Superconducting contacts and quantum interference phenomena in monolayer semiconductor devices

Inauguraldissertation

zur
Erlangung der Würde eines Doktors der Philosophie
vorgelegt der
Philosophisch-Naturwissenschaftlichen Fakultät
der Universität Basel

von

Mehdi Ramezani
from Tehran, Iran

2022

Genehmigt von der Philosophisch-Naturwissenschaftlichen Fakultät
auf Antrag von
Prof. Dr. Christian Schönenberger
Dr. Andreas Baumgartner
Prof. Dr. Richard Warburton
Prof. Dr. Klaus Ensslin
Assoc. Prof. Dr. Andras Kis

Basel, 22.02.2022

Prof. Dr. Marcel Mayor
Dekan

Widmung

I dedicate this manuscript to Dr. Ana Jesus for her constant support and love.

Contents

1 Introduction

It has been almost two decades since the isolation and investigation of graphene and other two-dimensional (2D) materials [1, 2]. Different research groups put tremendous efforts to study the novel characteristics of this diverse family of materials. Perhaps one of the most unique properties is the possibility of engineering novel heterostructure by stacking different Van der Waals (VdW) layers vertically [3]. Such a fabrication technique is known to be facile and low cost while maintaining a high quality and clean system. For instance, hexagonal boron nitride (hBN) that is a defect-free and atomically flat insulator can be replace a conventional atomic layer deposition (ALD) insulating layer. Beyond the non-interactive systems, researchers were able to combine 2D materials to engineer new band structures [4]. Interlayer coupling allows properties of one layer induced into another, and leads to band structure renormalizes in the Brillouin zone. Moreover, twistronics which is assembly of twisted-heterostructures is well realized in twisted VdW heterostructures [5].

Transitional metal dichalchogenides (TMDCs) are a class of 2D materials with a wide range of properties including semiconductors [6, 7], superconductors [8], and Weyl semimetals with topologically non-trivial phase [9]. TMDCs own a unique band structure [10], often with a large spin orbit interaction (SOI) [11], and outstanding optical properties [12] that is rare in other material systems.

Another intriguing topic is superconductivity, which is a correlative phenomenon defined as a drop of resistivity below a critical temperature. Superconducting materials show exotic physical properties such as Meissner effect [13], superconducting magnetic levitation [14], and heavy fermion superconductors [15].

The aim of this project is to establish a 2D semiconductors-superconducting hybrid system as a platform to investigate various new phenomena based on the interplay of electron pairing, electrically tunable two dimensional electron gas (2DEG), large SOI and electron-electron interaction in the semiconductor [16], and band topologies [17]. In addition, such a platform can bring control over phenomena such as Cooper pair splitting [18], coherent transport in quantum dots [19, 20], Majorana fermions [21], and superconducting quantum bit [22, 23].

In a typical superconductor-semiconductor hybrid system with high-quality (also described as high-transparency) contacts the superconducting properties can leak into the semiconductor. It is imperative that the semiconductor remains protected against charge traps, and scatterers in the surrounding environment. Investigation of these hybrid systems is challenged by (often occurring) a high contact resistance. This is often attributed to the formation of Schottky barrier at the interface of superconductor and semiconductor. Beyond the arguments of the work-function missmatch between the superconductor and semiconductor, the interface of materials should be clean and disorder free [7, 24, 25]. The aim of this project is to establish novel contact fabrication methods that protect the pristine properties of 2D semiconductor materials that allow the investigation of induced superconducting proximity effects.

In this dissertation, we first discuss various transport phenomena that are cited in the course of this manuscript. We continue with detailed descriptions of various novel techniques in the fabrication of normal and superconducting contacts and provide our experimental findings. Finally, we report on superconducting MoRe vertical interconnect access (VIA) contacts with clear evidence of a superconducting energy gap, a weak coupling strength between the superconductor and the semiconductor. We then extensively characterise these hybrid devices at cryogenic temperatures and study the magneto transport in a large magnetic field range.

2 Theoretical background

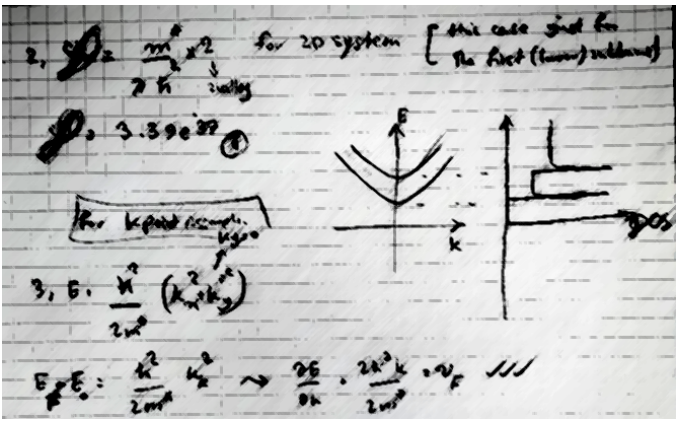

In this chapter, we provide with the theoretical background and transport phenomena which we use in the following chapters. We discuss charge transport in the ballistic and diffusive limit, and Schottky barrier formation. We will look at charge transport with quantum interference effect, and in quantum dots. Furthermore, beyond the transport of single-particles in a normal material, we discuss superconductivity and related phenomena. Our aim in this chapter is to understand what are the quantum interference effect in the proximity of a superconductor and to determine how it evolves in two-dimensional and two-dimensional systems.

2.1. Charge transport

Charge transport in a material system could be influenced by various parameters. Amongst them are temperature, dimensionality (1D, 2D, etc), geometrical size of the conductor, and a length scale known as mean free path. The later characterizes the average distance between subsequent inelastic scatterings between electron-electron or electron-phonon. If the mean free path is larger than the geometrical size ($l_{mfp} > L$) the transport is in the ballistic regime, otherwise it is classified as semi-ballistic regime, or diffusive regime.

The current in a conductor can be written as $I = nev = GV$, where n is the charge carrier density, e is the electron charge, and v is the velocity at which carrier move across the junction, G is the conductance, and V is the voltage across the junction. The Landauer formalism describes the conductance in a ballistic system as:

$$G = \frac{e^2}{h} MT, \tag{2.1}$$

where M is the number of quantum mechanical modes with the transmission coefficient of T.

In a fully diffusive regime, the quantities such as momentum, spin, and phase are fully randomized throughout the length where charge transfer occurs. Similar to the momentum relaxation length (l_{mfp}), a distance over which spin is relaxed the λ_s, and phase coherence length as l_ϕ are important parameters.

In the following chapters, we will restrict ourselves to charge transport within a semi-classical framework, and further discuss quantum effects, and charge transfer in presence of an external magnetic field.

2.1.1. Drude model, diffusive transport

In this section, we discuss the charge transport in a diffusive regime, where inelastic scattering randomizes the momentum of the charge carriers. The Drude model treats electrons as particles with a non-zero effective mass m^*, and studies the movement of these particles in a homogeneous crystal. The assumption is that the electric field $\overrightarrow{E}$ accelerates the electrons, and electrical resistance R results from scattering events. The total current density for the electrons with charge e and the number density of n reads:

$$\vec{j} = -ne\vec{v}_d = -ne\mu\vec{E} = \sigma\vec{E}, \tag{2.2}$$

where $\vec{v}_d$ denotes the mean drift velocity. The mobility is defined as $\mu = e\tau_{\mathrm{el}}/m^*$, where τ_{el} is the characteristic elastic scattering time. Therefore, the Drude conductivity in absence of magnetic field reads:

$$\sigma_{B=0} = en\mu = \frac{ne^2\tau_{\mathrm{el}}}{m^*}. \tag{2.3}$$

For a two-dimensional electron gas with a parabolic dispersion relation, we can write the electron density as:

$$n_s = \frac{g_s g_v k_{\mathrm{F}}^2}{4\pi}, \tag{2.4}$$

where g_s is the spin degeneracy factor, g_v is the valley degeneracy factor, and k_{F} is the Fermi wavevector. Substituting eq. 2.4 and mean free path $l_{\mathrm{mfp}} = v_{\mathrm{F}}\tau = \hbar k_{\mathrm{F}}\tau/m^*$ in eq. 2.3, the Drude conductivity in two-dimensions reads:

$$\sigma_{2D} = g_s g_v \frac{e^2 k_{\mathrm{F}} l_{\mathrm{mfp}}}{2h}. \tag{2.5}$$

In a two-dimensional system of a length of L, and a width of W, the electric current is $I = jW$, and the conductance is related to the conductivity by $G = \sigma W/L$. Since the specific resistivity $\rho = 1/\sigma$ is the inverse of the conductivity, and related to the resistance by $R = \rho L/W$.

2.1.2. Magnetotransport in homogeneous samples

This chapter discusses different aspects of Drude conductivity in the presence of an external magnetic field. Here we assume a two-dimensional system where electrons move in the $x-y$ plane, and an external magnetic field B is oriented along the $\vec{z}$ direction. In the absence of an external magnetic field, the conductivity writes as:

$$\sigma = \frac{\sigma_{(B=0)}}{1+\omega_c^2\tau_{el}^2}\begin{bmatrix} 1 & \omega_c\tau_{el} \\ -\omega_c\tau_{el} & 1 \end{bmatrix} = \frac{en\mu}{1+\mu^2B^2}\begin{bmatrix} 1 & -\mu B \\ \mu B & 1 \end{bmatrix}. \tag{2.6}$$

Here, the cyclotron frequency is denoted as $\omega_c = eB/m^*$. By inverting the conductivity tensor the resistivity tensor ρ (i.e. global sheet resistivity) reads:

$$\sigma^{-1} = \rho = \frac{1}{en\mu}\begin{bmatrix} 1 & \mu B \\ -\mu B & 1 \end{bmatrix}, \tag{2.7}$$

where the longitudinal and the transversal components (i.e. Hall resistivity) in respect to the current density are given by the diagonal, and off-diagonal components of resistivity tensor, respectively. In a Hall bar structure with $\vec{j} \parallel \vec{x}$ the longitudinal and transversal resistivity components are written as:

$$\begin{aligned} \rho_{xx} &\equiv \rho_{yy} \equiv \frac{1}{en\mu}, \text{ and} \\ \rho_{xy} &\equiv -\rho_{yx} \equiv \frac{B}{en}. \end{aligned} \tag{2.8}$$

Figure 2.1(a) shows schematics of a device with Hall bar structure. Using such device, the longitudinal resistivity $\rho_{xx} = U_{xx}W/(IL)$, and the transversal resistivity $\rho_{xy} = U_{xy}/I$ can be directly measured as macroscopic properties. By comparing the measurement values with eq. 2.8 one can extract electron density, and Hall mobility. The evolution of ρ_{xx} and ρ_{xy} in the presence of a magnetic field perpendicular to xy plan, is illustrated in fig. 2.1(b).

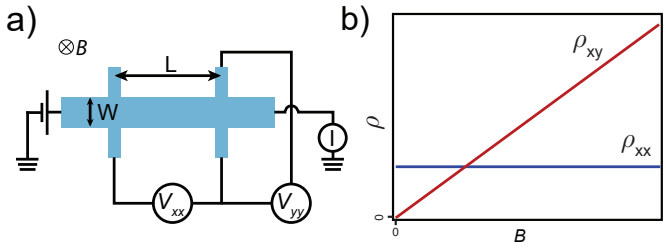

Figure 2.1. a) Schematics of Hall bar structured device and a perpendicular magnetic field. b) Evolution of longitudinal resistivity (ρ_{xx}) and transversal resistivity (ρ_{xy}) in respect to the perpendicular magnetic field.

2.1.3. Quantum Hall Effect

In this chapter, we will discuss the quantum Hall effect (QHE) that exhibits only in a two-dimensional system. In a semiclassical view, an external magnetic field causes in-plane circular motion in the mobile charge carriers. The electronic density of states $\mathcal{D}(E)$ (that is DoS) is the number of electronic states in $[E, E + dE]$ and per unit volume. In a two-dimensional system with a parabolic band dispersion the DoS is constant, and reads:

$$\mathcal{D}_{2D}(E) = \frac{gm^*}{2\pi\hbar^2}, \tag{2.9}$$

where g is the degeneracy factor of the electronic bands.

The interference of the two-dimensional electron gas with itself in circular orbits gives rise to the quantization of the electron energy, known as Landau quantization (see fig. 2.2). The energy between these quantized levels that are known as Landau levels (Lls) scales linearly with the magnitude of the perpendicular magnetic field. Above a critical magnetic field, the DoS in 2D is no longer a constant value (see fig. 2.2(b)), and instead shows an oscillatory characteristics. The maxima of the density of states in fig. 2.2(c) attributed to the extended states, and the outer states attributes to the extended states. The distribution of these quantized states is affected by spatially varying potential throughout the area of the sample. Spatial potential fluctuations are created by various effects and mainly by the random arrangement of charges in the sample and in the surrounding environment.

The number of filled Landau levels is called filling-factor ν, and defined as:

$$\nu = \frac{n}{n_L} = \frac{nh}{eB}. \tag{2.10}$$

Electrons in different Landau levels do not scatter into unoccupied states that are located above the Fermi level. At high magnetic field and low

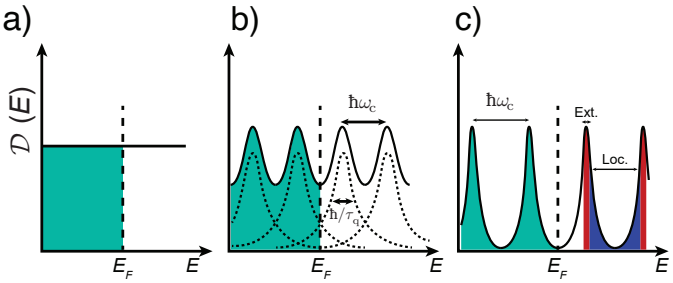

Figure 2.2. a) Landau level quantization by increasing the perpendicular magnetic field. The contribution of extended and localized states are indicated.

temperature, and whenever Fermi level lies between two consecutive Landau levels ($\nu \in 1, 2, 3, ...$) the transverse resistance is a constant value that is $R_{xy} = h/\nu e^2$. This effect is known as the integer quantum Hall effect (see fig. 2.3). Unlike in a classical description, the longitudinal resistance R_{xx} is not constant (as in the Drude model) and oscillates with 1/B periodicity. These oscillations have direct effect on the macroscopic characteristics of the device, and are known as Shubnikov-de Haas (SdH) oscillations (see fig. 2.3). In the case of the integer quantum Hall effect, the longitudinal resistance drops to zero around each transversal resistance plateau. In the QH regime, the current is carried by the extended states that run along the physical edge of the device, and the backscattering of charge carrier is strongly reduced. The localized states circle within the bulk of the two-dimensional gas (2DEG).

Taking into account the broadening due to spatial fluctuations at finite temperature, and with the assumption of symmetric broadening: the variation of the DoS takes the form of [26]:

$$\frac{\Delta\mathcal{D}}{\mathcal{D}} = -2\mathrm{e}^{-\pi/(\omega_c\tau_q)}\frac{2\pi}{\hbar\omega_c}\cos(2\pi\frac{E}{\hbar\omega_c}). \tag{2.11}$$

The oscillation is the DoS directly leads to an oscillatory cosine term that is periodic in transverse magnetic field. Using SdH oscillation one can extract charge carrier density in the bulk of sample is [27, 28]:

$$n = \sum g_v g_s \frac{e}{h} f_{\mathrm{SdH}}, \tag{2.12}$$

where f_{SdH} is the oscillation frequency of conductance with respect to the inverse of the magnetic field ($1/B$), and g_v and g_s are integer values corresponding to the valley, and the spin degeneracy of the Landau levels,

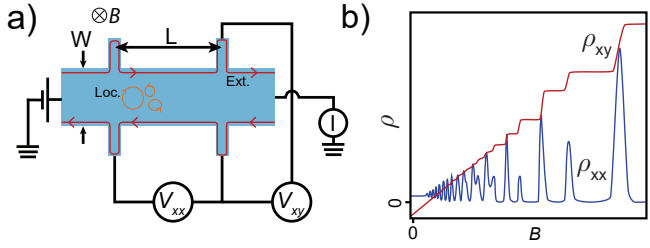

Figure 2.3. a) Schematics of Hall bar structure with a perpendicular magnetic field. Extended states and localized states are demonstrated. b) A typical longitudinal resistivity (ρ_{xx}) and transversal resistivity (ρ_{xy}) as a function of magnetic field applied perpendicular to the Hall bar plane.

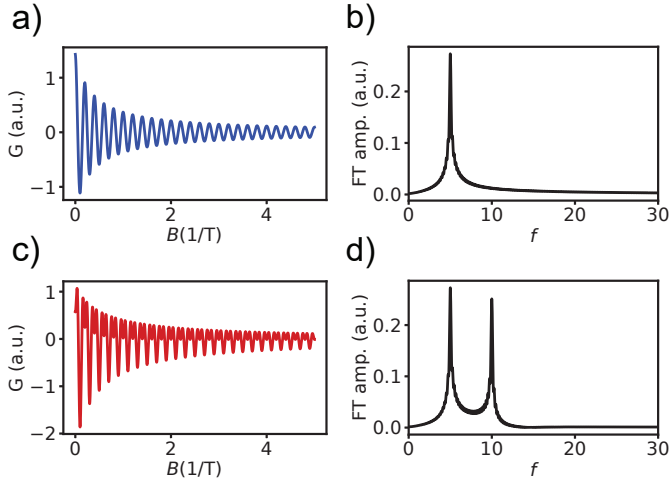

Figure 2.4. a) Conductance as a function of the inverse magnetic field. This graph illustrates SdH oscillations from degenerate subbands. b) Amplitude of the Fourier transformation as a function of frequency. The maximum frequency f indicates the oscillation frequency in (a). b) Conductance as a function of the inverse magnetic field, and from two non-degenerate subbands. d) Amplitude of the Fourier transformation as a function of frequency. The two peaks in frequency indicate the oscillation frequencies in (c).

respectively. Using fast Fourier transformation (FFT) we can extract the oscillation frequency of the experimental data (see fig. 2.4). The spin degeneracy of Landau levels can be lifted in magnetic field atributed to the Zeeman energy $\epsilon_Z = g^* \mu_B B$, where g^* is so-called Landé g-factor, and μ_B denotes the Bohr magneton. Consequently, at a high magnetic field, the spin degeneracy of the Landau levels is lifted, and magneto-resistance exhibits a secondary oscillation pattern with twice the frequency(see fig. 2.4(c, d)).

In a semiclassical intuitive picture, the magnetic field at which SdH oscillations are visible in magneto-resistance measurements is usually interpreted as the onset where charge carriers closing a cyclotron orbit before being scattered. This happens roughly at $\omega_c \tau_{crit.} > 1$, where $\omega_c = eB/m^*$ is the cyclotron frequency, and τ is the momentum scattering time. We note that in principle the visibility of the oscillation is affected by the sensitivity of the experiment. This simple estimation yields to a lower bound for the charge carrier mobility of $\mu = e\tau/m^* = 1/B_{crit.}$, and scattering time of $\tau = m^*/eB_{crit.}$.

2.2. Schottky barrier formation

An electronic device based on a semiconductor galvanically contacted to metallic contacts often suffers from high contact resistance. This is mainly explained by Schottky barrier formation at the contact interfaces. Although an uncompromising description of the Schottky barrier formation in two-dimensional material is beyond the scope of this thesis [29], we provide a simple explanation and discussion.

The difference between the metal work function (Φ_{m}) and the semiconductor electron affinity ($\chi_{\mathrm{sc.}}$) results in a sharp step in the electrical potential. Figure 2.5(a) demonstrates a typical semiconductor and metal (not brought in contact) where the Fermi level of metal lies inside the semiconductor gap. Once the two materials are brought into contact, the electrochemical potential comes to an equilibrium by the exchange of electrons. This charge transfer creates an electric potential barrier at the interface. To equilibrate the electrochemical potential, the electrical bands of the semiconductor reconstruct and lead to a potential barrier with a finite width and height, known as Schottky barrier (see fig. 2.5(b)). Especially at low temperatures at which tunnelling induced by thermal excitation across the Schottky barriers is negligible, and the excitation energy due to bias voltage is arbitrarily small, the electron tunnelling rate through the Schottky barriers can be very small. In other words the Schottky barrier formation hindersthe flow of charge in semiconductor devices. Using an electrical gate, one can tune the bands in the semiconductor and narrow the Schottky barrier width such that the electron tunnelling is allowed for charge carriers with finite electrochemical energy.

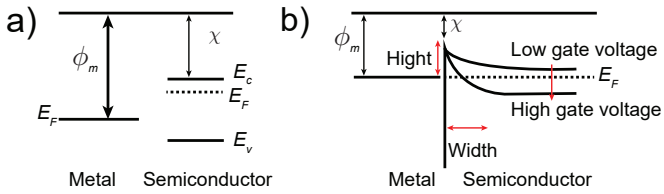

Figure 2.5. a) Demonstration of work function of an isolated metal, and electron affinity of a semiconductor, when both are isolated. b) Demonstration of Schottky barrier formed at contact interface, and effect of gate voltage on the Schottky barrier width.

Theoretically, the use of a low work function metals (e.g. Al, In, etc) as contact material leads to a lower Schottky barrier height. However, in confined electronic devices such as in 2D system this picture fails: Meaning that

there are other mechanisms that can influence the Schottky barrier height including chemical bonds, and surface reconstruction. Moreover, the contact interface is prone to impurity, material degradation, and accumulation of chemical residue at the interface.

2.3. Quantum interference

In a high-quality semiconductor, the phase coherence length is comparable to the dimensions of the electronic device and the measurements exhibit quantum mechanical interference effect. For instance, in a one-dimensional system such as carbon nanotube (CNT), the mean-free path can be solely limited by the device length (i.e. ballistic regime). Therefore, the electronic transport is governed by partial transmission and reflection at two contact interfaces [30]. This is analogous to an optical Fabry Pérot (FP) cavity consisting of two partially reflective mirrors at the two ends of an optical cavity. The electron plane wave travelling inside the CNT gains a kinetic phase upon a round trip between two barriers. This leads to constructive interference when the phase change is equal to $\Delta\phi = 2k_{\mathrm{F}}L$.

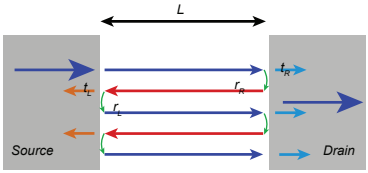

Figure 2.6. a) Schematics of an electronic Fabry Pérot cavity in one dimension, with partial transmission and reflection at the contact interfaces.

As illustrated in fig. 2.6, each contact interface is assigned reflection $r_{\mathrm{R}}, r_{\mathrm{L}}$, and transmission $t_{\mathrm{R}}, t_{\mathrm{L}}$ coefficients. For two symmetric delta scatterers at the two interfaces, we obtain a Lorentzian resonance:

$$T(E) = \frac{\Gamma_{\mathrm{L}}\Gamma_{\mathrm{R}}}{\Delta E^2 + 0.25(\Gamma_{\mathrm{L}} + \Gamma_{\mathrm{R}})}. \tag{2.13}$$

The current passing through the device is then given by:

$$I(E) = \frac{e}{h}\int_{-\infty}^{\infty} T(E)[f_{\mathrm{R}}(E-\mu_{\mathrm{R}}) - f_{\mathrm{L}}(E-\mu_{\mathrm{L}})]dE, \tag{2.14}$$

where $f_{\mathrm{L/R}} = 1/(\exp[(E-\mu_{\mathrm{L/R}})/k_{\mathrm{B}}T] + 1)$ is the Fermi distribution function, and μ is the electrochemical potential of left and right reservoirs.

In order to see the effect of gate voltage and bias voltage on the FP resonances, we assume the FP cavity is defined by the length in between the two barriers. The constructive interference occurs when $2Lk(E) = N2\pi$, where N is an integer number; therefore $k_N = \pi N/L$. We introduce $\eta = E_{\mathrm{F}} - E_{\mathrm{BM}}$ as the energy difference between the Fermi energy and the

conduction(/valence) band minimum(/maximum). The energy associated with each standing wave in a parabolic band dispersion is:

$$\eta_N = \frac{\hbar^2 k_N^2}{2m^*} = \frac{\hbar^2 \pi^2 N^2}{2m^* L^2}. \tag{2.15}$$

In a simple model, the interference happens when the source and drain reservoirs electrochemical potential is aligned to the resonance maximum energy. Therefore, the bias voltage between two states writes:

$$V_{\mathrm{SD}}^{m+1} - V_{\mathrm{SD}}^{m} = E_{\mathrm{m+1}}/e - E_{\mathrm{m}}/e = \frac{\hbar^2 \pi^2}{2m^* e L^2}(2m+1). \tag{2.16}$$

After discussing the effect of the bias voltage, now we discuss the effect of gate voltage on the FP resonances. The charge carrier density can be calculated using a plate capacitor model:

$$n = \int_{E_{\mathrm{BM}}}^{\infty} \mathcal{D}(E) f(E) dE = \frac{2m^*}{\pi\hbar^2}\eta = \frac{C\Delta V_{\mathrm{G}}}{e}, \tag{2.17}$$

where V_{G} is gate voltage, $\Delta V_{\mathrm{G}} = V_{\mathrm{G}} - V_{\mathrm{pinch-off}}$ is offset in respect to the pinch off voltage, and C is the capacitance per unit area. Substituting $\eta(V_{\mathrm{BG}})$ from eq. 2.17 in eq. 2.15, the gate voltage difference of two consecutive resonances reads:

$$V_{\mathrm{BG}}^{m+1} - V_{\mathrm{BG}}^{m} = \frac{\pi e}{L^2 C}(2m+1). \tag{2.18}$$

The slope of which constructive interference occurs is then:

$$\frac{\Delta V_{\mathrm{SD}}}{V_{\mathrm{BG}}} = \frac{\pi\hbar^2 C}{2m^* e^2}, \tag{2.19}$$

which is independent of the cavity length, gate voltage and bias voltage.

In order to extract the FP cavity length, we rewrite the condition for the constructive interference as $2L{=}N\lambda_{\mathrm{F}}$ where N is an integer. The Fermi wave vector is described as $k_{\mathrm{F}} = \sqrt{\frac{4\pi n}{g_{\mathrm{s}} g_{\mathrm{v}}}}$ where n is the charge carrier density, g_{s} is the spin degeneracy, and g_{v} is the valley degeneracy (we take $g_{\mathrm{v}} g_{\mathrm{v}} = 2$ for a 2-valley system with spin-degenerate bands). The Fermi wave length can be written as $\lambda_{\mathrm{F}} = \frac{2\pi}{k_{\mathrm{F}}} = \sqrt{\frac{2\pi}{n}}$. Therefore, the cavity length reads: $2L = N\sqrt{\frac{2\pi}{n}}$. For the N-th resonance one can write: $L\sqrt{n_N} = N\sqrt{\pi/2}$, and for the $N{+}1$-th resonance: $L\sqrt{n_{N+1}} = (N+1)\sqrt{\pi/2}$. By subtracting these two values as for the two neighbouring peaks, the cavity length writes:

$$L = \frac{\sqrt{\pi/2}}{\sqrt{n_{N+1}} - \sqrt{n_N}}. \tag{2.20}$$

In a two-dimensional system, Fabry Pérot resonance can occur as shown in fig. 2.7. The constructive and destructive interference depend on the charge carrier wavelength ($\lambda_F = 2\pi/k_F$), and the characteristic cavity size L. Upon total of two incidents of a charge carrier to the interfaces at an angle of θ (see fig. 2.7), the successive charge carrier gains a phase shift of $\Delta\phi = 2k_xL = 2k_FL\cos(\theta)$. Summing over all partial outgoing paths, the transmission probability writes:

$$T(\theta) = \frac{1}{1 + F\sin^2(\Delta\phi/2)}, \tag{2.21}$$

where $F = 4 \mid r_L \mid\mid r_R \mid /t_L^2 t_R^2$ (also in one-dimension) is known as finesse and interpreted as a measure of the quality factor. The effect of between destructive and constructive interference on the signal amplitude is large when $F \gg 1$. If the transmission coefficient is near 1 and the boundaries are symmetric the finess is one $F = 1$.

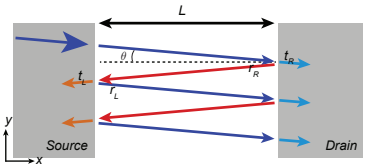

Figure 2.7. Schematics of a semiconductor Fabry Pérot cavity in two dimensions, where the incoming charge carrier has an incident angle of θ

By integrating over all incident angles in two dimensions, one can calculate the conductance normalized to the mean conductance:

$$G/\langle G\rangle = \frac{1}{2}\int_{-\pi/2}^{\pi/2} T(\theta)\cos(\theta)d\theta. \tag{2.22}$$

As it is stated previously, the constructive interference occurs when k_FL is multiples of π, indicating that the conductance maxima are mainly due to charge carriers at small incident angles (due to the cos function in the eq. 2.22).

Moreover, in a two-dimensional system, for an electron moving in x-y plane, the total momentum is $k_{tot} = \sqrt{k_x^2 + k_y^2}$. So, for each k_x that meets the condition for the constructive interference, there are many k_y at different energies $E = \hbar^2 k_{tot}^2/2m$ to satisfy resonance condition. This averaging of all standing waves perpendicular to the current path leads to the vanishing of the interference signal. Therefore, a mechanism should allow for the filtering of incident angles and distribution of k. For instance, in a graphene Fabry

Pérot cavity [31] the angular filtering occurs due to the angular dependence of Klein tunnelling [32], and in a two-dimensional electron gas from the out-coupling from a waveguide type contact, or due to percolation paths in the disordered system this is known as "branched flow" [33]. Therefore, in chapter 6 we neglect the dimensionality of our system and analyse our measurement data using a one-dimensional Fabry Pérot cavity model.

2.4. Coulomb blockade and quantum dots

In this section, we cover the most important characteristics of quantum dots (QDs). In a typical dot, due to confinement effect and small self capacitance C, the Coulomb interaction $U \sim e^2/C$ in the system is relatively large and can be the dominating energy scale at low temperature. In that case, this extra energy is required to add a single electron to the electronic island. Figure 2.8(a) demonstrates discrete energy spectrum of a QD with tunnel coupling Γ_S, Γ_D to the source and drain contacts. The latter allows for particle tunnelling between the QD orbitals and the reservoirs. Therefore, for single electron tunnelling (SET) the chemical potential of the source and drain contact and the chemical potential of the discrete levels are relevant.

Apart from Coulomb interaction in a QD, the confinement energy is comparable to the charging energy, which is in turn quantizes the kinetic energy of the orbitals in the QD. This quantization of the energy is often called single-particle level-spacing δE which is the energy between the discrete eigenstates (orbitals) of the quantum dot.

In general, charge transfer from source to drain reservoir occurs when a resonance lies between the bias voltage window (see fig. 2.8(a)). Consequently, the addition energy $E_{\text{add}} = \mu(N+1) - \mu(N) = e^2/C + \delta E$ is the required energy to add one electron to the QD island.

The chemical potential (energy to add an electron) of discreet levels can be tuned using an electric voltage on the gate electrode, and the electrochemical potential of the source and drain contact using bias voltage. Using these two parameters, one can fully investigate the characteristics of a dot. The diamond-like structures shown in fig. 2.8(b) are known as Coulomb diamonds, in which the charge transfer is forbidden inside them because of the energy mismatch of N and $N+1$. Please note that this diagram only accounts for charging energy and does not represent the level spacing.

The total capacitance of the QD island can be written as $C = \Sigma(C_S + C_D + C_G)$ associated to source, drain, and gate capacitance respectively. For a disk shaped QD, neglectinc stray electric field at the edges, one can find $E_c = e^2/8\epsilon_0\epsilon_r r$, where ϵ_r is the relative permittivity of the dielectric layer, and r is the radius of the circular confinement [26, 34].

The tunnel coupling between orbitals in the QD and the reservoirs can determine the transport characteristics. In particular, in a so-called "weak coupling regime" where $\Gamma \ll U$, the transport is dominated by interactions and sequential single electron tunnelling into and from QD. In an intermediate regime where $\Gamma \sim U$, higher-order processes such as co-tunnelling and Kondo effect can exhibit in transport. In the strong coupling regime where $\Gamma \gg U$ the system can condense to a non-interacting resonant tunnelling problem.

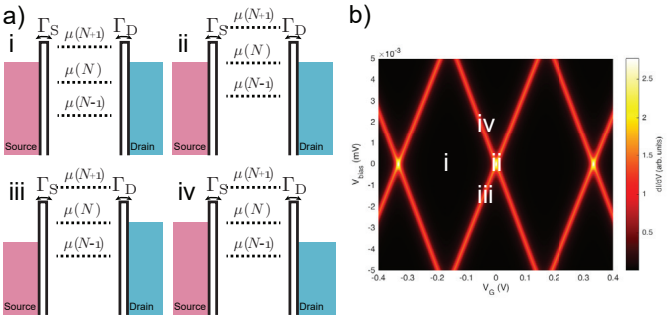

Figure 2.8. a) Schematic representation of a quantum dot with indicated parameters and different electrochemical energy detuning parameters. Bias voltage changes the chemical potential of the source and drain contacts. b) Representation of Coulomb diamonds, and respective energy scales.

2.5. Superconductivity

In this section, we discuss the most important principles of superconductivity and characteristics of normal-superconductor hybrid systems in one-dimension and two-dimensions. Superconductivity is a quantum many-body phenomenon that can be investigated on a macroscopic scale.

Dissipationless current (also known as supercurrent) is one of the most significant characteristics in a superconductor, and it was discovered in 1911 by Kamerlingh Onnes in mercury [35]. There is an upper limit for the amount of dissipationless supercurrent known as critical current (I_c) that can be limited by a variety of effects.

Another important characteristic is diamagnetism, such that any magnetic field is screened (i.e. Meissner effect) and magnetic field magnitude inside the bulk superconductor is zero [36], except in a small region, given by the London penetration depth (λ_L) at the surface. There is a limit of external magnetic field known as critical magnetic field (H_C) in which superconductivity is destroyed above that critical magnetic field.

Moreover, in a superconductor, the heat conduction by the electrons decays exponentially with temperatures below a critical temperature T_c [37]. Because of the same reason, a superconductor is not a good heat conductor below the critical temperature.

A microscopic model to explain the phenomena of superconductivity was developed in 1957 by Bardeen, Cooper and Schriefer, known as BCS theory [38]. The attractive interactions between electrons is mediated by phonons, and paired electrons of opposite momentum and spin, also known as Cooper

pairs. The Cooper pairs obey Bosonic statistics, and condense around the Fermi energy (in a range given by the interaction) into the same quantum-coherent ground state. The energy required to generate an excitation in the superconductor is finite, given by the energy gap Δ. The energy of these quasiparticles in respect to the electrochemical potential of Cooper pairs is $E_\mathrm{k} = \sqrt{\varepsilon_\mathrm{k}^2 + \Delta^2}$, where $\varepsilon_\mathrm{k} = \hbar^2 k^2/2m - \varepsilon_\mathrm{F}$ is the kinetic energy of an electron with respect to Fermi energy. The density of states of quasi-particles ($\mathcal{D}$) reads:

$$\mathcal{D}_\mathrm{S}(E) = \begin{array}{ll} \mathcal{D}_\mathrm{N} \frac{|E-E_\mathrm{F}|}{\sqrt{(E-E_\mathrm{F})^2-\Delta^2}} & (|E-E_\mathrm{F}| > \Delta) \\ 0 & (|E-E_F| < \Delta) \end{array} \tag{2.23}$$

where $\mathcal{D}_\mathrm{S}(E)$ is the density of states of the quasi-particles in the superconducting state, $\mathcal{D}_\mathrm{N}$ is the density of states in the normal state. A representation of the quasiparticle density of state $\mathcal{D}_\mathrm{S}(E)$ is shown in Fig.2.9.

Ginzburg and Landau developed a (phenomenological) description of the superconducting wave function $\psi(\vec{r},t) = \sqrt{n_s(\vec{r},t)}e^{i\varphi(\vec{r},t)}$, where $n_s(\vec{r},t)$ corresponds to the local Cooper pair density and φ to the macroscopic phase of the condensate. Within this model the coherence length determines the spatial variation of the superconducting order parameter. The coherence length in a clean superconductor is defined as $\xi_0^\mathrm{clean} = \hbar v_\mathrm{F}/\pi\Delta_0$, where v_F is the Fermi velocity in the normal state of superconductor [39, 40].

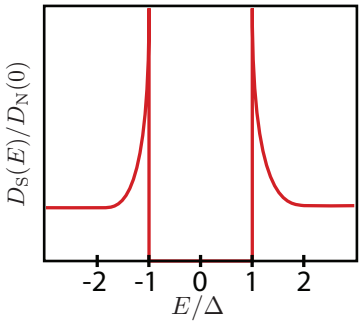

Figure 2.9. Illustration of the Density of states in a BCS superconductor, and superconducting energy gap Δ.

For any temperature above the absolute zero, the quasiparticles are thermally excited. Consequently the superconducting energy gap Δ decreases by increasing temperature, and vanishes at $T = T_\mathrm{c}$ which is known as critical temperature. An approximation of the temperature dependency of

superconducting energy gap can be written as [41]:

$$\Delta(T) = \Delta_0 \sqrt{1 - T/T_c}, \tag{2.24}$$

where Δ_0 is the zero temperature superconducting energy gap.

At and above the critical magnetic field ($B_c = \mu_0 H_c$), a thermodynamic phase transition to normal state occurs. When the value of the applied magnetic field exceeds B_c the superconductivity breaks down, and the external field penetrates the bulk of the superconductor. In a type-I superconductor, superconductivity breaks down above the critical magnetic field B_c. On the other hand, a type-II superconductor can host Abrikosov vortices at magnetic fields above the first critical magnetic field B_{c1}, and the superconductivity vanishes above the second critical magnetic field B_{c2} where $B_{c1} < B_{c2}$. These vortices pin randomly and can move around in the bulk, which itself leads to dissipation.

2.5.1. Andreev reflection-1D

This section aims to give an introduction to electric transport at a normal-superconductor (N-S) interface. Here, a new scattering process needs to be considered known as Andreev reflection (AR). In order to describe AR process, first, we assume an electron from the normal part, with an energy ε with respect to E_F impinging the N-S interface. For the excitation energies $\varepsilon > \Delta$, the electron enters the superconductor in an eigenstate almost identical to its electronic states. On the other hand, for $\varepsilon < \Delta$, the electron sees no single-particle state available, and normal reflection is prohibited due limit of momentum exchange ($\Delta/f_F \ll 2P_F$). However, in a higher-order process known as Andreev reflection, an electron is reflected as a hole (with $-\varepsilon$), and a charge of $2e$ is transferred into the superconductor by adding a Cooper pair to the condensate. As illustrated in fig. 2.10, the momentum of the electron and hole are (roughly) equal with opposite signs:$\vec{k_e} = -\vec{k_h}$, and the spin of electron and hole are similar to generate a Cooper pair singlet (two electrons with opposite spins). We will further discuss the theoretical description of transport through N-S junction in chapter 2.5.3.

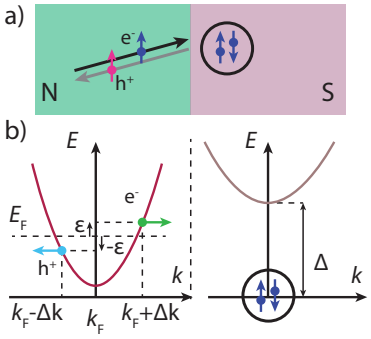

Figure 2.10. a) Schematics of Andreev reflection at an N-S interface. Electron and hole following the same path. b) Schematics of impinging electron and Andreev reflected hole, leaving a cooper pair in the superconductor.

2.5.2. Andreev reflection-2D

In this chapter, we discuss the basic properties of AR in a two-dimensional N-S junction. Figure 2.11(a) shows a two dimensional N-S junction, where an electron moving in $x-y$ plane, with a total momentum of $k_{\mathrm{F}}^{e} = \sqrt{(k_x^e)^2 + (k_y^e)^2}$. The superconducting contact includes the region $\vec{x} > 0$, and normal metal covers $\vec{x} < 0$. For an impinging electron to the N-S interface, two types of AR is considered (see fig. 2.11): i) Retro Andreev reflection (RAR, described above) if $E_{\mathrm{F}} \gg \Delta$. ii) Specular Andreev reflection (SAR) if $E_{\mathrm{F}} \leq \Delta$.

The elastic scattering does not change the amplitude of the momentum along the interface. Therefore, for both RAR and SAR processes the wavevectors are: $\vec{k_y^h} = -\vec{k_y^e}$.

However, the momentum perpendicular to the N-S interface depends on the AR at the interface. What distinguishes between RAR and SAR is the sign relation between the wavevector ($\vec{k_x}$) and group velocity ($\vec{v_{\mathrm{F}}}$) of the incoming electron and reflected hole.

In other words, specular Andreev reflected holes and incoming electrons do not counter propagate (see fig. 2.11).

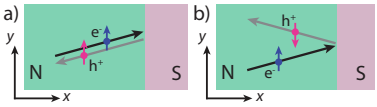

Figure 2.11. Schematics of (a) Retro Andreev reflection and (b) specular Andreev reflection in two-dimensional N-S junction.

The SAR is predicted for graphene and bilayer graphene near the Dirac point [42, 43]. A RAR process in graphene includes an electron and hole from conduction band (an intraband process). On the other hand, in a SAR process in graphene requires an electron from the conduction band while the hole is from the Valence band (an interband process) [42–44]. In this manuscript, we mainly focus on the retro Andreev reflection, since the SAR process does not happen in the MoS_2, or any semiconductor with a conventional parabolic band dispersion.

2.5.3. BTK model, and broadening parameter

The transport across N-S junction can be described by a theory first developed by Blonder, Tinkham, and Klapwijk in 1982 [39], also known as BTK model. Here the N-S junction is a 1D-system where the normal material is located at $x < 0$, and superconductor at $x > 0$. At the N-S interface a repulsive potential is modelled using a delta-distribution potential $V(x) = H\delta(x)$, where $H = Z\hbar v_{\mathrm{F}}$ describes the normalized barrier height, and δ is a Delta function. The parameter Z defines a dimensionless barrier strength that accounts for the elastic backscattering at the interface. The barrier height and contact transparency T are related by $T = 1/(1 + Z^2)$.

By matching the wave functions of normal and superconductor material, which are solutions of the Bogoliubov-de Gennes equations [39, 40], an expression for the differential conductance can be written as:

$$\mathrm{d}I/\mathrm{d}V = C_{\mathrm{N}} \int_{-\infty}^{\infty} [f(E - eV) - f(E)][1 + A(E) - B(E)]dE, \qquad (2.25)$$

where $A = \mid a \mid^2$, and $B = \mid b \mid^2$ are the coefficients expressing the probability of Andreev reflection and normal reflection, respectively. $C_{\mathrm{N}} = (1 + Z^2)/(eR_{\mathrm{N}})$ is a constant which depends on the barrier strength (Z), and the normal state resistance (R_{N}). For an ideal N-S junction the coefficients are given as $a = u_0 v_0/\gamma$, and $b = (u_0^2 - v_0^2)(Z^2 + iZ)/\gamma$, where $u_0^2 = 1 - v_0^2 = 0.5(1 + [(E^2 - \Delta^2)/E^2]^{0.5})$ are the coherence factors of the BCS condensate, and $i = \sqrt{-1}$ imaginary unit.

As demonstrated in fig. 2.12, for a fully transmitting interface (i.e. $Z = 0$, or $T = 1$), it was found that the conductance should double for $\varepsilon < \Delta$ compared to the normal state conductance $\varepsilon > \Delta$. In an intuitive picture: every electron is reflected as a hole leading to a charge transfer of $2e$ into the superconductor. For transmissions $T < 1$ the conductance is suppressed in the gap, since the probability of AR and transmission is related by $\propto T^2$. For $T \ll 1$ and in the so called tunnelling regime the conductance of the N-S junction reflects the quasiparticle density of state (see fig. 2.12).

The aforementioned discussion holds for an ideal N-S interface. However, in practice, possible disorders at the interface can lead to a broadening. In ref. [45], Dynes et al. introduced an inelastic scatting term for the non-ideal N-S interface and modified the Bogoliubov-de Genes equation. Consequently, a quasiparticle lifetime broadening τ is introduced which corresponds to an energy $\Gamma = \hbar\tau$ known as Dynes parameter [46]. This modifies the coefficients for the probability of Andreev and normal reflection and

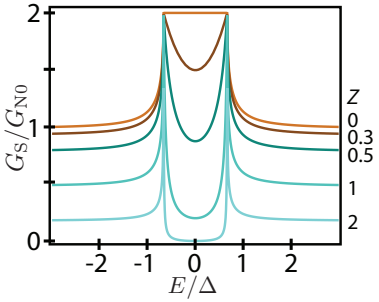

Figure 2.12. Conductance through the N-S interface for different indicated Z values.

writes [46, 47]:

$$
\begin{aligned}
A(E) &= \frac{\sqrt{(\alpha^2+\eta^2)(\beta^2+\eta^2)}}{\Gamma}, \text{ and} \\
B(E) &= Z^2\frac{[(\alpha-\beta)Z-2\eta]^2+[2\eta Z+(\alpha-\beta)]^2}{\Gamma}, \text{ and} \\
u_0 &= \frac{1}{2}(1+\frac{\sqrt{(\mid E \mid +i\Gamma)^2-\Delta^2}}{\mid E \mid +i\Gamma}),\ v_0 = 1-u_0 \text{ and} \\
\alpha &= \mathrm{Im}(u_0),\ \eta = \mathrm{imag}(u_0),\ \beta = \mathrm{Re}(v_0).
\end{aligned}
\tag{2.26}
$$

Here $A(E)$ and $B(E)$ are similar coefficients as in eq. 2.25, and the current through an N-S junction can be calculated with different broadening parameters. The experimental demonstration of BTK model with Dynes broadening parameter will be the subject of chapter 5, where we use the BTK model with Dynes parameter to fit to our measurements.

2.5.4. Quantum interference with superconducting leads

In this section, we discuss bound state coupled to a superconducting reservoir. Assume the situation where two superconductors are connected by a normal material of length L as shown in fig.2.13(a). If the transmission is high Andreev reflection can occur at both N-S interfaces. In particular, a right moving electron can undergo an Andreev reflection at the right superconductor, the resulting hole may reach the left superconductor, and Andreev reflected electron can move to the right, that is the initial motion direction of the electron. The single-particle phase-change upon each Andreev reflection for an electron is $-arccos(E/\Delta) + \phi_S$, where ϕ_S is the phase of the superconductor [39]), and while moving through the length of the junction is $(k_F L)$. If the total phase gain is multiples of 2π the two electronic partial waves interfere constructively and form a bound state called Andreev bound state (ABS) analogous to the Fabry Pérot interference. The total phase difference for an electron bouncing once at each interface writes:

$$\phi_{tot} = (k_h + k_e)L + \Delta\varphi - 2\arccos(\varepsilon/\Delta), \tag{2.27}$$

where $\Delta\varphi$ is the phase difference between two superconductors, and k_e and k_h are the wave vector of the electron and hole, respectively. The total phase difference for a counter propagating hole is similarly described but has a minus sign before $\Delta\varphi$.

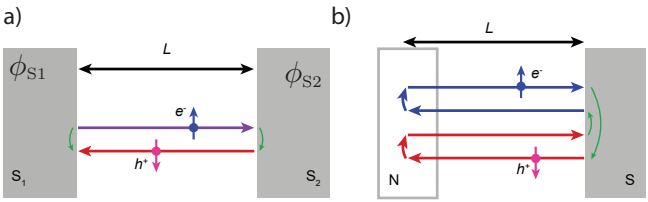

Figure 2.13. Schematics of Andreev bound state at (a) two, and (b) one superconducting interface(s). The later process is mediated by AR and a Fabry Pérot like process.

In the so-called short junction limit with the $L \ll \xi$, where ξ is the distance cooper pairs travel inside the normal metal (that is different than the coherence length ξ_0 in the bulk of a superconductor), the phase gain of a single-particle travelling through the junction (dynamic phase) is negligible. Therefore, for a clean interface and in the short junction limit, the energy of the Andreev bound state writes:

$$\varepsilon_{\pm}^{ABS} = \pm\Delta\cos(\varphi/2). \tag{2.28}$$

On the other hand, in the long junction limit where $L > \xi$ the dynamic phase gain is to be taken into calculations, and the energy of the Andreev bound state writes:

$$\varepsilon_{\pm}^{\mathrm{ABS}} = \pm\Delta\cos(\Delta\varphi/2 + \frac{L}{\xi}\frac{\varepsilon}{\Delta}). \tag{2.29}$$

This equation shows that ABSs can move into the superconducting energy gap, and occupying any arbitrary sub-gap energy.

Until now, we demonstrated the presence of Andreev bound state between two superconducting leads. However, Andreev bound state can also occur at one N-S interface, as illustrated in fig. 2.13(b). This process is mediated by the Andreev reflection at normal-superconductor interface, and normal reflection(s) due to disorder in the bulk of the normal conductor. As long as the total phase gain for a single particle is multiples of 2π, and these bound states can couple to other elements of the system.

2.5.5. Superconducting proximity effect

The superconducting proximity effect is closely related to Andreev bound state. When a normal material is placed between two superconducting leads, the Cooper pairs can tunnel into the insulator or normal conductor. The phase coherence of the Cooper pair is conserved after moving from one contact to another. In a peculiar case, in an S-I-S junction (i.e. a thin insulating layer between two superconductors) a dissipationless current develops between the two contacts. This phenomena was first described by Josephson et. al [48] and is known as Josephson current. Their theory introduces a perturbative tunnel coupling between the two superconductors that are separated by a thin insulating layer.

This dissipationless current is carried by Andreev bound states that are pinned the Fermi energy of the superconductor reservoir. Similar to the supercurrent in a superconductor, Josephson current exhibits a critical current I_{C}. Between two superconductors with different phases, the Josephson current is given by the first Josephson relation:

$$I(\varphi) = I_{\mathrm{C}}\sin(\varphi), \tag{2.30}$$

that is also known as the DC-Josephson effect. The phase difference can be determined using an external magnetic field exerting a flux through a superconducting loop enclosing the Josephson junction. When a DC bias voltage is applied to the Josephson junction, the phase evolves according to the second Josephson relation, where $\mathrm{d}\varphi/\mathrm{d}t = 2eV/\hbar$. Substituting the latter into eq. 2.30 the current through a Josephson junction is:

$$I = I_{\mathrm{C}}\sin(\frac{2eVt}{\hbar}). \tag{2.31}$$

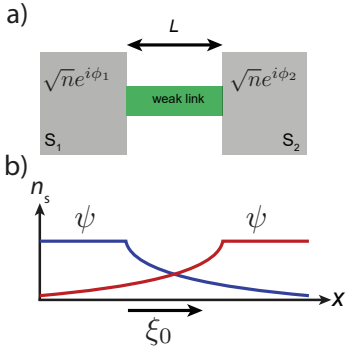

Figure 2.14. a) Illustration of the superconducting proximity effect in a weak link in between two superconducting contacts. b) Representation of the overlapping Cooper pair ground state of the left and the right superconducting reservoirs.

This equation is describing the AC-Josephson effect. Although the details of these effects are out of the scope of this manuscript, it is worth noting that the exact current-phase relation (CPR) depends on the strength and of the nature of the weak link.

We would like to point out that to sustain a Josephson current, the ABSs need to reach across the weak link from one superconductor to the other [49]. Moreover, a proximitized weak link is described when the Cooper pairs leaking out of the superconductor to the normal/Insulating material [20].

2.5.6. Reflectionless tunnelling

In the previous chapters, we discussed the Andreev reflection in an ideal N-S junctions. In practice, the interface near the superconducting contacts can be highly affected by the disorder. As stated earlier, the probability of Andreev reflection for the in-gap excitations ($\varepsilon < \Delta$) is directly proportional to the square transmission T^2, while for the larger excitation ($\varepsilon > \Delta$) is proportional to T since in the later only one charge needs to be transmitted across the N-S barrier. In the particular case of interfaces with small transmission factor, and disorder at the interface, an important quantum interference effect known as Reflectionless tunnelling is predicted. A normal reflected single-particle at the superconducting interface, can go through multiple (phase coherent) normal reflections within the disordered region, and eventually reflects back to the superconducting interface (see fig. 2.15). This process can repeat itself infinite times. Surprisingly, for $\varepsilon \sim 0$,

the probability of Andreev reflection at the N-S interface increases. This leads to an increase in conductance at zero bias voltage, which is known as reflectionless tunnelling [50].

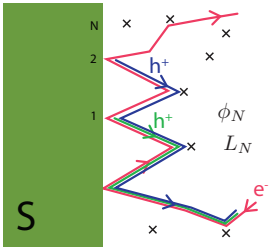

Figure 2.15. a) Demonstration of reflectionless tunnelling near the superconducting contact.

For an area A between the superconducting interface and an enclosed path inside the normal conductor, the total phase shift between the incoming electron and the reflected hole is:

$$\Delta\varphi = \frac{2\eta L}{\hbar v_{\mathrm{F}}} + 4\pi\frac{BA}{\Phi_0}, \tag{2.32}$$

where B is the external magnetic field, and η is the excitation energy relative to E_{F}, and $\Phi_0 = h/e$ is the flux quantum for a single charge. For $\Delta\varphi = 0$ the probability of Andreev reflection has a maximum, whereas the probability of normal reflection has a minimum. This results in a zero bias peak in the spectroscopic measurements (different than Josephson current) at zero bias voltage, and in the absence of an external magnetic field [51].

2.6. Coulomb blockade with Superconductor

The number of electrons in a quantumdot only varies by one, while superconductivity is a macroscopic phenomenon that involves countless electrons. A hybrid system of superconductor-quantum dot (N-QD-S) allows quasiparticle tunnelling into and from the isolated quantum dot, and Andreev processes simultaneously. However, the charging energy of the quantum dot (E_C) relative to the superconducting energy gap Δ, and tunnel coupling strength (Γ) are both relevant energy scales. The experimental realization of such hybrid systems often encounters challenges in a semiconductor due to the formation of large Schottky barriers at the superconductor-semiconductor interfaces [52].

The important message for the sake of our discussion is that depending on the coupling strength, a non-interactive picture of N-QD-S (illustrated in fig. 2.16(b)), can change to an interactive N-QD-S system [49]. For instance, at a very weak coupling regime, the QD is in blockade regime, and transfer of the Cooper pairs through the QD is highly unlikely, especially with an odd number of electrons in the capacitive island.

Simulation of a typical quantum dot with a very weak coupling to a superconductor is shown in fig. 2.16(c) [19]. A detailed experimental demonstration of QD with very weak coupling to the superconductor will be the subject of chapter 5 using spectroscopy measurements at low temperature.

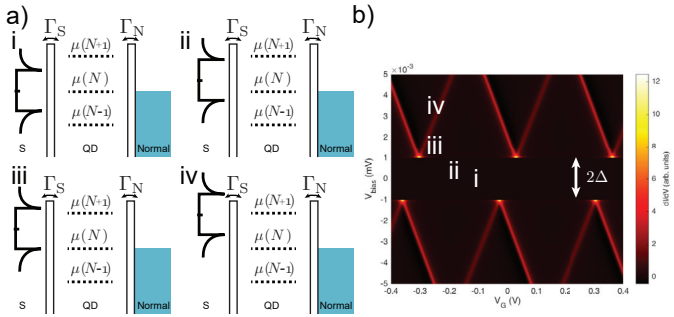

Figure 2.16. a) Schematics of N-QD-S device, at various de-tuning parameters. The energy diagram showing the allowed and forbidden transmissions. b) Simulation of a typical N-QD-S device measured.

2.7. Transition metal dichalcogenides

The family of transition metal dichalcogenides (TMDCs) are characterized by MX_2 where M represents a transitional metal (such as molybdenum, tungsten, vanadium, and titanium), and X_2 represents two dichalcogenide atoms (such as selenium, sulfur, and tellurium). Based on density functional theory, there is a prediction of around 40 compounds of this form [6], many of which are stable at ambient conditions and are synthesised or exfoliated from natural crystals. The crystallographic structure of TMDCs has mainly trigonometrical symmetry like graphene. The intralayer bonds consist of covalent bonds between each M atom and the neighbouring X atoms. The interlayer interaction (interaction between each layer) is due to Van der Waals (VdW) forces. Depending on which phase is stable at ambient condition, the unit cell has the trigonal prismatic (point group D_{3h}, 3H), or octahedral (point group D_{3d}, 1T) crystallographic symmetries.

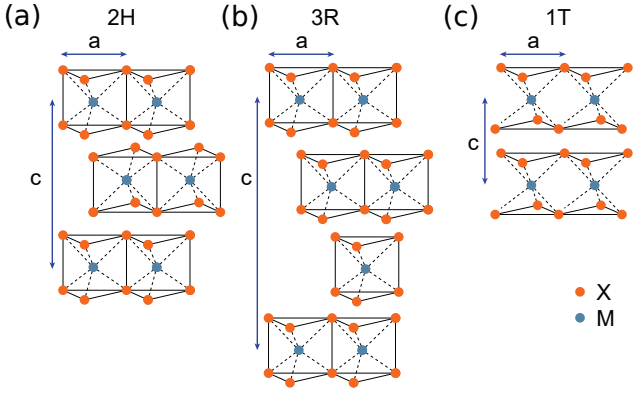

Figure 2.17. Structural schematics of a) 2H (i.e. 1H in monolayer), b) 3R, and c) 1T polytypes of TMDCs.

As illustrated in fig. 2.17, there can be different polytype stacking orders: 2H (1H for monolayer), 3R (1H for monolayer), and 1T. The first number in the stacking order defines the number of layers in the main unit cell, and the second part stands for hexagonal, rhombohedral, or trigonal lattice structure.

2.7.1. Band structure of MoS_2

MoS_2 is a semiconductor TMDC, with a parabolic band dispersion near the symmetry points K, and $K' = -K$ of the Brillouin zone, is expected to be robust against scattering by smooth deformations and long wavelength phonons due to a large valley splitting. When the thickness of this material is reduced down to an atomically thin regime or a monolayer limit, due to the confinement on the electronic structure, its bandgap increases from 1.29 eV (in bulk) to 1.9 eV (in monolayer) [12]. Moreover, the thinning of MoS_2 changes the indirect to direct band gap, experimentally reported in ref. [12, 53] and theoretically described in ref. [54]. During the course of this PhD project, we used 2H molybdenum disulfide (MoS_2), due to its peculiar properties. The lattice parameters of 2H MoS_2 are a=3.16 Å, and c= 12.294 Å[55–57]. While in the crystals with even numbers of the layer the inversion

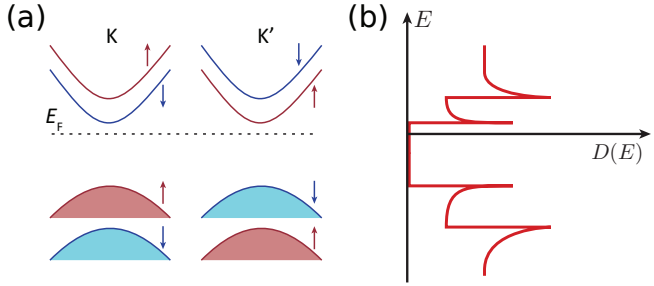

Figure 2.18. a) Dispersion relation of MoS_2 near the **K** and **K′** symmetry points. b) Density of states as a function of Fermi energy, indicating a doubling of Density of states by populating the upper subbands.

symmetry is prevailed, with an odd number of layers the inversion symmetry is broken. The broken inversion symmetry means if the transition metal atom is the inversion center, the chalcogen atoms map into the vacant space upon inversion. Meanwhile, the out of plane mirror symmetry is preserved. The broken inversion symmetry leads to the band structure symmetry in reciprocal space that gives degenerate subbands: $E^{\uparrow(\downarrow)}(\mathbf{K}) = E^{\uparrow(\downarrow)}(-\mathbf{K})$, where $\uparrow$ and $\downarrow$ are the spin up and down, respectively.

The intrinsic spin orbit interaction (SOI) of MoS_2 is due to the hybridization of d orbitals of the transition metal, and s orbital of the chalcogenide atoms. This modifies the band structure causing spin-orbit induced splitting in conduction and valence band in the vicinity of **K** and **K′** points, away from the time-reversal invariant point **M** and Γ points. The SOI and broken inversion symmetry in monolayer MoS_2 lift the Kramers' degeneracy

of the bulk. Therefore for the small momentum change near the **K** and **K′** point where $\mid \kappa \mid \ll \mid \mathbf{K} \mid$, we can write:

$$E^{\uparrow}_{\mathbf{K}}(\kappa) = E^{\downarrow}_{\mathbf{K}'}(\kappa), \tag{2.33}$$

where $\kappa = k - \mathbf{K}$, and $\kappa = k - (\mathbf{K}')$.

The effect of an intrinsic SOI on the band structure is illustrated in fig. 2.18(a), where the four-fold spin and valley degrees of freedom is realized in a monolayer MoS_2. However, overall spin degeneracy exists at zero magnetic fields. Based on the band calculations, the conduction band spin-orbit-induced splitting gap in energy is $\sim$ 3 meV [58, 59]. We would like to note that in two-dimensional systems, the electron-electron interaction is expected to be very strong. Therefore, the experimental value of the SO-induced splitting gap can vary from the aforementioned calculations [60, 61].

2.7.2. Andreev reflection in MoS_2

Due to the unique band structure of MoS_2, retro Andreev reflection (RAR) occures under certain condition, and with combination of certain valley and spin. For instance, for an impinging electron with excitation energy $+\varepsilon$ above E_F, spin up in $\mathbf{K}'$ valley, the reflected hole with an energy of $-\varepsilon$ has spin up to meet the spin-singlet requirement of a Cooper pair. In fig. 2.19 for avoiding confusion, we used electrons in the conduction band to demonstrate all of the process, and avoid showing the holes. Otherwise, the hole bands (not shown here) are inverted electron bands (virtual bands in the conduction band), in which spin and the group velocity of the holes are opposite of their counterpart electrons. In addition, the momentum of electron and reflected hole along $\vec{x}$ is $\vec{k_x^e} = -\vec{k_x^h}$. Thus, it is not allowed for the Andreev reflected hole to exist in the same valley of the impinging electron. Figures 2.19(b, and c) show two possibilities of RAR that occur in the two lower subbands of MoS_2. Demonstration of such momentum transfer in the first Brillouin zone of MoS_2 is shown in fig. 2.19(d). For a finite excitation energy $\varepsilon > 0$, there is a momentum mismatch δq between $\vec{k_x^e}$ and $\vec{k_x^h}$. An external magnetic field $B_z > 0$ leads to Zeeman shift ($\Delta\epsilon_Z = g\mu_B B$). Due to the Zeeman shift in each subband, momentum mismatch increases for spin up electron and hole, and decreases for spin down electron and hole. A schematic of this effect is shown in fig. 2.19(e,h).

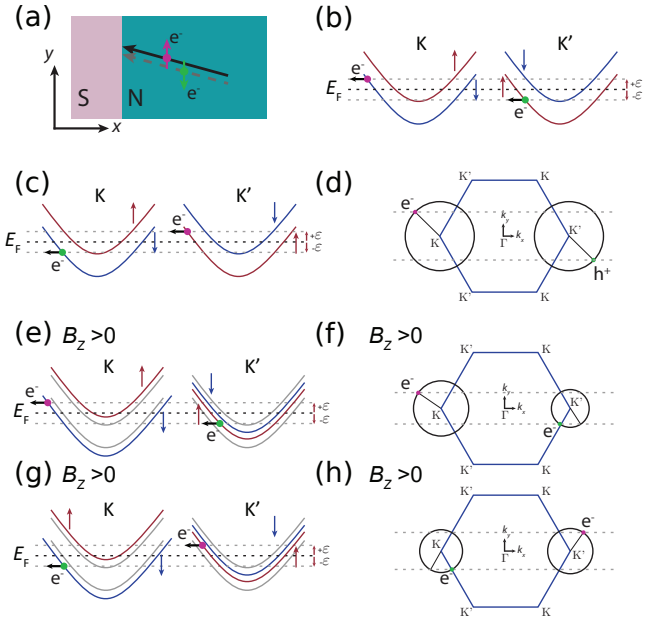

Figure 2.19. a) Demonstration of RAR at an N-S interface. b) Band dispersion along k_x, demonstrating an impinging electron with spin up, at $\mathbf{K}'$ valley, and retro reflected electron with spin down at $\mathbf{K}$ valley. c) RAR of an incoming electron with spin down, at K valley, and retro reflected electron with spin up, at $\mathbf{K}'$ valley. d) Schematics showing Brillouin zone, and related energies of RAR process explained shown in (b). (e) and (f) RAR for an incoming spin down electron in $\mathbf{K}$ valley, in presence of a magnetic field. (g) and (h) RAR for an incoming spin up electron in presence of an external magnetic field.

3 Experimental methods

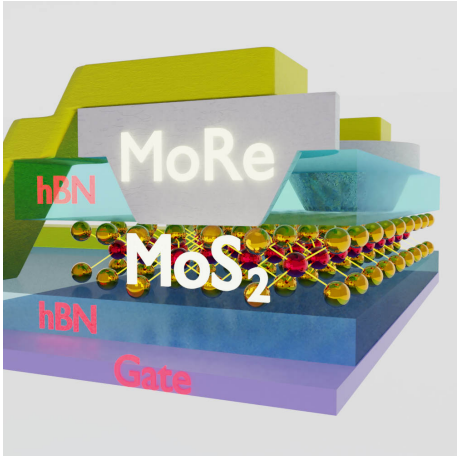

In this chapter, we give an overview of various approaches to fabricate galvanic contact to a monolayer molybdenum disulphide. We first develop normal contacts as a proof of concept. Using these techniques, we then establish superconducting contacts to monolayer molybdenum disulphide. We investigate the resistance area product, and carrier mobility of the bulk molybdenum disulphide obtained from different methods. We summarized all of our findings in table 3.11 to facilitate the comparison between the quality of different contacting approaches.

Moreover, we provide the basic fabrication method of VdW heterostructures. This includes exfoliation of layered materials and deterministic transfer of exfoliated flakes.

3.1. Fabrication of Van der Waals heterostructure

Layered materials are synthetic or naturally occurring crystals with intralayer covalent bonds and interlayer Van der Waals (VdW) interaction. The diverse family of layered material includes zero-band gap semiconductor such as graphene [1], electrical insulator like hexagonal boron nitride (hBN), large band gap semiconductor like molybdenum disulphide (MoS_2) [1], two-dimensional superconductors such as $NbSe_2$ [8], and topological insulator such as WTe_2 [9].

Due to relatively weak VdW force, one can isolate thin layer from the bulk crystals using electrochemical [62], chemical [63], or mechanical exfoliation [1] technique. In order to keep the surface chemistry of the crystals intact, the use of chemicals and solvents are to be avoided.

Using heterostructure of two-dimensional materials, one can engineer novel and unique optical, electronic, and physical properties [4, 64–69].

In the following chapter, we demonstrate the main techniques regarding mechanical exfoliation, and a deterministic transfer used in this project.

3.1.1. Mechanical exfoliation

Mechanical exfoliation is classified as a top-down fabrication method. Therefore, we rely on naturally occurring crystals of layered material, such as graphene and molybdenum disulfide, or synthetically grown hBN crystals.

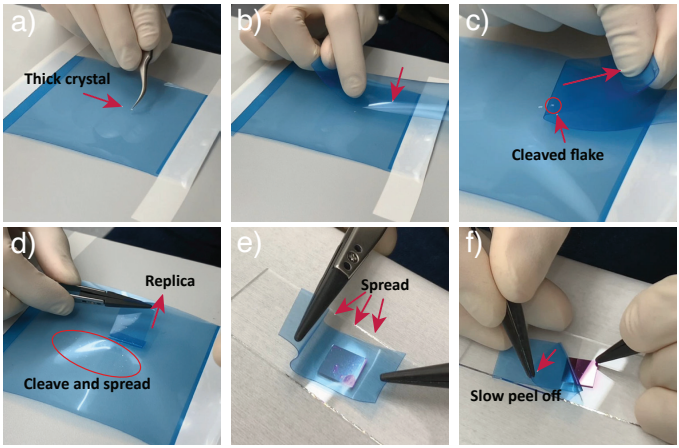

Figure 3.1. Illustration of a typical mechanical exfoliation. a) Fixing the sticky tape to the table, and depositing a thick crystal on the tape. b-c) Cleaving and spreading the bulk crystal on the surface of the tape. d) Use a new sticky tape in order to making a replica. e) Deposition of the exfoliated flakes on a silicon substrate. f) Peeling off the sticky tape from the silicon substrate. Some of these flakes eventually remain on the silicon substrate.

To start the exfoliation, first, we place a piece of thick crystal on top of an adhesive tape and press the crystal between two sticky tapes (see fig. 3.1(a, b)). As demonstrated in fig. 3.1(c, d), by pressing and peeling the tapes several times ($\sim$ 5-10 times), the crystals are gradually cleaved, thinned down, and spread on the tape. Tentatively, we can assume direct and indirect stress applied by the tape to the layered material overcomes the interlayer VdW force and leads to exfoliation.

After the cleaving is satisfying, we create a replica of the first tape using a fresh piece of tape (fig. 3.1(d)). Finally, we place a small piece of tape on a pre-cleaned silicon-silicon oxide substrate (285 nm) (see fig. 3.1(e)), then slowly peel the tape off the substrate at a shallow angle (see fig. 3.1(f)). The thickness of silicon oxide is chosen to increase the optical contrast under the white light of the microscope lamp[70, 71].

The thickness and quality of the exfoliated flakes are then characterized

using an atomic force microscope (AFM) in contact mode, and/or using an optical microscope. Ideally, we choose the flakes with no residue or crack on the top surface, that own a large surface area.

3.1.2. Deterministic transfer

The deterministic transfer is a combination of various techniques that are used to achieve a dry polymer-assisted transfer of layered material. For this, it is common to use a transfer stamp attached to a micro-manipulator. The transfer stamp often is a microscope glass slide that will be mounted to a micro-manipulator, a 5×5 mm thin film of 1-3 mm of polydimethylsiloxane (PDMS), that is covered with a polycarbonate (PC) thin film. The

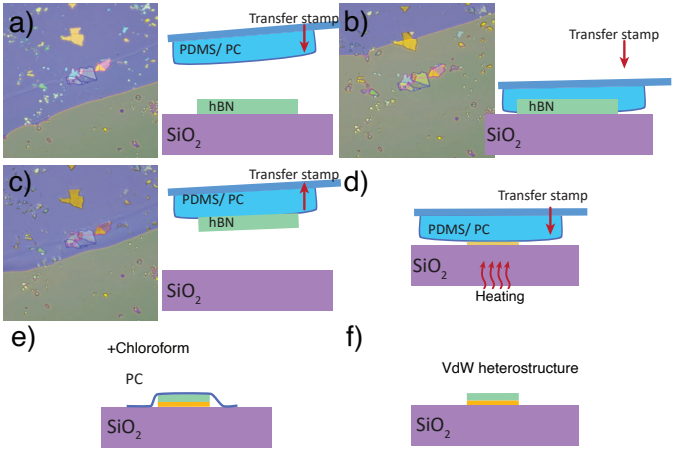

Figure 3.2. Schematics of deterministic dry transfer technique, with selected optical microscope image. a) Aligning the position and orientation of a flake and the transfer stamp. b) Lowering the transfer stamp at a stage temperature of $T \sim$ 70-90 °C to make contact with the substrate. c) Raising up the transfer stamp, and picking up the determined flake. d) Melting the PC film by heating the stage ($T \sim$150 °C. e) dissolving the sacrificial polymer layer. f) Completed heterostructure.

deterministic transfer is carried out inside the glove box, with a motorized stage, and motorized micro-manipulator. As shown in fig.3.2(a), we place the stamp on top of a pre-selected flake. Then the stamp is slowly brought into contact with the surface of substrate, while the stage temperature is kept at 70-90°C. By slowly lifting the transfer stamp, the identified flake

adhere better to the PC and comes off the silicon oxide substrate. This step could be repeated as desired until the designed heterostructure is completely fabricated (fig. 3.2(a-c)).

The PC-VdW heterostructure is then released irreversibly on a new silicon substrate by melting the PC film at 150 °C. Finally, after dissolving the sacrificial polymer layer using a strong solvent such as chloroform, or dichloromethane at room temperature for ∼1 h, the VdW heterostructure is completed and ready to be processed using further nanofabrication techniques.

3.2. Bottom contact fabrication

Bottom contact had been proven to be a powerful fabrication technique to study large bandgap semiconductor such as $MoSe_2$ [60], and MoS_2 [61]. It is facile, and flexible to be implemented for different nanostructure designs. The underlying idea is to first fabricate the lower part of the heterostructure, for instance, back gates and bottom insulator layer, and (bottom)contacts (see fig. 3.3(a-c)), followed by a cleaning process of the surface (see fig. 3.3(d)). Consequently, fabricating the upper part of the heterostructure including the study material, top insulating layer, and the top gate (see fig. 3.3(e, and f)). As demonstrated in fig. 3.3(d), the top surface of the contact interface is cleaned using a conventional AFM in contact mode. The polymer residue is pushed to the side of the scan area by the AFM tip (see also fig. 3.4(a)). Alternatively, oxygen plasma or thermal annealing are optional complementary cleaning steps after the AFM cleaning. However, oxygen plasma can change the surface chemistry of the contact, or even oxidise air-sensitive metals such as aluminium.

The upper part of the VdW heterostructure is fabricated in successive stacking steps, then transferred on top of the prefabricate contacts, inside the inert atmosphere of the glove box. The additional top gate structure is used to gate the contact interfaces and the bulk semiconductor from the top (see fig. 3.3(e, and f)).

Besides the advantage of a clean contact interface, the bottom contact technique provides a full/or top encapsulation of the active material. It has been demonstrated that encapsulation of two-dimensional materials with hBN screens charge traps, environment scatterers, and effectively reduces material degradation [72]. We have succeeded to establish bottom contacts of normal metals such as Au, and Pd, and bottom contacts based on MoRe which is a type II superconductor. In the next sections, we summarize our results for Au, and MoRe bottom contacts.

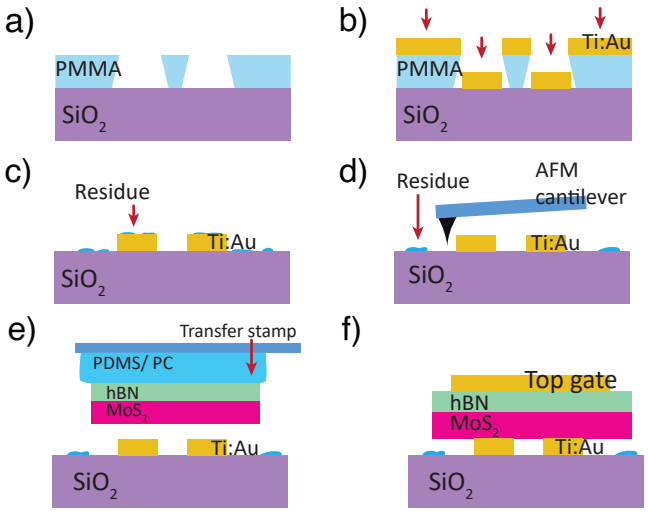

Figure 3.3. Schematics of fabrication steps of bottom contacts: a) Patterning the bottom contact structure using electron beam lithography. b) Metal deposition. c) Remaining polymer residue after the lift-off process. d) AFM cleaning. e) Stacking the heterostructure inside the glove box. f) Deposition of the top gate and finalized structure.

3.2.1. Au bottom contact

As stated previously, after metal deposition there is a thin layer (∼5 nm) of polymer residue on the surface after the lift off using a conventional solvent such as acetone. We pushed these residues away from the contact interface using the AFM tip. Figure 3.4(a) shows AFM micrographs in tapping mode before and after cleaning. The scan speed and feedback force are carefully chosen to minimize any damage to the surface. The bright spots in the figure are the polymer residues accumulated along the edge of the cleaned area. This step can take anything between 2-6 hours, depending on the amount of residue, and nanostructure design. This structure is stored inside the glovebox to be used in the next fabrication steps. The exfoliation and deterministic transfer is done inside the glove box environment.

Figure 3.4(b) shows a four-layer MoS_2 equipped with Ti:Au (7:20 nm) bottom contacts. The accumulation of polymer residue is visible. Finally, two sets of metallic top gates (Ti:Au) are fabricated using conventional e-beam lithography and deposition method. The top gate (TG, indicated by yellow area in fig. 3.4(c)) is used to electrically gate the bulk of MoS_2, and the contact gates (CGs, indicated by the red area) is used to gate contact areas.

Here we discuss preliminary measurements of the device shown in fig. 3.4(c), measured in a variable temperature insert (VTI) at T_{base}= 1.7 K. A two-terminal differential conductance of C_1,C_2 as a function of top gate voltage, at indicated contact gates V_{CG}=5 & 9 V, a finite back gate voltage V_{BG}=9 V, and at zero bias voltage is plotted in fig. 3.4(d). The overall characteristics is attributed to an n-type semiconductor. The measurement shows a linear characteristic at intermediate top gate voltage. At voltages V_{TG} <-1 V, the bulk of the semiconductor is depleted from electrons, and we do not see any conduction at more negative values, due to the large bandgap, and mid-gap trap states in MoS_2 [73]. The saturation of conductance at higher gate voltages could be intuitively attributed to the resistance of area between TG and CG (∼ 50 nm), in which the bulk MoS_2 which is not gated effectively. Using multi-terminal measurements, we extracted contact resistance of R_{c}= 29 kΩ, where two-terminal resistance is $R_{2\mathrm{t}}$= 60 kΩ (V_{SD}=5 mV, V_{TG}=9 V). Taking into consideration the two-terminal measurements, the resistance area product is RA= 600 kΩμm^2.

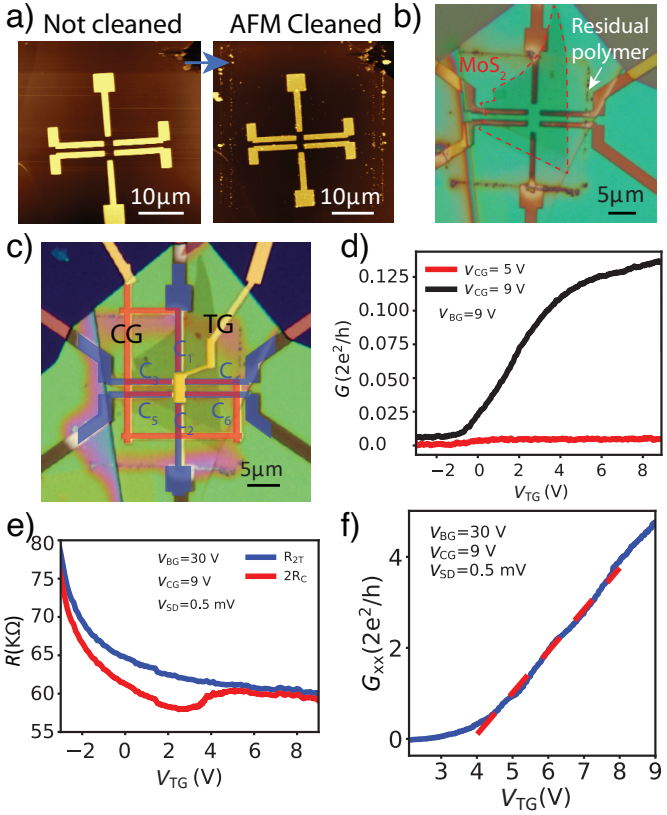

Figure 3.4. a) AFM micrographs of the contact area acquired before and after the AFM cleaning. The accumulation of polymer residue is evident. b) Optical microscopy image of the heterostructure. The outline of MoS_2 is indicated by a red dashed line. The accumulation of polymer residue is indicated by a white arrow. It is buried under the top-hBN and leads to a rectangular halo around the contacts. c) False colour optical micrograph of a multilayer MoS_2 with bottom Au contacts. 6 pairs of contacts are shown in purple, top gate in yellow, and contact gates in orange areas. d) Two-terminal differential conductance between C_1,C_2 as a function of top gate. e) Two-terminal resistance and contact resistance as a function of top gate voltage. The bias voltage is applied to C_1 while C_2 is electrically grounded, and the voltage drop is measured between C_3-C_5. f) Four terminal differential conductance of G_{xx}=dI_{12}/dV_{35} as a function of top gate which is corresponding to the bulk conductance of MoS_2. The red dashed line is a linear fit used to extract field effect mobility.

We use Drude model to extract the effective mobility from these set of measurements. The expression for the field effect mobility reads $\mu = (\mathrm{d}G/\mathrm{d}V_\mathrm{G})(L_\mathrm{ch}/W_\mathrm{ch}C)$, where G is conductance $G = I_\mathrm{SD}/V_\mathrm{xx}$, $\mathrm{I_{SD}}$ is the current passing from source to drain contact, $\mathrm{V_{xx}}$ is the voltage drop across voltage probes. The geometric capacitance C is calculated using the parallel plate capacitor model $C = \varepsilon_0 \times \varepsilon_1/d_\mathrm{dielectric}$, where $\varepsilon_0 = 8.854\times10^{-12}$ is vacuum permittivity. Using the above equation and the linear fit plotted in fig. 3.4(d) we calculated field effect mobility up to $1700\,\mathrm{cm}^2/\mathrm{Vs}$ at an electron density of $3\times10^{12}\,\mathrm{cm}^{-2}$ at $T_\mathrm{base} = 1.7\,\mathrm{K}$.

3.2.2. MoRe:Pt bottom contact

Despite the reliable bottom contact to 2D-semiconductor, this technique does not support contacts made out of air sensitive metals, including Al, and V. This is due to the exposure of the contact material to the ambient conditions during AFM cleaning. To minimize the oxidation of contact material, one can make use of an inert metal as a capping layer. Despite our intense effort, aluminium based devices that are capped in situ with Au, or Pd still suffer from partial oxidation and show no electrical connection at room temperature (see table 3.11). On the other hand, MoRe (with a work function ∼4 eV [74]) is more stable in ambient conditions and therefore a good candidate.

Figure 3.5(a) shows optical microscopy image of a monolayer MoS_2 device with bottom contact of MoRe:Pt (30:4 nm). Finally, a global metallic top gate is deposited on top of the hBN.

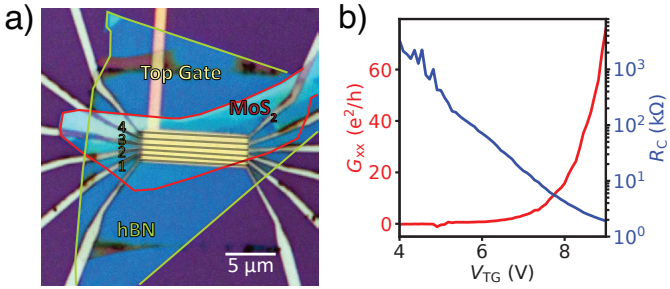

Figure 3.5. a) Optical micrograph of monolayer MoS_2 with bottom MoRe:Pt contacts. The rectangular contact pairs are shown by grey shade, labelled by numbers and used in the main manuscript as such. The boundary of MoS_2 flake is shown by the solid red line. b) Red is the four terminal differential conductance $G_{xx} = dI_{14}/dV_{23}$ as a function of top gate voltage, at finite bias voltage V_{SD}=5 mV. Blue is the contact resistance as a function of top gate voltage in log scale, at finite bias voltage V_{SD}=5 mV.

The electrical transport measurements are carried out in a VTI with T_{Base}= 1.7 K, using conventional lock-in techniques. In a multiterminal measurement, a bias voltage is applied to C_1, current passing from C_4 to ground is measured, and the voltage drop across contact C_2-C_3 is measured. The resulting differential conductance G_{xx}=dI_{14}/dV_{23} at finite bias voltage V_{SD}=5 mV, is plotted in fig. 3.5(b) solid red line. We find the two-terminal resistance of $R_{2\mathrm{t}}$= 4 kΩ, and resistance area product of RA=13.5 kΩ.μm^2 for C_1 while C_4 contact pair. Moreover, the contact resistance is calculated using a simplified formula $2R_{\mathrm{c}} = R_{2\mathrm{t}} - R_{\mathrm{xx}}$=2 kΩ, at V_{SD}=5 mV, and V_{TG}=9 V. Here R_{xx} is the bulk MoS_2 resistance. Accordingly, the contact resistance is plotted in log scale in fig. 3.5(b) solid blue curve.

Furthermore, we calculated the field effect mobility of 100 cm^2/Vs at an electron density of 3×10^{12} cm^{-2}.

In conclusion, bottom contacts of normal metal such as Au, or superconducting contacts such as MoRe, is a viable contacting method, and show reasonable mobility and contact resistance. Despite our intense efforts, we realized pristine MoRe cannot be used as bottom contact. This includes incorporating AFM cleaning, reactive ion cleaning, thermal annealing in vacuum/or forming gas. We intuitively attribute this to the partial oxidation of MoRe. This may as well explain why Al (as a type I superconductor) is not a good candidate as bottom contact due to its high oxidation rate in air. For comparison of different approaches see table 3.11. Details fabrication parameters can be found in appendix A.

3.3. VIA contact fabrication

The concept of vertical interconnect accesses (VIA) is an established technology in circuit electronics. It allows electrical connections to high-density arrays through the insulating substrate material. The adapted technology in VdW heterostructure is defined as connecting the material of interest through electrical contacts that are embedded into the insulating hexagonal boron nitride [75]. This technique preserves the pristine properties of the materials and keeps the interface polymer-free. Besides, a full encapsulation prevents material degradation of the air-sensitive materials. Moreover, in the fabrication of superconducting VIA contacts, there is no need for the use of a wetting/capping layer of the contact interface. In this section, we demonstrated the fabrication of normal metal and superconducting VIAs. The fabrication steps of a typical VIA contact is demonstrated in fig. 3.6.

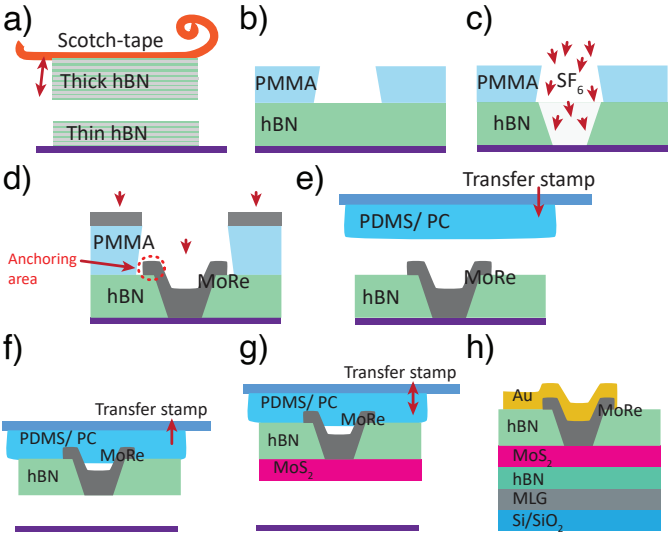

Figure 3.6. Schematics of various steps in the fabrication of a MoRe VIA contacts: a) Exfoliation of hBN on silicon dioxide substrate. b) Pattering the contact area using electron beam lithography. c) Etching the hBN using reactive ion etching technique. d) Repeating the patterning of the contact area plus anchoring area, followed by the metal deposition. (e) and (f) Pick up of VIA-hBN using a transfer stamp inside the glovebox. g) Stacking other VdW flakes using the same transfer stamp. h) Finished device with electrical leads connected to VIA contacts.

First, an hBN layer is exfoliated on top of a pre-cleaned silicon dioxide substrate. We determine hBN with a thickness of 20-40 nm, and an area of roughly 20*20 μm. Contact area and some alignment markers are patterned on top of this hBN using electron beam lithography. The as-defined contact area is etched away using reactive ion etching with a SF_6:O_2:Ar (20:5:5 sccm) gas mixture (see fig. 3.6(c)).

This guarantees a selective etch of hBN compared to silicon oxide. After the lift-off process in a warm acetone bath, a secondary electron beam lithography is used to pattern a slightly larger contact area with the etched structure in the centre. Then, after a mild oxygen plasma for 5 s, desired metal is deposited on top with a thickness 10% thicker than the corresponding depth of these holes (see fig. 3.6(d)). We realized that an AFM cleaning of the top surface can help to clean up the side depositions, and polymer residue, therefore, helps with the next pick step. The secondary patterning and deposition further improve the mechanical stability of VIA contacts, by anchoring the metal to the top of hBN. As shown in fig. 3.6(e-g), using deterministic transfer inside the glovebox we pick up other VdW flakes to complete the desired heterostructure. Finally, the heterostructure is released on a silicon oxide substrate, and electrical leads are patterned and deposited to connect the VIAs to the measurement pads.

The success rate of VIA fabrication varies and depends on the design of the contact, materials of choice, anchoring area (overlap on the hBN). Figure 3.7 shows scanning electron microscopy images of VIA fabrication. The most common challenge is that the VIA contacts often adhere so strongly to the silicon oxide that during pickup of hBN they crack and separate from the hBN; which means deposited metal remains on the silicon oxide substrate, and hBN is picked (see fig. 3.7(a, d, and f)). In other cases, the VIA contacts could be picked up, but partially moved from their position, impaired and leaving a gap between the electrical lead, and MoS_2 (see fig. 3.7(b)). The three top contacts are in place, and the three lower contacts are impaired. This is in agreement with the electrical measurement of the same sample where there is no electrical connections through the impaired contacts.

As mentioned before, creating an anchoring around the VIAs (overlap on top of hBN) significantly improves the mechanical stability of the hole structure. This is very effective for Au and MoRe based VIAs, albeit did not help for the Al based VIAs. Figure 3.7(c) shows an Al based VIA contacts (before transfer) embedded in hBN, and equipped with a large anchoring area. Based on our observation: during the pick up of the Al-based VIAs, the contacts suffer from brittleness and break off. Figure 3.7(d) shows those rectangular contact area that are left behind on top of SiO_2, while hBN and anchoring area are picked up successfully. In circular Al based VIAs (fig. 3.7(e)) we observe a similar pattern. The rim corresponds to the anchoring

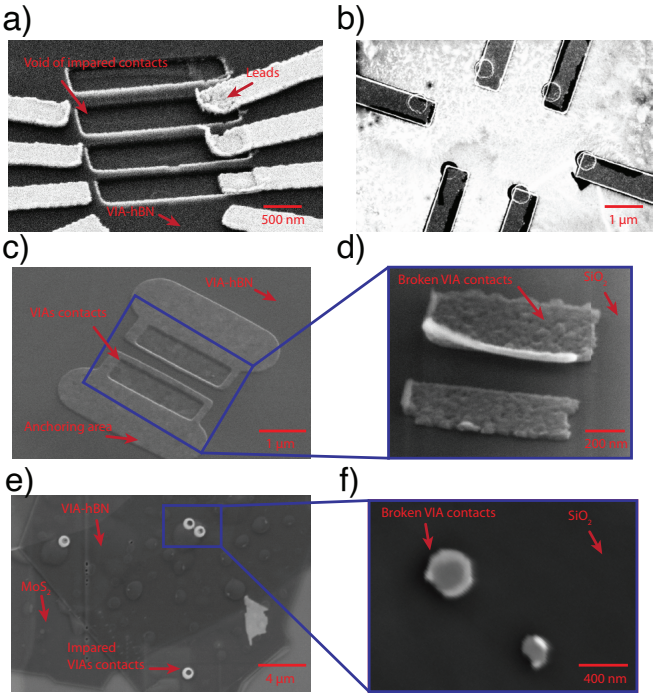

Figure 3.7. SEM micrographs of VIA contacts and VIA devices, demonstrating different designs, and faults during the process. a) Completed VIA device, where VIA contacts are broken off the VIA-hBN, and holes are left behind. b) Completed VIA device with intact and impaired VIA contacts. c) SEM micrograph of the pristine VIAs that are as fabricated on top of the VIA-hBN. The whole structure is placed on to of a silicon dioxide substrate. d) SEM micrograph acquired after the pick up of VIA-hBN, show the rectangular part of VIA contact that is broken off. e) A completed Al-based VIA device with circular contacts. All contacts are broken off in the middle. f) After the pick up of VIA-hBN, showing circular part of VIA contact that are broken off.

area (which are on top of hBN), and the hollow part in the middle is the contact area that is broken off the structure. Figure 3.7(f) is a SEM image from the silicon substrate: showing the broken VIAs after the failed pick-up process.

Another parameter that affects the yield is the contact area. In Au and

MoRe devices (mainly with a circular contact area) we limited the contact diameter to 300-700 nm, while the anchoring area is 400-800 nm.

In the following sections, we discuss the basic characterization of Au, and MoRe based VIA contacts. Both Au and MoRe are good materials of choice, thanks to high mechanical stability.

3.3.1. Normal metal VIA contact

An optical microscopy image of a typical Au based VIA contact to a monolayer molybdenum disulfide is shown in 3.8(a). Although at room temperature five contacts (indicated by numbers in the optical image) show gate tunable conductance, yet only C_1, C_2, and C_3 sustain a two-terminal resistance lower than 1 MΩ at cryogenic temperatures. This device is measured electrically in a VTI refrigerator at T_{base}=1.7 K and measured optically in a dry VTI refrigerator with optical access and base temperature of T_{base}=1.4 K.

This device owns two graphite gates, used as back and top gate in order to tune the chemical potential in the device. Surprisingly, the effect of the top gate on the characteristic measurements is small at all gate voltage regimes. The lever arm for the back gate is many times larger than the top gate ($> 10^6\times$). We propose that this could be due to the difference in the dielectric thickness of the bottom hBN ∼18 nm compared to top hBN ∼50 nm.

On the other hand, the back gate is effective in tuning the Schottky barrier and chemical potential in the bulk MoS_2. Figure 3.8(b) red solid line shows the two-terminal differential conductance of contact pairs C_1-C_2 in respect to the back gate voltage, at $V_{\text{SD}} = 0$. This results in a total resistance of 180 kΩ at high gate voltage. Using three terminal measurements we could extract the contact resistance of the working contacts. The results are listed in table 3.1, and indicate variations in the contact resistance. This variation could be due to the mechanical instability of the VIA's during the fabrication that leads to an inhomogeneous interface, different transparency. Another possible explanation could lie in the asymmetry in the current path, which results in an overestimation of contact resistance.

Contact number	Resistance kΩ	Resistance unit area (kΩμm^2)
Contact 1	150	120
Contact 2	20	16
Contact 3	140	112

Table 3.1. Contact resistance of various Au VIA contacts.

Details of the magnetoconductance and optical measurements of this particular sample is the subject of chapter 4.

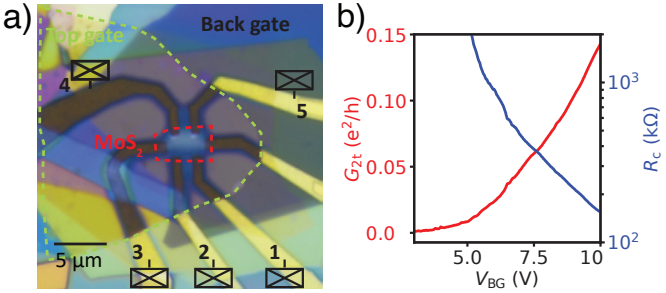

Figure 3.8. a) Optical microscopy image of a monolayer MoS_2 with Au VIA contacts. The boundary of MoS_2 flake is shown by dashed red line. b) Red: two-terminal differential conductance $G_{2t} = dI_{12}/dV_{12}$ between C_1,C_2 as a function of back gate voltage. Blue: Measured contact resistance of contact C_1 as a function of back gate voltage in log scale ($V_{SD} = 0$).

3.3.2. Superconducting VIA contact

We fabricated MoRe VIA contacts to a monolayer molybdenum disulfide (see fig. 3.9(a)). The deposition of MoRe is carried out in a UHV system, without the need for a wetting layer. Only four out of eight contacts (indicated by numbers in the optical image) sustain a two-terminal resistance lower than 1 MΩ at cryogenic temperatures. This device is measured in a VTI at a base temperature of T_{base}= 1.7 K, and in a dilution refrigerator at base temperature of 50 mK.

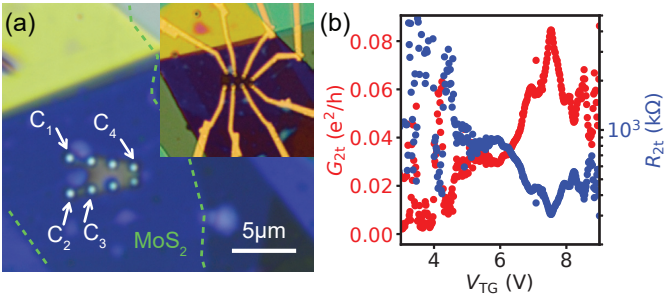

Figure 3.9. a) Optical microscopy image of a monolayer MoS_2 with MoRe VIA contacts. The boundary of MoS_2 flake is shown by a green dashed line. Inset shows the final device with the measurement leads. b) Red: two-terminal differential conductance $G_{2t} = dI_{23}/dV_{23}$ between C_2-C_3 as a function of back gate voltage. Blue: Two-terminal differential resistance of C_2-C_3 as a function of back gate voltage in log scale (at V_{SD} =5 mV).

Contact pair	Resistance kΩ
C_1- C_2	60
C_2- C_3	430
C_3- C_4	516
C_2- C_4	140

Table 3.2. Two-terminal resistance between different contact pairs of MoRe based VIA contacts, at V_{SD} =5 mV, and T_{base}= 1.7 K.

As shown in fig. 3.9(b), the back gate is effective in tuning conductance of the sample: the red solid line shows the two-terminal differential conductance of contact pairs C_2-C_3 in respect to the back gate voltage, at V_{SD} =5 mV. This results in a total resistance of $\sim$ 430 kΩ at high gate voltage.

There is a variation in the two-terminal conductance of different contact pairs, as shown in table 3.2.

Details of the transport measurement and magnetoconductance of superconducting VIA contacts is the subject of the chapters 5, and 6.

3.4. Van der Waals contact fabrication

The study of VdW hybrid system has been one of the most promising fields in the recent years. Study shows that graphene can be reliably used as a contact material to two-dimensional semiconductors including TMDCs. This method allows a full encapsulation of the VdW heterostructure, atomically flat and (potentially) clean contact interface. For instance, graphene can be used as contact material to other VdW materials, and measurement along heterojunction, or homojunction is possible [76–78]. Graphene with an atomically flat surface, a low defect density, and a tunable chemical potential assure enhanced charge injection to the semiconducting material. One of the early studies that leveraged this technology reports a record quantum mobility of 1400 cm^2/Vs and a quantum scattering time of τ_q= 176 fs using a CVD-grown monolayer molybdenum disulphide [76]. In the same study, a multi terminal measurement in presence of an external magnetic field reveals hall mobility of 1000 cm^2/Vs. Recently, the Josephson effect had been reported in planar graphene-$NbSe_2$ devices [79, 80]. Moreover, a signature of specular interband Andreev reflection has been observed in graphene-$NbSe_2$ hybrid system [81].

In this chapter we report fabrication of a $NbSe_2$:graphene VdW contact to monolayer MoS_2. $NbSe_2$ is a two-dimensional superconductor down to monolayer limit [8]. Our goal here is to investigate the induced superconducting proximity effect from a two-dimensional superconductor to a two-dimensional semiconductor. The fabrication of such a device is challenging since $NbSe_2$ is an air-sensitive material, and the conventional fabrication method leads to severe material degradation [75]. Here we established a novel method to minimize the surface oxidation of $NbSe_2$, and fabricated it under ambient conditions.

First, Au bottom contacts (Ti:Au 5:20 nm) are fabricated on silicon dioxide substrate, with three leads namely terminal C_1, C_2, and C_3. Then, we exfoliated $NbSe_2$ and graphene flakes inside the glove box atmosphere. Using conventional transfer technique (inside the glove box), a monolayer graphene flake, and a $NbSe_2$ (∼15 nm thick) is picked up and transferred on top of the prefabricated Au bottom contacts (see fig. 3.10(a)). The role of graphene is to protect $NbSe_2$ from above.

Subsequently, a few trenches (∼ 150 nm wide) is patterned and etched away using reactive ion etching. The goal is to electrically disconnect contacts C_2 and C_3 (see fig. 3.10(b)). The electrical decoupling between C_2-C_3 is ensured by the measurements at room temperature.

Next, a monolayer MoS_2 is picked up using an hBN layer (19 nm thick) and transferred on top of the etched trench. In fig. 3.10(c) the boundaries of the MoS_2 flake is shown by red dashed line. Finally, a metallic top gate is fabricated above the encapsulated MoS_2 flake (see fig. 3.10(d)).

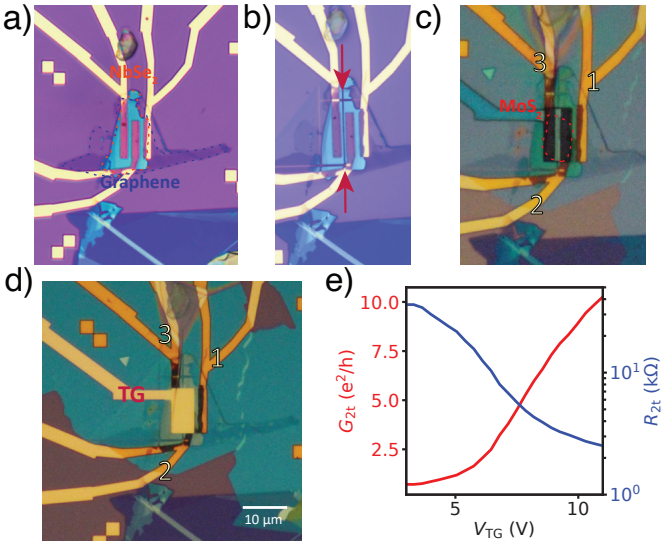

Figure 3.10. a-d) Optical microscope images of various fabrication steps of a MoS_2-graphene:$NbSe_2$ device. a) Au bottom contacts with graphene:$NbSe_2$ placed on top. b) The etched area between the contacts for electrical decoupling. c) Transfering hBN:MoS_2 flakes on top of the structure. d) Fabrication of top gate. e) Two-terminal differential conductance (in red) and differential resistance (in blue) as a function of top gate voltage. The measurement is carried out between C_2-C_3, at finite DC bias voltage of V_{SD}= 5 mV.

The electrical transport measurements are performed in a dilution refrigerator with an external magnetic field perpendicular to the device plane at a base temperature of T_{base} = 50 mK. We would like to note that measurements between C_1-C_2 is used to confirm superconductivity in $NbSe_2$, whereas in between C_2,C_3 is used to measure the contribution of bulk MoS_2. Two-terminal differential conductance of C_2-C_3 as a function of top gate voltage at finite voltage bias of V_{SD}= 5 mV is plotted in fig. 3.10(e) using a solid red curve. The measurements show gate tunable characteristics of the conductance which is attributed to the MoS_2. The total differential resistance of the same contact pair is plotted in solid blue curve. In order to break down different contributions in this measurement we provide a

simplified picture of the resistors in series for this measurement as:

$$R_{2\mathrm{t,C_1C_2}}(V_{\mathrm{TG}}) = \\ 2R_{\mathrm{c,NbSe_2:Au}} + 2R_{\mathrm{c,NbSe_2:gr}} + 2R_{\mathrm{c,gr:MoS_2}} + R_{\mathrm{NbSe_2}} + R_{\mathrm{MoS_2}}(V_{\mathrm{TG}}), \tag{3.1}$$

Where $R_{\mathrm{c,NbSe_2:Au}}$ is the contact resistance of $NbSe_2$ with Au, and $R_{\mathrm{c,gr:MoS_2}}$ is contact resistance between graphene and MoS_2 interface, $R_{\mathrm{NbSe_2}}$ is resistance through the bulk of $NbSe_2$, and $R_{\mathrm{MoS_2}}$ is the resistance of bulk MoS_2 which is a function of top gate voltage.

Besides, the two-terminal resistance between C_1-C_2 which can be written as $R_{2\mathrm{t,C_1C_2}} = 2R_{\mathrm{c,NbSe_2:Au}} + R_{\mathrm{NbSe_2}}$. After accounting for the measurement line resistance we find $R_{2\mathrm{t,C_1C_2}} = 2\Omega$, which indicates the intrinsic superconductivity in $NbSe_2$. Proving the superconducting nature of $NbSe_2$; we neglect the small resistances including $R_{\mathrm{NbSe_2}}$, $R_{\mathrm{c,NbSe_2:Au}}$, and $R_{\mathrm{c,graphene:NbSe_2}}$ for further calculations. Taking these assumptions, the two-terminal resistance between C_2C_3 is mainly the bulk resistance of MoS_2 $R_{\mathrm{MoS_2}}$, and contact resistance $R_{\mathrm{c,graphene:MoS_2}}$. The total resistance at $V_{\mathrm{TG}} = 11V$ is $R_{2\mathrm{t}} = 40\mathrm{k}\Omega$, and resistance area product of RA$=200$ $\mathrm{k}\Omega.\mu\mathrm{m}^2$.

In conclusion, graphene:$NbSe_2$ based VdW contacts to two-dimensional material is a very promising technique, especially with the advancement of fabrication techniques [77, 82]. Details of the transport measurement, and magnetoconductance of this particular sample is the subject of chapter 4 of this manuscript.

3.5. Edge contact fabrication

One dimensional contact also known as edge contact is a very effective method to fabricate nanoelectronic devices with flexible design [72]. This method outperforms conventional top contact and preserves the pristine properties of two-dimensional material for ballistic transport in graphene over more than 15 μm at low temperatures. This technique is originally developed for graphene [72], and later on was leveraged in small-bandgap semiconductors such as WTe_2. Nevertheless, it has not yet been proven effective for the large gap semiconductors such as MoS_2.

The edge-contact is a one-dimensional object, and susceptible to material degradation. Moreover, this may lead to in-gap charge trap states and consequently pinning of Fermi level inside the semiconducting gap [73]. It has been shown that extensive Ar-milling of contact area and a following in situ metal deposition can be deployed to achieve edge contact to MoS_2 [83]. Nevertheless, our attempts to establish edge contacts to a monolayer MoS_2 with normal metal Ti:Au, or superconducting metals such as MoRe did not succeed. As shown in table 3.11, the room temperature resistance of such devices is >2 MΩ. At liquid helium temperature, the contact resistance is orders of magnitude larger, and it dominates the electrical transport measurements.

In conclusion, our attempts to fabricate edge contact to MoS_2 had not been successful.

3.6. Top contact fabrication

The most intuitive method for the fabrication of contact is known to be top contact. In the case of the two-dimensional material, it is carried out by coating a resist polymer layer on top of an exfoliated flake, patterning the top contacts using electron beam lithography, and then depositing the contact material on top, followed by the lift-off process. One can use a dopped silicon back gate, or additional local gates in order to change the chemical potential in the system [7, 84]. This technique results in a room temperature mobility μ= 200-5000 cm^2/Vs for thick crystals of MoS_2 [85], 0.1-50 cm^2/Vs for monolayer MoS_2 exfoliated on silicon substrate [86], and up to ∼180 cm^2/Vs for monolayer MoS_2 with gating using high dielectric constant materials [7, 84]. Using this technique, a multi terminal field effect mobility of ∼180 cm^2/Vs at 4 K is reported in ref. [7]. Moreover, a multi terminal field effect mobility of 1000 cm^2/Vs and hall mobility of 250 cm^2/Vs at 5K was reported in ref. [87].

These early attempts demonstrate the versatility of the top contact technique. Nevertheless, large contact resistance is common, which is attributed to two effects: The Schottky barrier formation at the contact interface, and back scattering of the charge carrier in the conductance channel. The latter can be addressed by the encapsulation of two-dimensional materials in insulating hexagonal boron nitride. This is technically incompatible with top contact fabrication, due to the electrical insulation. Since all-around encapsulation is not possible, the polymer residue which is accumulated on top of the two-dimensional semiconductor leads to many scattering events and has an adverse effect on the mean free path and mobility of the device [88]. In addition, the contact interface is always contaminated with the e-beam resist and other solutions during the fabrication [25]. This could be the main reason for the discrepancy between the calculation of the Schottky formation and experimental findings. Therefore in this project, we have not investigated the fabrication of top contact to two-dimensional semiconductors.

3.7. Conclusions

Table 3.11 summarizes our findings regarding different types of contact fabrication. We have tried each fabrication process multiple times, in order to ensure our findings. As shown in the below table, a low resistant contact pair that is based on superconducting material requires a careful choice of materials. In the following chapters, we will discuss the optical and electrical measurements of those devices with working contacts.

Type	Failure analysis	Material	R_2t (kΩ) (RT)	R_2t (kΩ) (LT)	RA (kΩ.μm2)
VIA	-	Au	500	180	144
VIA	Mechanical instability of VIAs	Au	>2000	NA	NA
VIA	-	MoRe	400	200	28
VIA	-	MoRe	700	430	54
VIA	Mechanical instability of VIAs	Al_Pd	NA	NA	NA
VIA	Mechanical instability of VIAs	Al-Au	NA	NA	NA
VIA	Mechanical instability of VIAs	Al	NA	NA	NA
VIA	Mechanical instability of VIAs	V	NA	NA	NA
VIA	Mechanical instability of VIAs	NbTi	NA	NA	NA
B.C.	-	MoRe-Pt	25	4	13.6
B.C.	Contamination	MoRe-Pt	1400	NA	NA
B.C.	Oxidation (assumption)	MoRe	>3000	NA	NA
B.C.	-	Au(Ti-Au)	400	60	600
B.C.	-	Pd	>1000	NA	NA
B.C.	Oxidation	Al_Pd	NA	NA	NA
VdW	-	NBSe2	400	2.7	200
VdW	-	graphene	NA	NA	NA
Edge	Oxidation + Contamination	MoRe	>2000	NA	NA
Edge	Oxidation + Contamination	Au	>2000	NA	NA

Figure 3.11. A general overview of the various contacting approaches, colour coded for successful and failed attempts. The failure analysis is our interpretations based on multiple attempts of each technique.

4 Optical and electrical measurements

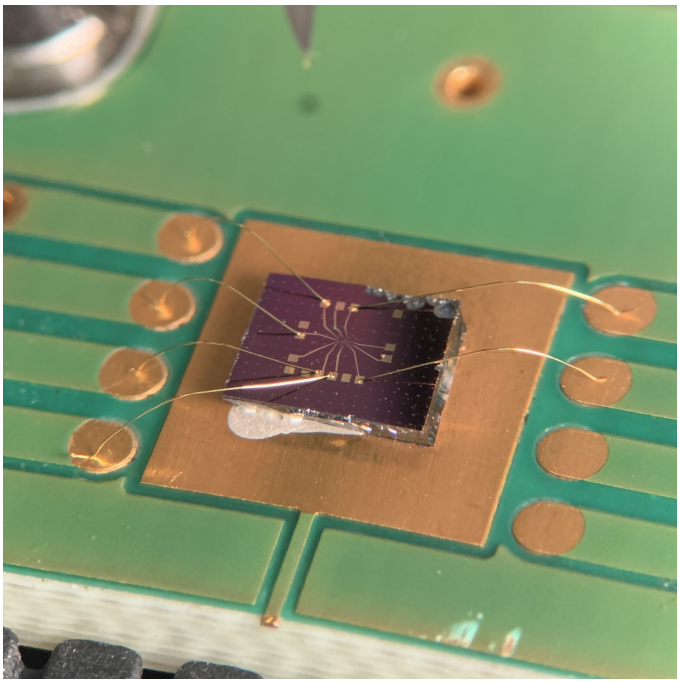

In this chapter we discuss the low temperature optical and electrical measurements of molybdenum disulphide devices. Using optical measurements we studied the characteristics of neutral exciton, and charged exciton in respect to chemical potential. Moreover, using magnetotransport measurements we observe Landau level quantization in the bulk of molybdenum disulphide. We demonstrate that in all fabrication methods, the quality of bulk molybdenum disulphide is preserved. In case of superconducting contacts, we observe a signature of superconducting contacts in the measurements.

4.1. Optical measurements

Here we discuss the optical characterisation of molybdenum disulphide device with Au VIA contacts that is shown in fig. 3.8(a) at low temperature (T_{base}= 1.4 K). We mainly discuss the photoluminescence (PL) in respect to the back gate voltage. In doing so, we use a collimated red laser beam with photon energy of 1.959 eV, and power of 600 μW (relatively high power), and no circular polariser in the beam path. The laser energy is slightly above the energy corresponding to the A exciton, and well below B exciton of molybdenum disulphide. A few of the adverse effects of using a high laser power on the optical measurements includes populating the semiconductor with copious amount of excitons, photo-bleaching, photo doping, non-linearity, and potentially hysteresis in the measurements. Nevertheless, we have not observed any hysteresis in PL measurements as a function of back gate voltage, or the direction of voltage sweep, or the exposure time.

Figure 4.1(b) shows PL intensity at different photon energy, and back gate voltage. The green dashed lines and numbers are used in the rest o this chapter for the interpretation of the features.

The bright feature at around 1.93 eV (box i in fig. 4.1(b), and (c)) is attributed to the neutral exciton (A exciton, or X^0) [89] of MoS_2. This is the energy associated to the recombination of the bound exciton, which is the bound state of a hole in valence band and an excited electron in the conduction band. For negative gate voltages $V_{\text{BG}} < 0$ there is no gate dependence (fig. 4.1(c)), whereas for $V_{\text{BG}} > 0.1\,\text{V}$ the intensity of the neutral exciton decreases significantly. Moreover, for $V_{\text{BG}} > 0.1$ the neutral exciton shows a blue shift, similar to the findings in ref. [90], where the authors attribute this shift to band renormalization. In fig. 4.1(c), there is a peak at $\sim$1.925 eV which could be due to non-ideal low pass filtering of the laser line. Quite expectedly, this feature is not gate tunable.

The feature that appears at $0.1 < V_{\text{BG}} < 5\,\text{V}$ (box ii in fig. 4.1(b), and (d)), at around 1.89 eV is attributed to the negatively charged exciton (trion, or X^-), where the free electron is populating the two lower spin orbit split subbands of molybdenum disulphide. A negative trion consists of two electrons in the conduction band and in a spin-singlet state and a hole [90, 91]. Similar to an exciton, there is a binding energy attributed to the bound trion. The trion peak dissappears at higher gate voltage (i.e. high carrier density).

The other feature appears at $5 < V_{\text{BG}}\,\text{V}$ corresponding to $n = 4.1 \times 10^{12}\,\text{cm}^2/\text{Vs}$ (box iii in fig. 4.1(b), and (e)), at energies 1.87-1.88 eV. This peak is attributed to a Mahan-like exciton [90], or an exciton-plasmon-like excitation [92], and the exact origin of it is still under debate. Mahan exction shows a redshift in the corresponding PL signal in respect to the neutral exciton.

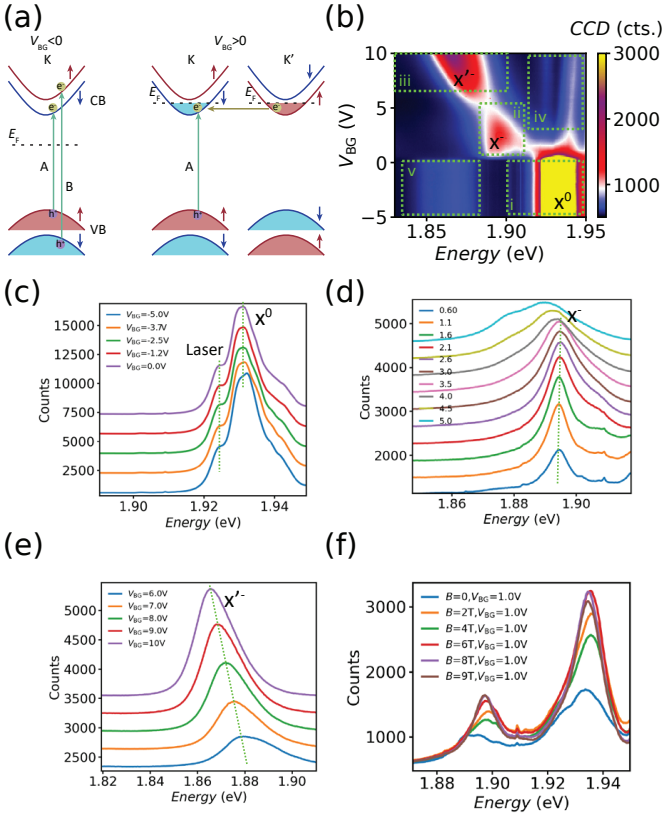

Figure 4.1. a) Schematics of neutral exciton and negatively charged exciton (trion) in bandstructure of MoS_2. b) Spectrometer counts in respect to the back gate voltage and energy of the emitted PL. c) PL spectrum with respect to indicated back gate voltage, showing the energy of neutral exciton X^0. d) Evolution of negatively charged exciton X^- as a function of the back gate voltage. e) Evolution X'^- with respect to gate voltage. f) Evolution of X^0, and at slightly smaller energy X^- with respect to external magnetic field. All the curves in (c-e) are manually offsetted for clarity.

The broad feature that is indicated by v in fig. 4.1(b) could be attributed to defect states in the band gap of MoS_2. This peak vanishes once the conduction band is populated.

Figure 4.1(f), shows the evolution of neutral exciton, and charged exciton as a function of external magnetic field. The neutral exciton shows a change in its amplitude, at constant energy. However, the trion peak shows a red shift, and and increase of PL intensity. We tentatively attribute this to Zeeman shift.

4.2. Normal metal VIA contact

In this section, we give an overview of the magneto transport measurements of a monolayer molybdenum disulphide, contacted with Au based VIA contacts, demonstrated previously in fig. 3.8(a).

Figure 4.2(a) shows change in differential conductance amplitude $\Delta G = G - f$ at various gate voltages and perpendicular magnetic fields. the function f is a polynomial background which accounts for the classical hall effect and contact resistance variations in the two terminal measurements. The amplitude modulation is clearly attributed to the Landau fans evolving in magnetic field. In a non-interactive picture, and at high carrier densities ($n > 4.1 \times 10^{12}\,\mathrm{cm}^2/\mathrm{Vs}$), all the four subbands are occupied [61]. Therefore, Landau fans originating from two lower subbands (fig 4.2(b) black dashed lines), and two upper subbands (4.2(b) cyan dashed lines) co-exist in this gate voltage regime. The interference of these Landau fans leads to the chequerboard pattern of fig. 4.2(a). The onset of oscillations indicates $\omega_c > 1/\tau$ in which the cyclotron frequency ($\omega_c = eB/m^*$) is larger than inverse scattering time (τ). Using equation for the charge carrier mobility $\mu = e\tau/m^*$ where $m^* = 0.6m_e$ is the effective electron mass [61], we obtain quantum mobility of $\mu = 3000\,\mathrm{cm}^2/Vs$.

In order to investigate these oscillations we use Fourier transformation (FT) on the $\frac{\Delta G}{1/B}$ at finite gate voltages. The total charge carrier density can be calculated using eq. 2.12. We assume the Landau level degeneracy is $g_v g_s = 2$, and plot the resutls in the inset of fig. 4.2(b) in red circles. Moreover, we calculate charge carrier density using plate capacitor model as described in eq. 2.17, and plot the results in the inset of fig. 4.2(b) in blue squares. Seemingly, there is a discrepancy between the carrier density extracted from two calculations. Our tentative guess is that SdH oscillations from the two lower spin-split subbands are dominating the conductance. Nevertheless the charge carrier density increases linearly with increasing back gate voltage.

We calculated the mean free path using:

$$l_{\mathrm{mfp}} = \frac{\hbar\mu}{e}\sqrt{(2\pi n)}. \tag{4.1}$$

Using eq. 4.1 results in mean free path of ∼160 nm at highest charge density. This indicates a high quality semiconductor, which is promising for making

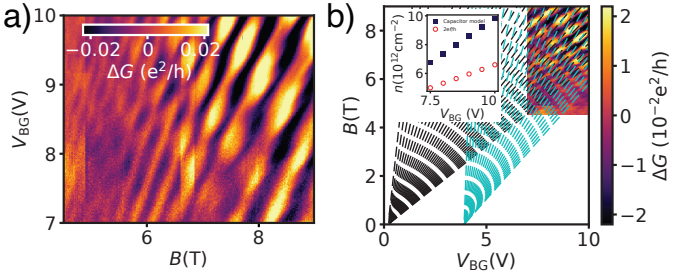

Figure 4.2. a) Change in amplitude of differential conductance ΔG in contacts C_1-C_2 as a function of back gate voltage, and perpendicular magnetic field. b) Demonstration of Landau fans superimposed on the same measurements as in (a). Inset is the charge carrier density as a function of back gate voltage; blue is calculated using plate capacitor model, and red is calculated using Fourier transformation analysis and $n = 2e/hf_{\mathrm{SdH}}$.

quantum devices.

In conclusion, we successfully established VIA contacts of normal metal, to MoS_2, and obtained low contact resistance, high mobility μ= 3000 cm^2/Vs, and relatively high mean free path l_{mfp} ∼160 nm.

4.3. Van der Waals contact

In this section, we discuss the bias spectroscopy, weak localization, and magneto transport measurements of a monolayer molybdenum disulphide, contacted with graphene:$NbSe_2$ that is shown in fig. 3.10(d). The superconducting energy gap associated to the bulk $NbSe_2$ is reported to be Δ_{NbSe_2}= 1.1 meV in the reference [93]. The resistance measurement of the $NbSe_2$ between C_1-C_2 as a function magnetic field gives the upper critical field of ∼1 T, as shown in the inset of fig. 4.3(a). This value is smaller than the reported values in the literatures that is 4 T for the bulk $NbSe_2$ H_{c2} [8, 94, 95], and can indicated a partial degradation of bulk $NbSe_2$ in our device.

We investigate the differential conductance of contacts C_2C_3 with respect to bias voltage (see fig. 4.3(a)). The dip in conductance at small bias voltage occurs at around $\mid V_{SD} \mid$<0.5 mV, which is well below the superconducting gap of NbS_2. This dip in conductance sustains up to B= 8 T, well above critical field of NbS_2. Therefore, our intuitive guess is that the dip in conductance is not associated to the superconducting energy gap, and rather an environmental Coulomb blockade.

Figure 4.3(b) shows bias spectroscopy of this device at various temperatures up to 4 K. The main characteristics vanishes completely at T= 4 K, an it does not match the upper critical temperature of bulk $NbSe_2$ T_C = 7 K [8]. This further confirms that we do not observe any superconducting effect in this set of measurements.

Figure 4.3(c) shows the change in conductance $\Delta G = G(B) - G(B = 0)$ of contact pair C_2-C_3 as a function of magnetic field, at various top gate voltages. At small magnetic fields there is a dip in ΔG. We tentatively attribute this to weak localization effect in MoS_2 [96]. The amplitude of dip in conductance increases by increasing the charge carrier density, as previously demonstrated by ref. [96].

The weak localization correction to the conductance can be experimentally studied by introducing external magnetic field. As a consequence of the magnetic field the time reversal symmetry is lifted and the quantum correction gets smaller and disappears at higher magnetic fields. The correction to the Drude conductance as a function of external magnetic field can be written as [26]:

$$\delta\sigma(B) - \delta\sigma(0) = \frac{e^2}{2\pi^2\hbar}[\Psi(\frac{1}{2} + \frac{\tau_B}{2\tau_\phi}) - \Psi(\frac{1}{2} + \frac{\tau_B}{2\tau_e}) + \ln(\frac{\tau_\phi}{\tau_e})]. \qquad (4.2)$$

Here, τ_ϕ is the phase coherence time, τ_e is the elastic scattering time, $\tau_B = \hbar/(2eDB)$, D is the diffusion constant, and $\Psi(x)$ is the digamma function.

The larger dip at higher charge carrier density could be attributed to the increase in coherent length increases at higher charge carrier density. Al-

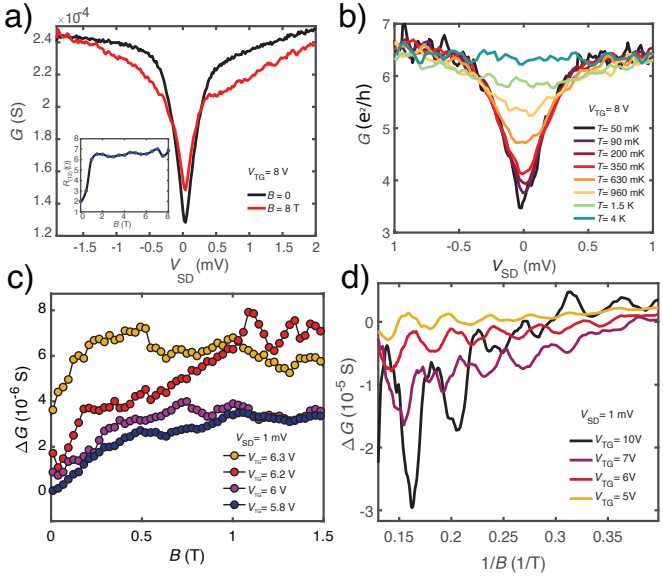

Figure 4.3. a) two-terminal differential conductance (C_2-C_3) with respect to the bias voltage and finite external magnetic field. Inset: Resistance of $NbSe_2$ between C_1-C_2 as a function of external magnetic field. b) Two-terminal differential conductance (C_2-C_3) with respect to the bias voltage, and various indicated temperature. c) Change in conductance ΔG of C_2-C_3 as a function of external magnetic field, at various indicated top gate voltage. The data are offset for clarity. d) Shubnikov-de Haas oscillations as a function of inverse magnetic field, at various indicated top gate voltage. A linear background is subtracted from the conductance amplitude.

though a fit to the data could reveal the estimated value for phase coherence time, this data is not of a high quality to be used for such analysis.

Figure 4.3(d) shows change in conductance amplitude ΔG as a function of inverse magnetic field, and at various indicated gate voltages. A linear background is subtracted from these data accounting for the classical hall effect. We attribute these oscillations occuring at $B_{\text{on.}} > 2.5\,\text{T}$ to Shubnikov-de Haas oscillations. Using onset of SdH oscillations, we obtain an outstanding value for the quantum mobility of $\mu_{\text{q}} = 4000\,\text{cm}^2/Vs$. The mean free path is $l_{\text{mfp}} = 190\,\text{nm}$, the largest we have ever recorded in our measurements.

In conclusions, we successfully established VdW contacts of supercon-

ducting two-dimensional material to two-dimensional semiconductor, and obtained low contact resistance, high mobility $\mu = 4000\,\mathrm{cm}^2/\mathrm{Vs}$, and large mean free path $l_{\mathrm{mfp}} = 190\,\mathrm{nm}$. Nevertheless, we did not observe any signature of superconducting proximity effect in our measurements.

4.4. MoRe:Pt bottom contact

In this section, we provide with additional measurements of a monolayer molybdenum disulphide device with MoRe:pt VIA contacts, shown previously in fig. 3.5(a). We restrict ourselves to investigate the superconducting effects in the measurements. All the measurements are carried out in a VTI with T_{base}= 1.7 K.

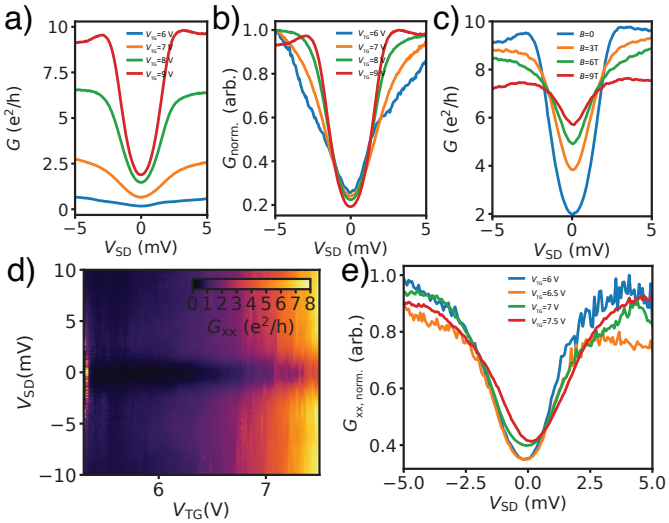

Figure 4.4. c) Two-terminal differential conductance measured between contacts C_1-C_4 as a function of bias voltage, and at various indicated top gate voltage. b) Same data as in (a) with normalizing conductance values $G_{\text{norm.}}$=$G(V_{\text{SD}})/max(G(V_{\text{SD}}))$. c) Two-terminal differential conductance between contacts C_1-C_4 as a function of bias voltage, and indicated external magnetic fields. d) Four-terminal differential conductance ($G_{\text{xx}} = \mathrm{d}I_{14}/\mathrm{d}V_{23}$) as a function of bias voltage and top gate voltage. e) Four-terminal deferential conductance (normalized to maximum G_{xx}) as a function of bias voltage at various indicated top gate voltages.

Figure 4.4(a) shows two-terminal differential conductance measurements of C_1-C_2 (edge to edge distance ∼200 nm) as a function of bias voltage, at various specified top gate. A suppression of conductance at low bias voltage $|\ V_{\text{SD}}\ |$<2.5 mV is visible for all gate voltages. In order to study the characteristics of these measurements, we normalize these curves with respect to their respective maximum $G_{\text{norm.}}$= $G(V_{\text{SD}})/max(G(V_{\text{SD}}))$. Seemingly,

the suppression of conductance is more pronounced at high gate voltages (see fig. 4.4(b)). We also investigate the effect of perpendicular external magnetic field on the characteristics of the bias spectroscopy. Figure 4.4(c) shows differential conductance as a function of bias voltage, at fixed top gate voltage V_{TG}= 9 V, and finite external magnetic field B= 0-9 T. At high magnetic fields, the overall suppression reduces significantly and the U shape characteristics changes to a V shape.

We tentatively attribute the dip in conductance to the superconducting energy gap of bulk MoRe $2\Delta_{\mathrm{MoRe}}$=2.5 eV, where the density of states of the quasiparticles within the gap $\mid V_{\mathrm{SD}} \mid < 2\Delta_{\mathrm{MoRe}}$ is suppressed. The bias spectroscopy in perpendicular magnetic field further approves this speculation, since the superconductivity is suppressed at higher external magnetic field (see fig. 4.4(c)).

Besides two-terminal measurements, we carried out four-terminal measurements, to reduce the effect of contact resistance. As shown in fig. 4.4(d), a signature of superconducting energy gap is present over a long range of top gate voltage. Similar to the aforementioned measurements, the bias voltage at which the suppression occurs is $\sim$ 2.6 mV.

In conclusion, we establish low resistance MoRe:Pt bottom contacts to monolayer molybdenum disulphide. More importantly, we observe a signature of superconducting gap $\mid V_{\mathrm{SD}} \mid < 2.5$ mV, with no gate voltage dependence. Intuitively, we attribute the apparent gap to the MoRe bulk superconducting energy gap. Furthermore, we observe a suppression in this gap at higher magnetic fields.

4.5. Conclusions

Throughout this chapter, we have discussed various characteristics of different electronic devices. We summarize our findings in table 4.5. These results are selected from the measurements of different devices. Based on the mobility and mean free path, the intrinsic quality of monolayer molybdenum disulphide is preserved, regardless of the fabrication type.

The VdW-contact is very promising in case of high mobility, and low contact resistance. Despite, we have not observed any signature of superconducting contacts in our measurements.

One of the most promising technique is bottom contact fabrication, where we observed signature of superconducting density of state. This fabrication technique is limited by the oxidation of contact material. Unfortunately, our intense efforts to thin down the Pt layer (i.e. capping layer) and reduce the inverse proximity effect was not successful, Probably due to the oxidation of the contact material. Therefore, in search of superconducting proximity effect we move on to another contact fabrication technique, that will be the topic of chapter 5 of this manuscript

Type	Material	R_2t (kΩ) (LT)	RA (kΩ.µm2)	Mobility (cm2/VS)	mean free path
VIA	Au	180	144	3000	155
VIA	MoRe	200	28	2500	130
VIA	MoRe	430	54	3000	160
B.C.	MoRe-Pt	4	13.6	100*	-
B.C.	Au(Ti-Au)	60	600	1700*	90
VdW	NBSe2	2.7	200	4000	190

Figure 4.5. A general overview of the characteristics of successful fabrication method. The reported mobility amplitude corresponds to quantum mobility. Except for those marked with '*': that corresponds to Drude mobility.

5 Superconducting contacts to a monolayer semiconductor[1]

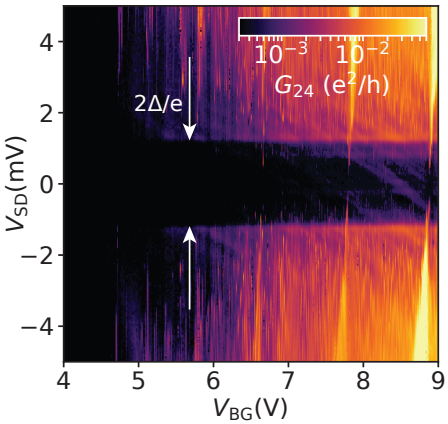

In this chapter we demonstrate superconducting vertical interconnect access (VIA) contacts to a monolayer of molybdenum disulfide (MoS_2), a layered semiconductor with highly relevant electronic and optical properties. As a contact material we use MoRe, a superconductor with a high critical magnetic field and high critical temperature. The electron transport is mostly dominated by a single superconductor/normal conductor junction with a clear superconductor gap. In addition, we find MoS_2 regions that are strongly coupled to the superconductor, resulting in resonant Andreev tunneling and junction dependent gap characteristics, suggesting a superconducting proximity effect. Magnetoresistance measurements show that the bandstructure and the high intrinsic carrier mobility remain intact in the bulk of the MoS_2. This type of VIA contact is applicable to a large variety of layered materials and superconducting contacts, opening up a path to monolayer semiconductors as a platform for superconducting hybrid devices.

[1] Parts of this chapter were published in a similar form in Ref.[97]

5.1. Introduction

Semiconductors combined with superconducting metals have become a most fruitful field for applications and fundamental research, from gate tunable superconducting qubits [98], thermoelectrics [99, 100], to prospective Majorana bound states, [21, 101] or sources of entangled electron pairs [18, 102, 103]. These experiments were mainly developed based on one-dimensional (1D) nanowires. To obtain more flexible platforms and scalable architectures, recent efforts focused on two-dimensional (2D) semiconductors [104–107]. However, the number of materials suitable for superconducting hybrids is rather limited. Potentially ideal and ultimately thin semiconductors with a large variety of properties can be found among transition metal dichalcogenides (TMDCs) grown in stacked atomically thin layers. TMDCs often exhibit a broad variety of interesting optical and electronic properties [54, 108, 109], for example the valley degree of freedom, potentially useful as qubits [11, 110], strong electron-electron [59, 111] and spin-orbit interactions [59], or crystals with topologically non-trivial band-structures [112, 113]. One promising material is the semiconductor MoS_2, with a relatively high mobility and large mean free path, allowing for gate-defined nanostructures [61, 114, 115], which would make MoS_2 an ideal platform to combine with superconducting elements.

MoS_2 was used as tunnel barrier between superconductors in vertical heterostructures [116, 117] and showed signs of intrinsic superconductivity [118] and of a ferromagnetic phase at low electron densities [119]. However, to exploit the intrinsic properties of MoS_2 and to fabricate in-situ gate tunable superconducting hybrid structures, direct superconducting contacts in lateral devices are required. Such contacts are difficult to fabricate due to the formation of Schottky barriers [76, 112, 120], material degradation [121] and fabrication residues when using standard fabrication methods [114, 122, 123]. Less conventional edge contacts were also found problematic recently [124].

Here, we report vertical access interconnect (VIA) contacts [75] to monolayer MoS_2 with the superconductor MoRe as contact material. We demonstrate a clear superconducting gap in the transport characteristics, including the magnetic field and temperature dependence, and features suggesting stronger superconductor-semiconductor couplings, forming the basis for superconducting proximity effects and bound states. In addition, we show that this fabrication method retains the intrinsic MoS_2 bulk properties, including a large electron mobility and sequentially occupied spin-orbit split bands [61].

5.2. Results and discussion

Figure 5.1(a) shows an optical microscopy image of the presented device, and a schematic of a single VIA contact. The MoS_2 is fully encapsulated by exfoliated hexagonal boron nitride (hBN), ensuring minimal contamination of the bulk materials, while the following assembly process allows the fabrication of pristine material interfaces and contacts, for example never directly exposing the active contact area to air:

1) vertical access: using electron beam lithography (EBL), VIA areas with a radius of 200 nm are defined on the designated top hBN flake (~ 40 nm thickness) on a Si/SiO_2 wafer, and etched completely open by reactive ion etching with a 20:5:5 sccm SF_6:O_2:Ar mixture at 25 mTorr chamber pressure and 50 W RF power.
2) VIA metalization: in a second EBL step, a slightly larger area with the VIA in the center is defined for mechanical anchoring to the top hBN. We then deposit the type II superconductor MoRe (bulk critical temperature $T_c \approx 6-10$ K, (second) critical magnetic field $B_c \approx 8-9$ T [125, 126]) using sputter techniques. As the optimal film thickness we find 10 nm plus the top hBN thickness.
3) Stacking of layers: the wafer with the VIA structure is transferred to an inert gas (nitrogen) glove box (residual water and oxygen levels: < 0.1 ppm), where the top hBN layer with the metalized VIAs is picked up from the substrate using a polycarbonate (PC) stamp and an hBN helper layer, and then used to pick up consecutively a monolayer MoS_2 flake, a bottom hBN flake (~ 25 nm thickness), and a multilayer graphene (MLG) flake serving as backgate.
4) Finish: the stack is then deposited onto a Si/SiO_2 wafer, where macroscopic Ti/Au (10/50 nm) leads to the VIAs are fabricated using EBL. The sample is then annealed at 350°C for 30 min, in a vacuum chamber with a constant flow of forming gas.

Using gold as VIA material, this fabrication process yields $> 80\%$ of the contacts with two-terminal resistance-area products smaller than $200\,\mathrm{k\Omega\mu m^2}$ at $T = 1.7$K at a backgate voltage of $V_{BG} = 10$ V. This yield is reduced to $\sim 65\%$ when using MoRe, possibly due to a material loss during the pick-up procedure. In the presented device, only half of the contacts show resistances lower than $200\,\mathrm{k\Omega\mu m^2}$, which we use for the experiments and are labeled from C_1 to C_4 in fig. 5.1(a). The contacts were fabricated at various distances, stated individually for each discussed contact pair, all in the range of a few micrometers. The two terminal differential conductances $G_{jk} = dI_j/dV_k$ we obtain by measuring the current variation in the grounded contact C_j while applying a modulated bias voltage V_{SD} to con-

tact C_k using standard lock-in techniques. The experiments were performed in a dilution refrigerator at $\sim 60\,\mathrm{mK}$, while for higher temperatures, we used a variable temperature insert (VTI) with a base temperature of $\sim 1.7\,\mathrm{K}$. In addition, we apply an external magnetic field B perpendicular to the substrate.

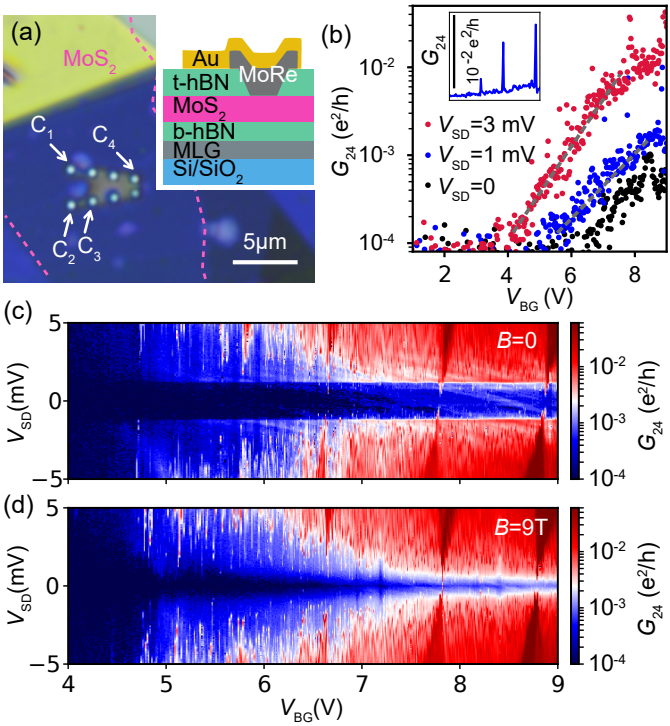

Figure 5.1. (a) Optical microscopy image of the MoS_2 heterostructure, with MoRe VIA contacts pointed out by white arrows. Inset: schematic of a VIA contact, with t-hBN and b-hBN denoting the top and bottom hBN layers, respectively. (b) Differential conductance G_{24} as a function of V_{BG} for a series of V_{SD} on a logarithmic scale, and as an inset for $V_{SD} = 1\,\mathrm{mV}$ on a linear scale. (c) G_{24} vs. V_{BG} and V_{SD} at $B = 0$ and (d) at $B = 9\,\mathrm{T}$.

In fig. 5.1(b), the differential conductance G_{24} (center to center contact distance: $4.85\,\mu\mathrm{m}$) is plotted as a function of the backgate voltage V_{BG} for several bias voltages V_{SD}. Increasing V_{BG} results in an exponential increase in G_{24}, starting from a pinch-off voltage of $V_{BG} \approx 6\,\mathrm{V}$ for $V_{SD} = 0$.

This value is offset towards smaller values for larger bias voltages, a first indication for an energy gap. However, as seen in the inset of fig. 5.1(b), in this regime we find very sharp peaks in G, consistent with Coulomb blockade (CB) effects. We note that an increase in V_{BG} not only changes the charge carrier density in the MoS_2, but also the Schottky barrier at the metal-semiconductor interface and disorder induced charge islands. To demonstrate a superconducting energy gap and to distinguish it from other effects like CB, we plot in fig. 5.1(c) the conductance G_{24} vs. V_{SD} over a large range of V_{BG} at $B = 0$, while fig. 5.1(d) shows the same experiment at $B = 9\,\mathrm{T}$. At $B = 0$, independent of the gate voltage, one clearly finds a strongly suppressed conductance for roughly $|V_{\mathrm{SD}}| < 1.2\,\mathrm{mV}$, a gap size consistent with literature values for the superconducting energy gap of MoRe [127]. Similar data for a second device are shown in the supplementary material, fig. S1. The conductance is suppressed by a factor ~ 8 between the large and the zero bias values at $V_{\mathrm{BG}} \approx 6\,\mathrm{V}$, and by a factor of ~ 15 near $V_{\mathrm{BG}} = 8\,\mathrm{V}$. We note that such a sharp gap is only observable if a tunnel barrier is formed between the semiconducting MoS_2 and the superconducting region, at least at one contact. The discrete features inside the gap are probably not Andreev bound states [128, 129], but rather originate from gate-modulated conductance features in the bulk MoS_2. At $|V_{\mathrm{SD}}| > 1.2\,\mathrm{mV}$, we find a strong modulation of G, which we interpret as several Coulomb blockaded regions. These resonances suggest that there is significant disorder near some of these contacts, so that we can think of this device as an MoS_2 region, incoherently coupled to the contacts by two normal-superconductor (N-S) junctions. The reason for one junction, namely the less transparent one, dominating the transport characteristics is that the junction with the higher transmission has a reduced resistance in the energy gap due to Andreev reflection, in which two electrons are transferred to S to form a Cooper pair. At $B = 9\,\mathrm{T}$, the superconducting gap is reduced, as discussed below in detail, but we now find that the gap becomes gate dependent. While in short semiconducting nanowires a gate tunable proximity effect was reported [49, 130], we tentatively attribute our finding to a gate independent superconducting energy gap convoluted with a gate tunable MoS_2 conductance.

We investigate the gap in the transport characteristics and the field dependence in more detail in fig. 5.2 for the same contact pair. Similar data we find for the other contact pairs and on two more devices, with an additional example provided in the supplementary data, see fig. S1. Figures 5.2(a)-(c) show higher resolution conductance maps for a smaller V_{BG} interval, for the magnetic fields $B = 0$, $B = 5\,\mathrm{T}$ and $B = 9\,\mathrm{T}$, respectively. The figures show a very clear gap in the conductance map, which is systematically reduced with increasing magnetic field, independently of the sharp resonances. The positions of the latter are unaffected by the gap, so that we can attribute

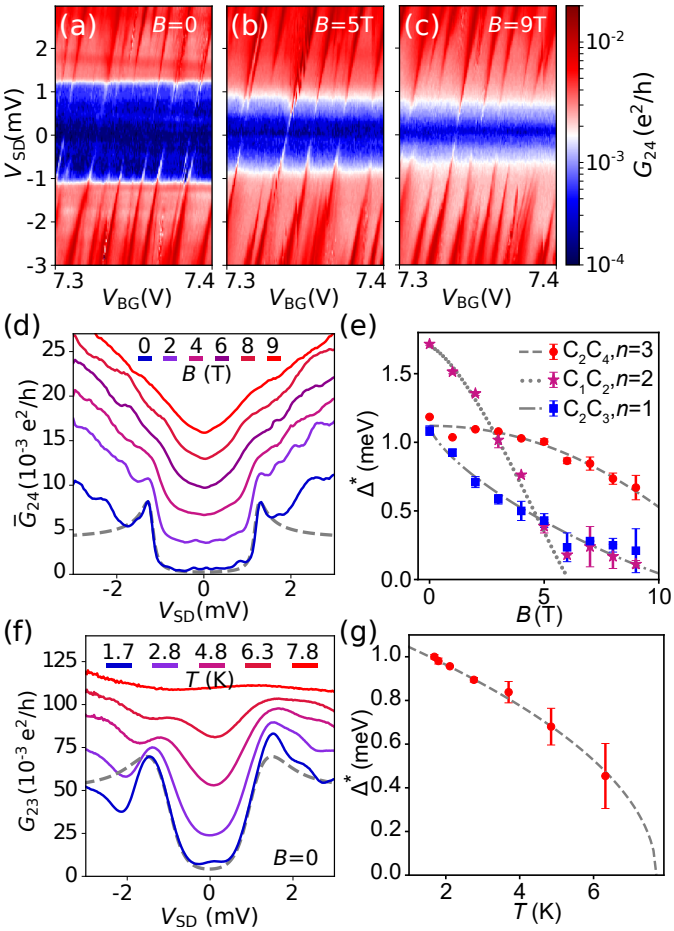

Figure 5.2. (a) Differential conductance G_{24} as a function of the bias V_{SD} and the backgate voltage V_{BG} at $B = 0$, (b) $B = 5\,\mathrm{T}$, and (c) $B = 9\,\mathrm{T}$. (d) G_{24} averaged over a V_{BG} interval of 0.5 V plotted vs. V_{SD} for the indicated magnetic fields, with the curves offset for clarity. (e) Superconducting energy gap Δ^* as a function of B for different contact pairs. Δ^* is extracted from the inflection points in the curves of fig. 2(d) [red disks], from fig. 3 [purple stars] and from an additional data set discussed in the supplemental data, fig. S2 [blue rectangles]. (f) G_{23} vs. V_{SD} recorded at the indicated temperatures T. (g) Δ^* vs. T extracted from the data in (f). All theoretical curves (dashed and dotted lines) are discussed in the text.

them to resonances in the MoS_2, for example due to CB. To extract the energy gap, we plot G_{24} in fig. 5.2(d), averaged over a gate voltage interval of 0.5 V for each V_{SD} value, for a series of perpendicular magnetic fields. These curves show how the energy gap closes with increasing B. The curve at $B = 0$ can be fitted well using the model by Blonder, Tinkham and Klapwjik (BTK) [39], including an additional broadening parameter [131], as shown in fig. 5.2(d) by a gray dashed line. The fit parameters are consistent with a weakly transmitting barrier in a single N-S junction. At larger fields, the extracted parameters become ambiguous due to a strong broadening of the curves. As a measure for the superconducting energy gap Δ^*, we therefore plot in fig. 5.2(e) the average of the low-bias inflection points of each curve (red dots). For $B = 0$, we find $\Delta_0^* \approx 1.2$ meV, in good agreement with bulk MoRe [116, 127] and one S/N junction dominating the transport. The field dependence of Δ^* is well described by standard theory of superconductivity for pair breaking impurities in a metal with a mean free path shorter than the superconducting coherence lengths. For the corresponding self-consistency equations we use $\Delta^*(\alpha) = \hat{\Delta}(\alpha)[1 - (\alpha/\hat{\Delta}(\alpha))^{2/3}]^{3/2}$, with $\Delta^*(\alpha)$ the energy gap in the excitation spectrum and $\hat{\Delta}$ the order parameter determined numerically from $\ln(\hat{\Delta}(\alpha)/\Delta_0) = -\pi\alpha/4\hat{\Delta}(\alpha)$ for a given pair breaking parameter α [132, 133]. The latter we interpolate as $\alpha = 0.5\Delta_0^*(B/B_c)^n$, with n a characteristic exponent. As shown in fig. 5.2(e), the best fit we obtain for $n = 3$, $\Delta_0^* = 1.12$ meV and the (upper) critical field $B_c = 14.5$ T. The latter value is clearly larger than reported for bulk MoRe. Seemingly similar data plotted as purple stars and blue rectangles we discuss below.

As expected for a superconducting energy gap, Δ^* is also reduced with increasing temperature T. In fig. 5.2(f) we plot G_{23} (contact distance: $\sim 1.55\mu$ m) as a function of V_{SD} at $V_{BG} = 9$ V for a series of temperatures at $B = 0$ in a different cooldown. For the lowest values of T, we can reproduce the data using very similar BTK and Dynes parameters as above, only adjusting the normal state resistance and the temperature to $T = 1.7$ K. However, at higher temperatures, the fits become ambiguous, due to a broadening and possibly a temperature dependence of the Schottky barrier [76]. Again, we plot the inflection points of the curves as an estimate for Δ^*, as shown in fig. 5.2(g). To determine the critical temperature, we fit the expression $\Delta^* = \Delta_0^*\sqrt{1 - T/T_c}$ and find $T_c = 7.7$ K and $\Delta^* = 1.2$ meV, consistent with literature values for bulk MoRe [126, 127]. Up to this point, our experiments demonstrate superconducting contacts, but with a weak electronic coupling between the MoS_2 and the reservoirs, at least for one contact junction. However, we also find evidence for a stronger coupling of MoS_2 regions to the superconductors, relevant for devices relying on the superconducting proximity effect. As an example, we show bias

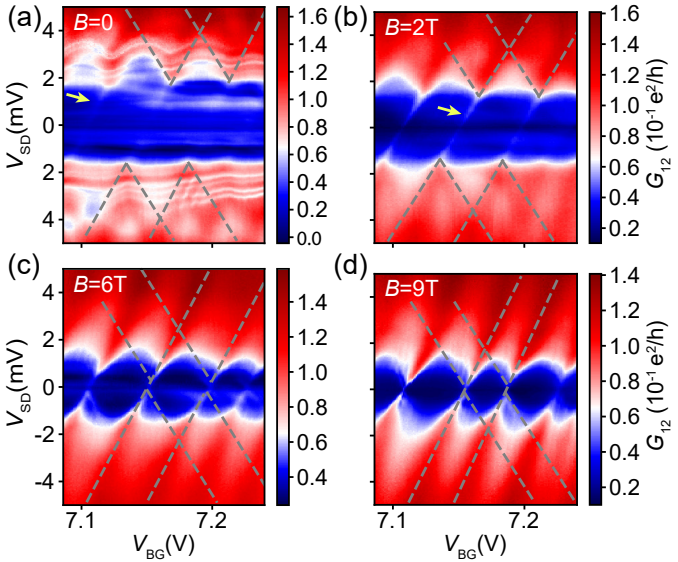

Figure 5.3. G_{12} plotted as a function of V_{BG} and V_{SD} at (a) $B = 0$, (b) $B = 2\,\mathrm{T}$, (c) $B = 6\,\mathrm{T}$ and (d) $B = 9\,\mathrm{T}$, recorded at $T = 60\,\mathrm{mK}$. The dashed lines trace the CB diamonds, shifted vertically and horizontally between the subfigures, while the yellow arrows point out lines of resonant Andreev tunneling.

spectroscopy measurements with CB features between contacts C_1 and C_2 (distance $\sim 2.5\,\mu\mathrm{m}$) in fig. 5.3, for a series of magnetic fields B. Similarly as in fig. 2, we find a transport gap, reduced by larger B values. Here, the low-bias ends of the CB diamonds are shifted in energy and in gate voltage, as indicated by the gray dashed lines, consistent with a MoS_2 quantum dot (QD) directly coupled to one superconducting contact (i.e. forming an S-QD-N junction) [19]. These tips of the CB diamonds are connected across the gap by a single faint resonance, pointed out by yellow arrows, best seen in fig. 3(b) at $B = 2\,\mathrm{T}$. We attribute these lines to resonant Andreev tunneling [19], in which the electrons of a Cooper pair pass through the QD in a higher order tunneling process. This process is suppressed much stronger by a tunnel barrier than single particle tunneling [134], which suggests that the QD is strongly coupled to the superconductor. At large B fields, a quasi-particle background in the superconducting density of states results in single particle CB diamonds [49]. With a QD charging energy of

$\sim 2\,\mathrm{meV}$ and using $E_\mathrm{c} = \frac{e^2}{8\epsilon\epsilon_0 r}$ for a disc shaped QD encapsulated in hBN, we estimate the radius of the confined QD region as $r \approx 300\,\mathrm{nm}$.

The shift of the CB diamonds in V_SD gives a measure for Δ^* [19], which we read out at the bias at which $\sim 50\%$ of the large bias conductance is reached at the tip of the CB diamond. The extracted values are plotted as purple stars in fig. 2(e). Surprisingly, we find a significantly larger zero field gap, $\Delta_0^* \approx 1.7\,\mathrm{meV}$, and a rather different functional dependence on B than for the curves analyzed in fig. 2 (red dots). The latter is demonstrated by the dotted line obtained for the exponent $n = 2$, and $B_\mathrm{c} = 6.4\,\mathrm{T}$. In addition, fig. 2(e) shows a third Δ^* curve extracted from CB diamond shifts in experiments on another contact pair shown in the supplemental data, fig. S2. For this curve, we obtain $n = 1$, while $\Delta^* \approx 1.12\,\mathrm{meV}$ and $B_\mathrm{c} \approx 12\,\mathrm{T}$ correspond well to the previously obtained values.

While a larger gap in the transport experiments can be simply attributed to a significant fraction of the bias developing across another part of the device, for example across the second N-S junction, the different functional dependence is more difficult to explain. Since nominally the geometry and MoRe film thickness are identical for all contacts, we tentatively attribute this finding to a superconducting proximity region forming in the MoS_2 near a strongly coupled contact, yielding an induced superconducting energy gap Δ^* [49], and a different B-field dependence of the pair breaking compared to the bulk superconductor.

Additional indications for a stronger coupling to S are the almost gate voltage independent features at $B = 0$, reminiscent of two NS junctions and multiple Andreev reflection processes in between, with a much stronger suppression with increasing B than for the observed gap. In the supplemental data, fig. S3(a), we also show data at higher gate voltages, exhibiting a conductance minimum instead of a maximum at the bias that corresponds to the energy gap, developing into negative differential conductance at the lowest field values. These findings are qualitatively consistent with calculations for an S/I/N/S junction with resonances in the N region [135].

The above data show that our fabrication scheme results in superconducting contacts to monolayer MoS_2, possibly with a reasonably strong coupling to the superconductors for some of the contacts. To demonstrate that the intrinsic properties of MoS_2 are intact in the bulk crystal, we investigate quantum transport in large magnetic fields and at bias voltages large enough to render the superconducting energy gap irrelevant. In fig. 5.4(a) we plot the dc conductance $G_{12} = I_1/V_\mathrm{SD}$ as a function of V_BG and B, at $V_\mathrm{SD} = 8$ mV and $T = 60$ mK, from which we have subtracted a third order polynomial background for each gate voltage to eliminate effects from the classical Hall effect and CB effects.

Figure 5.4(a) shows well developed Shubnikov de Haas (SdH) oscillations,

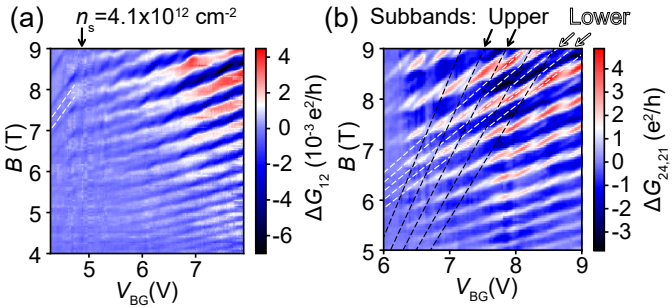

Figure 5.4. (a) Two-terminal dc conductance $G_{12} = I_1/V_{SD}$ with $V_{SD} = 8\,\text{mV}$ applied to contact C_2, plotted as a function of the magnetic field B and the backgate voltage V_{BG} at $T \approx 60\,\text{mK}$. n_s points out the gate voltage corresponding to the electron density at which the higher spin-orbit subbands start to be populated. (b) Three-terminal dc conductance $G_{24,21} = I_2/V_{12}$, with an external bias $V_{SD} = 10\,\text{mV}$ applied to C_4, while the current I_2 is measured at C_2 and the voltage difference V_{12} between C_1 and C_2. In both maps, a third order polynomial was subtracted at each gate voltage to remove a smooth background.

suggesting a high MoS_2 quality, with an onset at $B_{on} < 4\,\text{T}$. In the Drude model, this onset is interpreted as the charge carriers closing a cyclotron orbit before being scatted, which happens roughly at $\omega_c\tau > 1$, with $\omega_c = eB/m^*$ the cyclotron frequency, m^* the effective electron mass, and τ the scattering time. This yields a lower bound for the carrier mobility of $\mu = e\tau/m^* \approx 2500\,\text{cm}^2/\text{Vs}$, similar to $\mu \approx 5000\,\text{cm}^2/\text{Vs}$ we obtain with Au VIA contacts, identical to the best literature values [114]. The discrepancy in mobility between the MoRe and the Au VIA contacts we attribute to heating effects due to the much larger bias we apply to the MoRe contacts to avoid effects of the superconducting energy gap.

The quality of the MoS_2 can also be seen in the fact that the the four lowest spin-orbit subbands, corresponding to the valley and the spin degree of freedom, are not mixed by disorder. We find that the slope of the SdH resonances changes by roughly a factor of two at $V^*_{BG} = 4.8\,\text{V}$, corresponding to an electron density of $n_s \approx 4.1 \times 10^{12}\text{cm}^{-2}$, at which the two upper spin-orbit subbands become populated. Using $m^* = 0.6$, we obtain a subband spacing of $\sim 15\,\text{meV}$, as reported previously [61]. These features prevail also at $T \approx 1.7\,\text{K}$, as shown in the supplemental data, fig. S3(b).

The two-terminal magneto-conductance measurements suffer from large background resistances due to Shottky barriers, which we can partially cir-

cumnavigate by performing a three terminal experiment. In fig. 4(b) we plot the dc conductance $G_{24,21}$, as explained in the figure caption. This technique removes the contact resistance at C4, so that the conductance resonances due to the Landau levels can be measured more clearly. The results in fig. 4(b) show similar patterns as in better suited Hall bar experiments [61], exhibiting clear superposition patterns of the spin and valley split subbands, indicated by dashed lines. We note that due to the less ideal contact geometry of our devices, we cannot go to lower electron densities in these experiments, because the current density passing near the remote contacts is very low.

5.3. Conclusions

In conclusion, we established superconducting contacts to a monolayer of the TMDC semiconductor MoS_2 using vertical interconnect access (VIA) contacts, and characterized the superconducting energy gap in different transport regimes. The fact that in most experiments one N-S junction dominates the transport characteristics, and signatures of resonant Andreev tunneling and a superconducting proximity effect, suggest that also contacts with a stronger transmission between the superconductor and the semiconductor are possible, thus opening a path towards semiconductor-superconductor hybrid devices at the limit of miniaturization, with a group of materials - the TMDCs - that offers a very large variety of material properties and physical phenomena.

5.A. Supporting informations

The supplemental data mentioned in the text as Figs. S1, S2 and S3 are available free of charge on the ACS Publications website at DOI:
with the following content: gate and magnetic field dependence obtained on a second device, Coulomb blockade diamond analysis obtained for a second contact pair (C_2 and C_3), bias spectroscopy data for G_{12} at the larger backgate voltage $V_{\mathrm{BG}} = 9.0\,\mathrm{V}$, and Shubnikov de Haas oscillations (Landau fan) at a temperature of $\sim 1.7\,\mathrm{K}$.

All data in this publication are available in numerical form at Link here.

5.A.1. Further measurements of the main device

Figure 5.8 shows the two-terminal differential conductance G_{23} between contacts C_2 and C_3 as a function of the gate voltage V_{BG} and the bias voltage V_{SD} for a series of magnetic fields. These maps (and several more at different B values) were used to extract the energy gap Δ^* plotted as blue rectangles in fig. 2(e) of the main text. In fig. 5.6(a) we show the bias

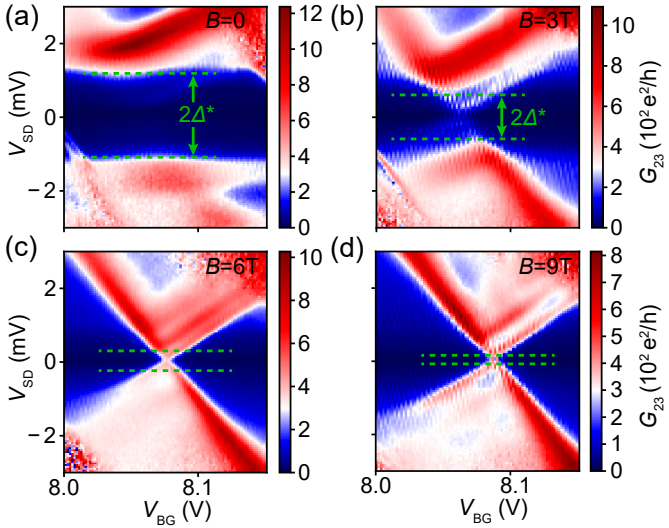

Figure 5.5. (a) G_{23} as a function of V_{SD} and V_{BG} for a series of external magnetic field values B, applied perpendicular to the substrate plane at $T = 60\,\text{mK}$.

dependence of the differential conductance G_{12} at $V_{BG} = 9\,\text{V}$. Around this gate voltage, the MoS_2 conductance is almost independent of V_{BG}. However, we find a strong modulation of G_{12} with bias, with a conductance minimum at a value where one might expect a maximum due to the BCS coherence peaks in the superconductor density of states. A second minimum occurs at twice the value. The first minimum even turns negative at zero B, showing negative differential conductance. These features are independent of gate voltage and suppressed with increasing magnetic field, on the same scale as the gap in the main text.

These data are at least qualitatively consistent with model calculations [135] for the case of an S/I/N/S junction with a weak to intermediate coupling between S and I, and with resonances occurring in the N-region. Taking the average of the first minima at negative and positive bias as an estimate, we find $\Delta^* \approx 1.3\,\mathrm{meV}$, as indicated in the figure. These findings again demonstrate that MoS_2 forms an electrical connection to the superconducting VIA contacts, possibly with a Shottky barrier near one of the contacts.

In fig. 5.6(b) we show additional Shubnikov de Haas (SdH) oscillations in the differential conductance, similar to fig. 4 in the main text, but at a temperature of 1.7 K. At these temperatures, the individual spin-orbit subband SdH oscillations are more washed out, but the transition from two to four subbands being occupied is more clearly visible at the indicated $n_s = 4.1 \cdot 10^{-12}\,\mathrm{cm}^2/(\mathrm{Vs})$. We would like to note that from the data illustrated in

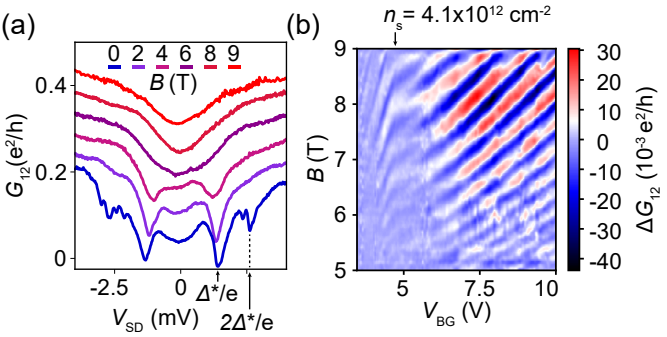

Figure 5.6. (a) Two terminal differential conductance G_{12} as a function of the bias voltage V_{SD} at the backgate voltage $V_{BG} = 9\,\mathrm{V}$ and at a temperature of $T \approx 60\,\mathrm{mK}$. (b) G_{12} at $V_{SD} = 7\,\mathrm{meV}$, plotted as a function of V_{BG} and the magnetic field B applied perpendicular to the substrate plane, at $T \approx 1.7\,\mathrm{K}$.

fig. 5.6(b) a third order polynomial background was subtracted at each gate voltage to remove a smooth background. The background is attributed to the transverse component of Hall resistivity.

5.A.2. Measurements of a second device

Figure 5.7 shows additional data obtained from a second device fabricated as described in the main text and investigated by transport spectroscopy at a temperature of $\sim 250\,\mathrm{mK}$ in a Helium 3 cryostat. This data set reproduces

the findings in the main text. For example, we also find a superconducting transport gap that is reduced with increasing magnetic field, but is essentially independent of the backgate voltage. This device featured four contacts with a diameter of 300 nm, of which three had useful contact resistances as defined in the main text. The center-to-center distance between the two contacts used to obtain the presented data is 1.7 μm. We point out that in these measurements, we find strong Fabry-Perot type oscillations and no significant Coulomb blockade diamonds at gate voltages larger than 3 V.

Figure 5.8 shows the result of our model indicating the change in conductance of MoS_2 in presence of an external magnetic field and at different gate voltages. Two sets of Landau levels originates from two different subbands, as discussed in the main text.

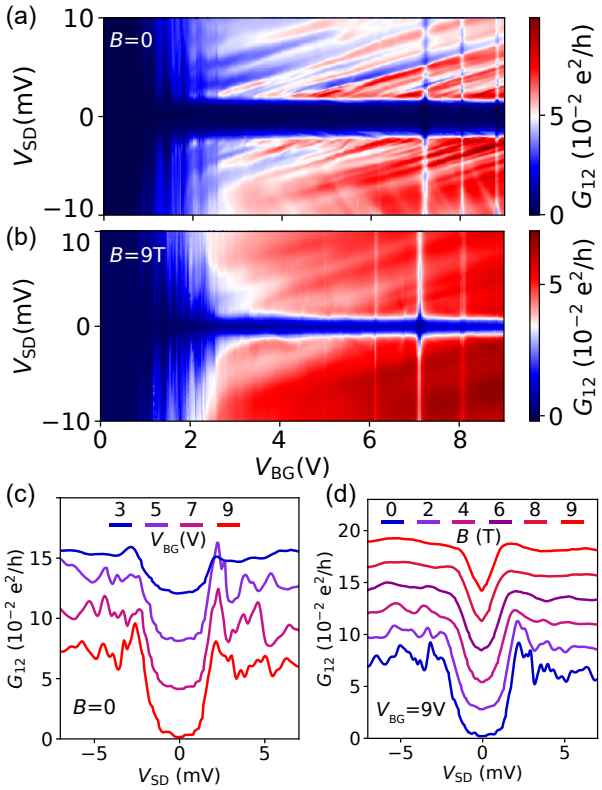

Figure 5.7. Data for a second device. (a) and (b) Two terminal differential conductance G_{12} as a function of the bias voltage V_{SD} and the backgate voltage V_{BG}, recorded at the magnetic fields $B = 0$ and $B = 9\,\mathrm{T}$, respectively. (c) shows cross sections of the data in (a) at the indicated constant backgate voltages. (d) G_{12} as a function of V_{SD} at $V_{\mathrm{BG}} = 9.0\,\mathrm{V}$ for a series of magnetic fields. In (c) and (d) the curves are offset by a constant for clarity.

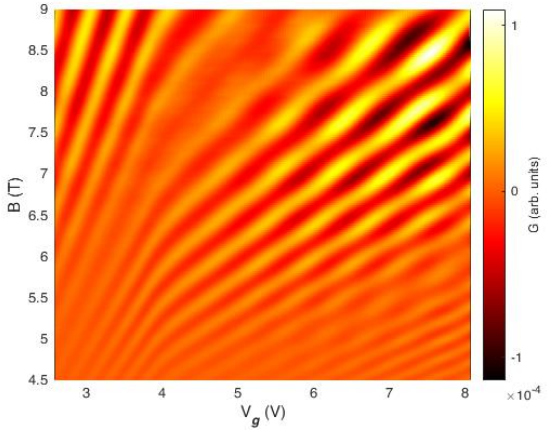

Figure 5.8. Model showing the change in conductance of an MoS_2 device as a function of magnetic field and gate voltage.

6 Coherent transport and 2D Andreev bound states in a monolayer semiconductor[1]

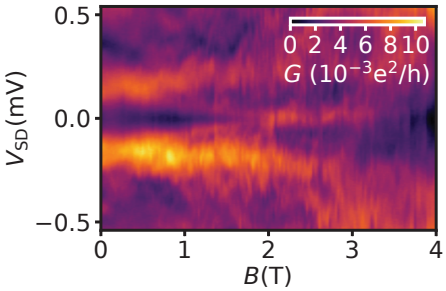

In this chapter, we discuss our experimental findings of a monolayer MoS_2 device with high quality MoRe contacts. The superconducting VIA's are fabricated as close as $\sim$ 300 nm edge to edge distance of each other. The modification of the fabrication method increased the yield to 100% working contacts, and all contacts have similar characteristics. We investigate the superconducting gap at $V_{SD} \sim 2\Delta_{MoRe}/e = 2.4$ mV, and a subgap feature at V_{SD}=170 μV. Furthermore, we demonstrate a zero-bias conductance peak at finite magnetic field B=2-3 T, and investigate the effect of magnetic field on these characteristics. Finally, we provide our interpretation of these findings.

[1] In preparation

6.1. Materials and methods

In chapter 5, we investigate the first superconducting MoRe VIA contacts to monolayer MoS_2. In order to improve the device quality, we decrease the edge to edge distance of the VIA contacts and increase the fabrication yield. For that, we first adjust the dose test for achieving a larger undercut and consequently reduce the side deposition (bi-product of the sputtering process) (see supporting information fig. 6.5(a,b)). Then, we utilize an AFM cleaning step after the deposition of MoRe, to remove the reminiscence of the side deposition, and any residual polymer on the surface (see supporting informations fig. 6.5(c,d)). By doing so, we increase the yield of working contacts to 100% measured at low temperatures.

Figure 6.1(a) shows a monolayer MoS_2 (indicated by black dashed line) equipped with MoRe VIA contacts (indicated by the red circles), and Ti:Au leads. All four superconducting contacts demonstrate similar characteristics at low temperatures. The measurements are carried out in a dilution refrigerator with a base temperature of T_{base}= 50 mK. We restrict ourselves to two terminal measurements of contact pair C_1-C_2, where the edge to edge distance of these contacts is ∼300 nm. Since all of the contacts are superconducting, and often far apart, multi terminal measurement is difficult, due to a low current density below the contacts in this geometry. Further measurements of other contact pairs are mentioned in the supporting information section.

6.2. High quality symmetric contacts

The normal state resistance of all four contact pairs range between 150-200 $k\Omega$, and RA= 21-28 $k\Omega\mu m^2$, which is 2× lower than the device discussed in chapter 5. Figure 6.1(b) shows differential conductance G_{12} in respect to bias voltage V_{SD}, at a back gate voltage V_{BG}= 8 V. This measurement shows a suppression of conductance of a factor of ~ 40 at $|V_{SD}| < 2.4$ mV. The bias voltage at which the coherence peak occurs corresponds to $2\Delta_{MoRe}$. This finding suggests quasi-particle tunnelling across two similar N-S interfaces, illustrating a much better reproducibility of the individual VIA contact characteristics.

We plot the differential conductance G_{12} (in log scale for visibility of subgap structure) as a function of back gate voltage and bias voltage (see fig. 6.1(c)). The characteristic of the bulk superconducting gap is robust throughout different gate voltages. Moreover, there is no signature of Coulomb blockade effect in this measurement, and also in all other contact pairs (not shown), except for low gate voltages $V_{BG} < 2$ V, in contrast to the earlier data our ours [97].

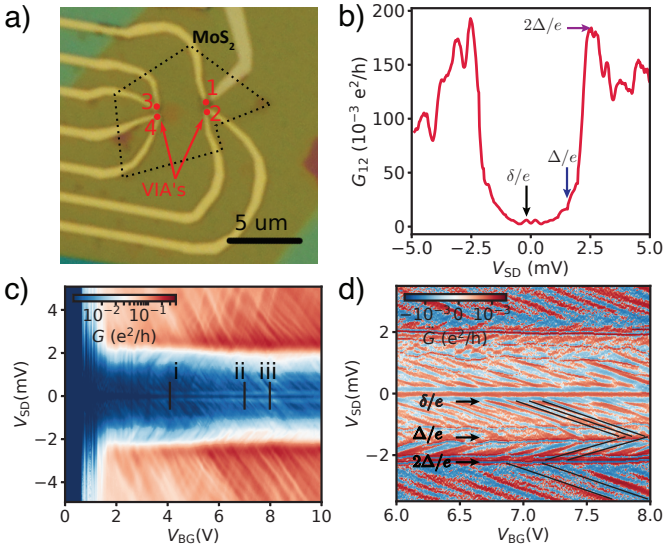

Figure 6.1. a) Optical microscope photograph of MoS_2 with MoRe based VIA contacts. b) Differential conductance C_1-C_2 as a function of bias voltage, at V_{BG}= 8 V. c) Differential conductance C_1-C_2 as a function of the bias voltage and gate voltage, and (d) is the second derivative of the data shown in (c) and zoomed in for more visibility.

6.3. Quantum interference effect

In fig. 6.1(c), we find regular patterns of narrow resonances with an enhanced conductance. For bias voltages much larger than $2\Delta/e$, these resonances can be understood as constructive interference of the electron wave function propagating in opposite directions in a cavity, analogous to the Fabry-Pérot resonance in an optical cavity. The slope of these resonances

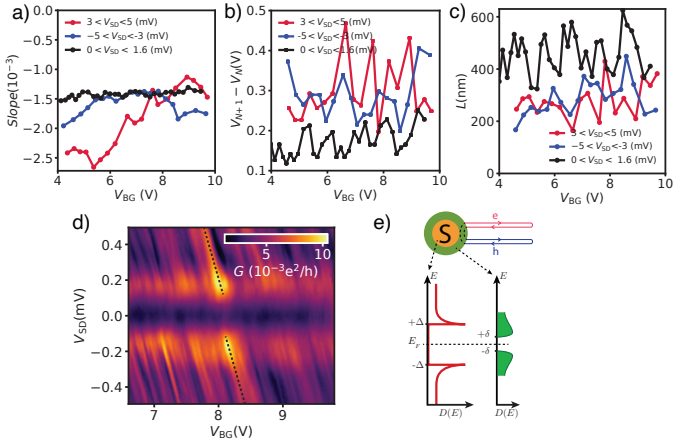

Figure 6.2. a) The evolution of the slope as a function of the gate voltage at three different bias voltages: red and blue at large bias voltage (above gap), and black (subgap) near zero bias voltage. b) Gate voltage difference of two consecutive resonance $V_{\mathrm{BG}}^{N+1} - V_{\mathrm{BG}}^{N}$, as a function of gate voltage, and at the same bias voltage range as (a). c) The characteristic length of Fabry Pérot cavity with respect to gate voltage, and at the same bias voltage range as (a). d) Differential conductance as a function of gate voltage, and a small bias voltage range. e) Schematic of superconducting contact, and minigap, together with the respective quasiparticle density of state. And schematics of a Fabry Pérot resonance at the N-S interface, including normal reflection in N, and Andreev reflection at the N-S interface.

$\Delta V_{\mathrm{SD}}/\Delta V_{\mathrm{BG}}$ as a function of V_{BG}, is plotted in fig. 6.2(a). We extracted the slope (manually) in three bias ranges, two for $\mid V_{\mathrm{SD}} \mid > 2\Delta_{\mathrm{MoRe}}/e$ (red and blue data points), and one for the resonances around zero bias voltage (black data points), well in the subgap regime $V_{\mathrm{SD}} < \Delta/e$. Seemingly, the FP resonances with positive and negative slopes have different amplitude that changes significantly at finite bias voltages, namely

$\Delta V_{\mathrm{SD}} = 2.4\mathrm{mV} = 2\Delta_{\mathrm{MoRe}}/e$, and $\Delta V_{\mathrm{SD}} = 1.6\mathrm{mV}$. This is visible in fig. 6.1(c), and in the second derivative of the conductance which is plotted in fig. 6.1(d). We can use these features to make statements about what features are truly "subgap".

Next, we extract the voltage difference of consecutive resonances ($V_{\mathrm{BG}}^{N+1} - V_{\mathrm{BG}}^{N}$), as a function of back gate voltage, for three different bias voltage regime (see fig. 6.2(b)). In spite of large variations, we find that the average spacing at low bias voltage (subgap) is roughly half of the spacing at large bias voltages.

6.4. Subgap structure and minigap

Figure 6.2(d) demonstrates the characteristics of the FP resonances at low bias voltage. At zero magnetic field, the conductance shows peaks around $|\ eV_{\rm SD}\ | \sim 170\,\mu$eV, well below the energy gap of bulk MoRe. Moreover, the average conductance is suppressed by a factor of ~ 1.5 at zero bias voltage. For the sake of discussion, we call this feature minigap, in order to distinguish it from the superconducting energy gap of the bulk MoRe. Our measurement exhibits minigap for all gate voltage ranges, and a similar characteristic in other contact pairs (not shown).

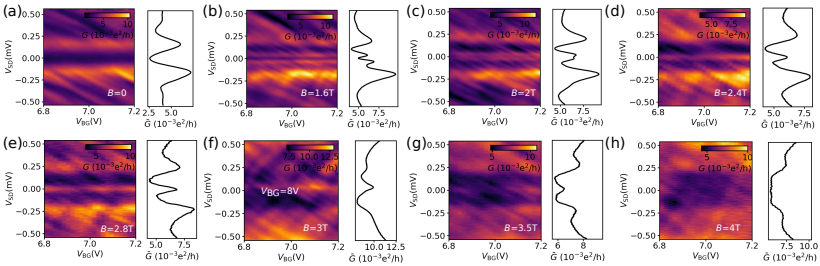

Figure 6.3. Left panels: differential conductance as a function bias voltage, at different ranges of gate voltage. Right panels: averaged differential conductance along the respective range of gate voltage $V_{\rm BG} = 6.8 - 7.2\,$V.

In fig. 6.3(left panels) we plot the conductance as a function of the gate and bias voltage, and the average of conductance (right panels) along the corresponding given gate voltage $V_{\rm BG} = 6.8 - 7.2\,$V. With increasing magnetic field (in perpendicular direction), the peaks of minigap split in energy, with two peaks merging at zero bias voltage around $B \sim 2\,$T to form a single maximum that sticks to $V_{\rm SD} \approx 0$ for an extended magnetic field range. At a higher magnetic field (i.e. $B > 3.5\,$T), this amplitude of the zero bias peak (ZBP) decreases below the noise level. Although the magnetic field range where ZBP prevails for all gate voltages $V_{\rm BG} > 4.5\,$V (see fig. 6.4(a,b) and fig. 6.6 in appendix).

In fig. 6.4(c) we plot differential conductance as a function of bias voltage and magnetic field, at $V_{\rm BG} = 7\,$V. A smooth background along bias voltage is subtracted to reduce the flux jump that manifests in the conductance measurement. The finite bias peak at zero magnetic field split, and form a ZBP at $B = 2 - 3.5\,$T. In these measurements, we can resolve a large number of resonances that are modulated in amplitude, constituting the observed broad peaks and features with a steep slope. This is more clear

in 6.4(d), that is measured at lower gate voltage V_{BG} =4.2 V, where ZBP is absent. We have observed similar characteristics, including ZBP at a finite magnetic field in the measurements of all other contact pairs.

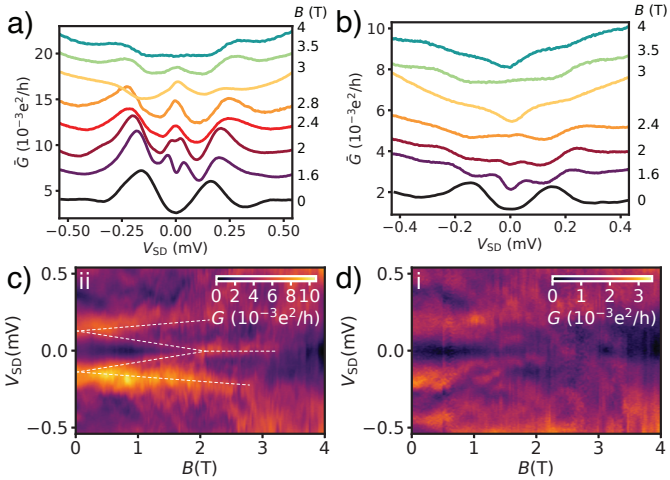

Figure 6.4. (a) and (b) show water fall plots of averaged differential conductance along gate voltage (a) V_{BG} = 6.8 − 7.2 V, and (b) V_{BG} = 3.8 − 4.2 V, as a function of bias voltage, at various indicated magnetic fields. (c) and (d) show the differential conductance with respect to the bias voltage and external magnetic field at (a) V_{BG}= 7 V, and (b) V_{BG}= 4.2 V.

Discussion

In this chapter, we investigate the measurements, and tentatively ascribe different characteristics. We use the model of an electron FP cavity with hard wall potential and therefore fixed cavity length, and use eq. 2.19 (and an hBN thickness of 30 nm, and $m^* = 0.6m_e$) to calculate the FP resonance slope $\sim 1.5 \times 10^{-3}$, which is roughly in agreement with the experimental finding shown in fig. 6.2(a). We would like to stress that, in our model, we assume the whole voltage drop occurs at the tunnel barrier, which in practice may not be the case due to the presence of resistance in series. To further investigate this issue, more advanced modelling will be necessary to self-consistantly calculate the voltage drops across the N-S interface. In addition, we also neglect gating effects on the MoS_2 band structure due to the bias voltage.

Moreover, in a single particle picture and using eq. 2.20, and gate voltage difference of consecutive resonances, we calculate and plot the FP cavity length in fig. 6.2(c). The resulting cavity length of ∼300 nm is slightly larger than the mean free path of MoS_2, but also on the scale of the inter-contact distance. However, the latter match is probably accidental, since we find similar cavity length between contact pairs with larger distance (see fig. 6.5(b)). To the best of our knowledge, and apart from weak (anti-)localization in MoS_2 [96], the coherent transport in MoS_2 has not been reported in the literature. As shown in fig. 6.2(c), the characteristic FP cavity length doubles for subgap resonances where $eV_{SD} < \Delta_{MoRe}$. This finding can be understood if we assume that the FP cavity is directly coupled to a superconducting reservoir and that the incoming electron is reflected as a hole in an AR process. The hole needs to traverse the cavity and undergo another AR into an electron before constructive interference can occur with the original electron wavefunction. This process can be seen as doubling of the effective cavity length, or better as the formation of (non-interacting) Andreev bound states due to constructive interference of the electron and hole wavefunctions in the same cavity [136].

As stated previously in chapter 2.3, we observe the physics of a one-dimensional FP resonance in a two-dimensional semiconducting system. Our initial guess based on semi-classical picture is that due to an "almost" 1:1 ratio of width:length, an impinging particle with an oblique angle will not be collected at the other contact. However, this picture is incorrect, since we observed FP resonances in an InSe device with superconducting Edge-contact (not shown), where the W:L ratio is 35. The calculated cavity length is roughly the same for the contact pair with an edge to edge distance of 300 nm, or 3 μm. We intuitively propose that the FP cavity might be formed near the contact area (see fig. 6.5(b)). The exact cause and location of FP is not clear, nevertheless, the FP cavity exists inside the

bulk of MoS_2 due to its gate and bias voltage dependence.

In addition, we tentatively attribute the suppression of conductance at small bias voltages $eV_{SD} < \delta$ (see fig. 6.3) to formation of minigap in the proximity of the superconducting contact [137, 138]. At small excitation energies $\varepsilon < \delta$ the DoS is suppressed, and DoS exhibits a peak at δ similar to the coherence peak in a BCS superconductor (see fig. 6.2(e)). In correspondence to our measurements, the minigap is pinned to the superconductor Fermi energy and there is no discernible gate voltage dependence. At larger excitation energies $\delta < \varepsilon < \Delta_{MoRe}$ there seems to be a continuum of the Andreev bound states at all energies. This finite sub-gap DoS, allows the formation of Andreev bound states mitigated by FP resonance.

Next, we will discuss the characteristics of minigap in presence of an external magnetic field. The eigenvalues of minigap can have a spin component (many subgap states with two spins), that can exhibit a Zeeman splitting at a finite magnetic field. This can explain the splitting of minigap in magnetic field that is shown in fig. 6.4(c), and fig. 6.6.

The overall field dependence of minigap characteristics is more or less independent of the gate voltage, reminiscent of the strongly debated Majorana bound states [21]. However, similar ZBP is theoretically predicted in the systems with topologically trivial phase [139, 140]. In ref. [141], authors show a ZBP due to the quantum interference in nanowires with intrinsic SOI and absence of time-reversal symmetry, that can survive a disorder potential at the proximity of N-S interface. Electrons and holes are scattered by random disorder in the normal conductor, is Andreev reflected at the N-S interface and forms closed trajectories. Because of the particle-hole symmetry, the phase shift due to travelling electrons and holes in these paths cancels out. Whether or not the time-reversal symmetry is broken, these scattering events permit weak (anti-)localization to sustain in the magnetic field. The sum of all trajectories leads to appearance of a minigap that evolves to a ZBP at finite magnetice field range. Therefore, we intuitively attribute the ZBP observed in our data to such effects.

6.5. Conclusions

In conclusion, we report quantum coherent transport in MoS_2 based semiconductor-superconductor hybrid electronic devices. We have further improved the quality of the VIA superconducting contacts to monolayer MoS_2, which allows us to investigate new phenomena in this hybrid system. We find a series of quantum interference effects, suggesting coherence length larger than mean free path $l_{mfp} < l_\phi \approx 300\,\text{nm}$. In addition, Andreev bound states resonances at energies below the superconducting gap is observed. The dimensionality of the system which is inherently 2D adds a new char-

acteristics to these Andreev bound states. Furthermore, we observed a minigap at around 170 μeV, well below the superconducting gap. In addition, we observed a zero bias peak anomaly at finite magnetic field between 2-3.5 T. The remaining question is if the intrinsic SOI in MoS_2 plays a role in the presence of a zero bias peak.

6.A. Supporting informations

In order to achieve a high success rate in fabrication of VIA contacts, we realized the bottom interface and the upper interface of the VIA contacts has to be clean and flat. Due to the nature of the sputtering process there is side deposition at the outline of the circular VIA contacts shown in fig. 6.5(a). We used a thicker PMMA resist layer (600 nm) and a larger undercut, to reduce the side deposition effect. Furthermore, we use post processing AFM cleaning to clean the remaining side deposition, indents, and polymer residues.

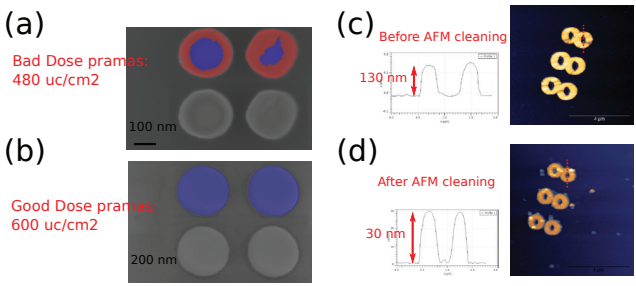

Figure 6.5. a), b) False colour scanning electron microscope micrograph of VIA contacts with sputtered MoRe: red shows the side deposition of MoRe, and blue is the flat surface of VIA contacts. The dose parameter used in (a) gives a smaller undercut, and the dose parameter used in (b) results in a larger undercut and consequently eliminates any side deposition. c) Atomic force microscopy micrograph of pristine MoRe VIA contact. The side deposition creates mounts as high as 130 nm. d) The same surface area that is shown in (c) after AFM cleaning. This side deposition is cleared effectively.

The measurements of the other contact pairs show similar characteristics of superconducting gap, and FP resonances that is tunable with gate voltage and bias voltage. We extracted similar sets of parameters including slope and FP cavity length of the other contact pairs and plotted in the fig. 6.6 and fig. 6.7.

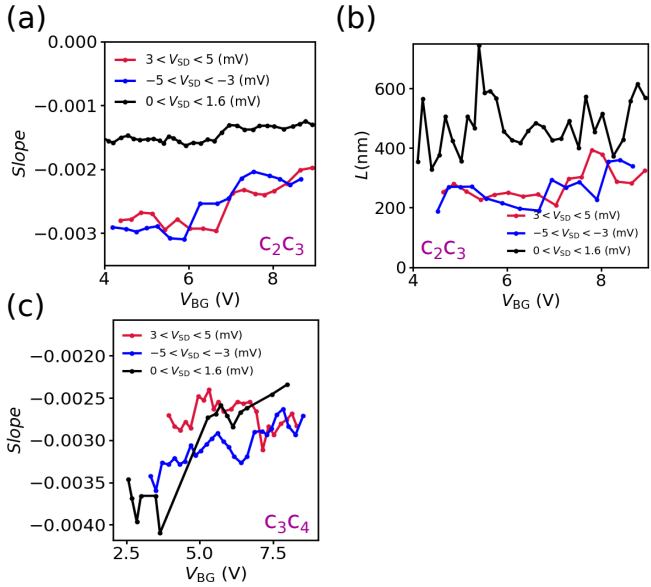

Figure 6.6. Calculated from the indicated contact pairs (a) and (b) that are associated to contacts C_2-C_3, and (c) to the contacts C_3-C_4. (a) and (c) The evolution of the slope in respect to the gate voltage at three different bias voltages: red and blue data points are acquired from large bias voltage, and black data points are acquired near zero bias voltage. b) The characteristic length of Fabry Pérot cavity in respect to gate voltage, for different bias voltage regimes. *Data points shown in (c) is so scarce and therefore the cavity length is erroneous.

The measurements of other contact pairs show the presence of minigap with a slightly different gap size, and the similar magnetic field range (2-3.5 T). We subtracted a smoth background from these measurements at each magnetic field.

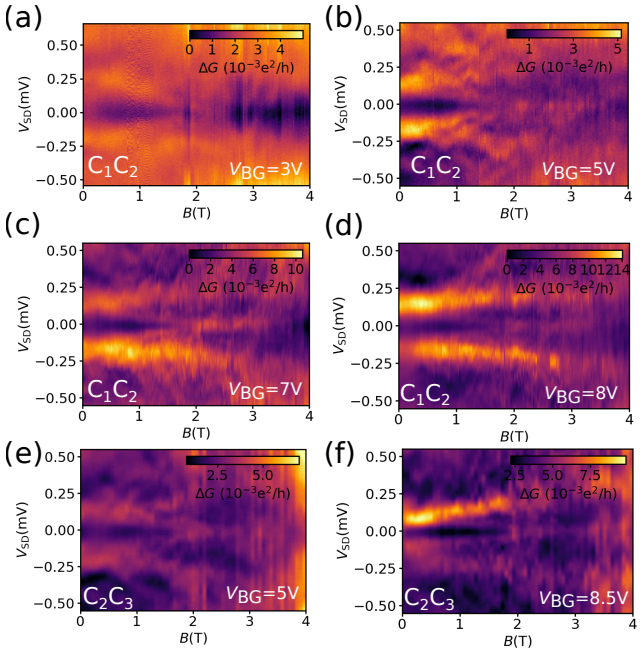

Figure 6.7. Differential conductance, as a function of bias voltage and magnetic field, at various indicated gate voltages. Measurements belong to the respective contact pairs (a-d) from C_1-C_2, and (e-f) from C_2-C_3.

7 Summary

The goal of this thesis was to investigate the possibility of inducing superconducting proximity effect in two-dimensional van der Waals heterostructures. We chose to work mainly with Molybdenum disulphide due to high literature value mobility and mean free path. We first established normal metal contacts to molybdenum disulphide, and investigated the intrinsic electrical and optical properties of it. We demonstrated low resistance contacts fabricated using various methods. Moreover, we investigated the mobility, and mean free path, as a tool to asses the quality of monolayer MoS_2. We found out that our best results shows properties that are in the same range of the cutting edge literatures.

Van der Waals contact based on graphene:$NbSe_2$ shows a record mobility in MoS_2, and very low resistance area product. Nevertheless, we have not observed any induced superconducting characteristics in the corresponding measurements.

The bottom contact fabrication techniques is a very promising technique in terms of facility, and high yield, yet suffers from surface oxidation. Therefore, bottom contacts of (air-sensitive) superconducting material (such as MoRe and Al) requires a novel method to minimize surface oxidation rate, and therefore is an outlook of this thesis.

Finally, we have developed superconducting MoRe vertical interconnect access (VIA) contacts, and demonstrated clear evidence of a superconducting energy gap and proximity effect for the first time. We investigated the characteristics of such a hybrid system at cryogenic temperatures and, measured magneto conductance in a large magnetic field range.

In addition, we have significantly improved the contact quality and yield of MoS_2 based electronic devices, which allowed us to investigate compelling physics such as quantum interference effects, superconducting minigap, zero bias peak anomaly, and Andreev bound state. Nevertheless, observation of Josephson effect had yet been unsuccessful.

Bibliography

[1] K. S. Novoselov, A. K. Geim, S. V. Morozov, D. Jiang, Y. Zhang, S. V. Dubonos, I. V. Grigorieva, and A. A. Firsov, Science **306**, 666 (2004).

[2] K. S. Novoselov, A. K. Geim, S. V. Morozov, D. Jiang, M. I. Katsnelson, I. V. Grigorieva, S. V. Dubonos, and A. A. Firsov, Nature **438**, 197 (2005).

[3] A. K. Geim and I. V. Grigorieva, Nature **499**, 419 (2013).

[4] S. Zihlmann, A. W. Cummings, J. H. Garcia, M. Kedves, K. Watanabe, T. Taniguchi, C. Schönenberger, and P. Makk, Physical Review B **97**, 75434 (2018).

[5] Y. Cao, V. Fatemi, S. Fang, K. Watanabe, T. Taniguchi, E. Kaxiras, and P. Jarillo-Herrero, Nature **556**, 43 (2018).

[6] C. Ataca, H. Şahin, and S. Ciraci, Journal of Physical Chemistry C **116**, 8983 (2012).

[7] B. Radisavljevic and A. Kis, Nature Materials **12**, 815 (2013).

[8] X. Xi, Z. Wang, W. Zhao, J. H. Park, K. T. Law, H. Berger, L. Forró, J. Shan, and K. F. Mak, Nature Physics **12**, 139 (2016).

[9] A. A. Soluyanov, D. Gresch, Z. Wang, Q. Wu, M. Troyer, X. Dai, and B. A. Bernevig, Nature **527**, 495 (2015).

[10] A. Kuc and T. Heine, "The electronic structure calculations of two-dimensional transition-metal dichalcogenides in the presence of external electric and magnetic fields," (2015).

[11] A. Kormányos, V. Zólyomi, N. D. Drummond, and G. Burkard, Physical Review X **4**, 1 (2014).

[12] K. F. Mak, C. Lee, J. Hone, J. Shan, and T. F. Heinz, Physical Review Letters **105** (2010), 10.1103/PhysRevLett.105.136805.

[13] J. Bardeen, Physical Review **97**, 1724 (1955).

[14] M. D. Simon and A. K. Geim, Journal of Applied Physics **87**, 6200 (2000).

[15] G. R. Stewart, Reviews of Modern Physics **56**, 755 (1984).

[16] A. Manchon, H. C. Koo, J. Nitta, S. M. Frolov, and R. A. Duine, Nature Materials **14**, 871 (2015).

[17] J. P. Heida, B. J. van Wees, T. M. Klapwijk, and G. Borghs, Physical Review B **60**, 13135 (1999).

[18] L. Hofstetter, S. Csonka, A. Baumgartner, G. Fülöp, S. D'Hollosy, J. Nygård, and C. Schönenberger, Physical Review Letters **107**, 136801 (2011).

[19] J. Gramich, A. Baumgartner, and C. Schönenberger, Physical Review Letters **115**, 216801 (2015).

[20] C. Jünger, S. Lehmann, K. A. Dick, C. Thelander, C. Schönenberger, and A. Baumgartner, (2021).

[21] V. Mourik, K. Zuo, S. M. Frolov, S. R. Plissard, E. P. Bakkers, and L. P. Kouwenhoven, Science **336**, 1003 (2012).

[22] J. I.-J. Wang, M. A. Yamoah, Q. Li, A. Karamlou, T. Dinh, B. Kannan, J. Braumueller, D. Kim, A. J. Melville, S. E. Muschinske, B. M. Niedzielski, K. Serniak, Y. Sung, R. Winik, J. L. Yoder, M. Schwartz, K. Watanabe, T. Taniguchi, T. P. Orlando, S. Gustavsson, P. Jarillo-Herrero, and W. D. Oliver, (2021).

[23] P. Krantz, M. Kjaergaard, F. Yan, T. P. Orlando, S. Gustavsson, and W. D. Oliver, Applied Physics Reviews **6** (2019), 10.1063/1.5089550.

[24] X. Liu, T. Galfsky, Z. Sun, F. Xia, E. C. Lin, Y. H. Lee, S. Kéna-Cohen, and V. M. Menon, Nature Photonics **9**, 30 (2014).

[25] X. Zheng, A. Calò, E. Albisetti, X. Liu, A. S. M. Alharbi, G. Arefe, X. Liu, M. Spieser, W. J. Yoo, T. Taniguchi, K. Watanabe, C. Aruta, A. Ciarrocchi, A. Kis, B. S. Lee, M. Lipson, J. Hone, D. Shahrjerdi, and E. Riedo, Nature Electronics **2**, 17 (2019).

[26] T. Ihn, *Semiconductor Nanostructures: Quantum States and Electronic Transport*, Vol. 9780199534 (Oxford University Press, 2009) pp. 1–568.

[27] I. Lifshitz and A. Kosevich, Sov. Phys. JETP **2**, 636 (1956).

[28] A. Isihara and L. Smrčka, Journal of Physics C: Solid State Physics **19**, 6777 (1986).

[29] R. T. Tung, Applied Physics Reviews **1** (2014), 10.1063/1.4858400.

[30] W. Liang, M. Bockrath, D. Bozovic, J. H. Hafner, M. Tinkham, and H. Park, Nature **411**, 665 (2001).

[31] C. Handschin, P. Makk, P. Rickhaus, M. H. Liu, K. Watanabe, T. Taniguchi, K. Richter, and C. Schönenberger, Nano Letters **17**, 328 (2017).

[32] M. I. Katsnelson, K. S. Novoselov, and A. K. Geim, Nature Physics **2**, 620 (2006).

[33] M. A. Topinka, B. J. LeRoy, R. M. Westervelt, S. E. Shaw, R. Fleischmann, E. J. Heller, K. D. Maranowski, and A. C. Gossard, Nature **410**, 183 (2001).

[34] L. P. Kouwenhoven, D. G. Austing, and S. Tarucha, (2001).

[35] H. K. Onnes, *HEIKE K AMERLINGH O NNES*, Tech. Rep. (1913).

[36] W. Meissner and R. Ochsenfeld, Die Naturwissenschaften **21**, 787 (1933).

[37] Z. Y. Wang, Physica C: Superconductivity and its Applications **299**, 256 (1998).

[38] J. R. Schrieffer, Theory of Superconductivity **105**, 1 (2018).

[39] G. E. Blonder, M. Tinkham, and T. M. Klapwijk, Physical Review B **25**, 4515 (1982).

[40] T. T. Heikkilä, *The Physics of Nanoelectronics* (Oxford University Press, 2013).

[41] J. Bardeen, L. N. Cooper, and J. R. Schrieffer, Physical Review **108**, 1175 (1957).

[42] C. W. Beenakker, Physical Review Letters **97**, 1 (2006).

[43] C. W. Beenakker, Reviews of Modern Physics **80**, 1337 (2008).

[44] D. K. Efetov and K. B. Efetov, Physical Review B **94**, 75403 (2016).

[45] R. C. Dynes, J. P. Garno, G. B. Hertel, and T. P. Orlando, Physical Review Letters **53**, 2437 (1984).

[46] A. Pleceník, M. Grajcar, A. Beňačka, P. Seidel, and A. Pfuch, Physical Review B **49**, 10016 (1994).

[47] R. C. Dynes, V. Narayanamurti, and J. P. Garno, Physical Review Letters **41**, 1509 (1978).

[48] B. D. Josephson, Physics Letters **1**, 251 (1962).

[49] C. Jünger, A. Baumgartner, R. Delagrange, D. Chevallier, S. Lehmann, M. Nilsson, K. A. Dick, C. Thelander, and C. Schönenberger, Communications Physics **2**, 1 (2019).

[50] B. J. Van Wees, P. De Vries, P. Magnée, and T. M. Klapwijk, Physical Review Letters **69**, 510 (1992).

[51] A. Kastalsky, A. W. Kleinsasser, L. H. Greene, R. Bhat, F. P. Milliken, and J. P. Harbison, Physical Review Letters **67**, 3026 (1991).

[52] H. Takayanagi and T. Kawakami, Physical Review Letters **54**, 2449 (1985).

[53] A. Splendiani, L. Sun, Y. Zhang, T. Li, J. Kim, C. Y. Chim, G. Galli, and F. Wang, Nano Letters **10**, 1271 (2010).

[54] D. Xiao, G. B. Liu, W. Feng, X. Xu, and W. Yao, Physical Review Letters **108**, 196802 (2012).

[55] L. F. Mattheiss, Physical Review B **8**, 3719 (1973).

[56] J. A. Wilson and A. D. Yoffe, Advances in Physics **18**, 193 (1969).

[57] W. S. Yun, S. W. Han, S. C. Hong, I. G. Kim, and J. D. Lee, Physical Review B - Condensed Matter and Materials Physics **85**, 033305 (2012).

[58] F. Rose, M. O. Goerbig, and F. Piéchon, Physical Review B - Condensed Matter and Materials Physics **88**, 125438 (2013).

[59] A. Kormányos, G. Burkard, M. Gmitra, J. Fabian, V. Zólyomi, N. D. Drummond, and V. Fal'ko, 2D Materials **2**, 022001 (2015).

[60] S. Larentis, H. C. Movva, B. Fallahazad, K. Kim, A. Behroozi, T. Taniguchi, K. Watanabe, S. K. Banerjee, and E. Tutuc, Physical Review B **97**, 201407 (2018).

[61] R. Pisoni, A. Kormányos, M. Brooks, Z. Lei, P. Back, M. Eich, H. Overweg, Y. Lee, P. Rickhaus, K. Watanabe, T. Taniguchi, A. Imamoglu, G. Burkard, T. Ihn, and K. Ensslin, Physical Review Letters **121**, 247701 (2018).

[62] S. K. Jeong, M. Inaba, Y. Iriyama, T. Abe, and Z. Ogumi, Electrochemical and Solid-State Letters **6**, A13 (2003).

[63] D. C. Marcano, D. V. Kosynkin, J. M. Berlin, A. Sinitskii, Z. Sun, A. Slesarev, L. B. Alemany, W. Lu, and J. M. Tour, ACS Nano **4**, 4806 (2010).

[64] L. A. Ponomarenko, R. V. Gorbachev, G. L. Yu, D. C. Elias, R. Jalil, A. A. Patel, A. Mishchenko, A. S. Mayorov, C. R. Woods, J. R. Wallbank, M. Mucha-Kruczynski, B. A. Piot, M. Potemski, I. V. Grigorieva, K. S. Novoselov, F. Guinea, V. I. Fal'ko, and A. K. Geim, Nature **497**, 594 (2013).

[65] J. Chen, B. D. Woods, P. Yu, M. Hocevar, D. Car, S. R. Plissard, E. P. Bakkers, T. D. Stanescu, and S. M. Frolov, *Physical Review Letters*, Tech. Rep. 10 (2019) arXiv:1902.02773 .

[66] B. Yang, M.-F. Tu, J. Kim, Y. Wu, H. Wang, J. Alicea, R. Wu, M. Bockrath, and J. Shi, 2D Materials Letter **3**, 31012 (2016).

[67] T. Völkl, T. Rockinger, M. Drienovsky, K. Watanabe, T. Taniguchi, D. Weiss, and J. Eroms, Physical Review B **96**, 1 (2017).

[68] T. Wakamura, F. Reale, P. Palczynski, S. Guéron, C. Mattevi, and H. Bouchiat, Physical Review Letters **120**, 1 (2018).

[69] J. C. Leutenantsmeyer, A. A. Kaverzin, M. Wojtaszek, and B. J. V. Wees, 2D Materials **4**, 1 (2017).

[70] Y. Y. Wang, R. X. Gao, Z. H. Ni, H. He, S. P. Guo, H. P. Yang, C. X. Cong, and T. Yu, Nanotechnology **23**, 1 (2012).

[71] R. V. Gorbachev, I. Riaz, R. R. Nair, R. Jalil, L. Britnell, B. D. Belle, E. W. Hill, K. S. Novoselov, K. Watanabe, T. Taniguchi, A. K. Geim, and P. Blake, Small **7**, 465 (2011).

[72] L. Wang, I. Meric, P. Y. Huang, Q. Gao, Y. Gao, H. Tran, T. Taniguchi, K. Watanabe, L. M. Campos, D. A. Muller, J. Guo, P. Kim, J. Hone, K. L. Shepard, and C. R. Dean, Science **342**, 614 (2013).

[73] E. Ponomarev, Á. Pásztor, A. Waelchli, A. Scarfato, N. Ubrig, C. Renner, and A. F. Morpurgo, ACS Nano **12**, 2669 (2018).

[74] G. B. Babkin, S. D. Grishin, V. A. Zhirnov, S. S. Kellin, and A. V. Potapov, Journal of Applied Mechanics and Technical Physics **15**, 745 (1974).

[75] E. J. Telford, A. Benyamini, D. Rhodes, D. Wang, Y. Jung, A. Zangiabadi, K. Watanabe, T. Taniguchi, S. Jia, K. Barmak, A. N. Pasupathy, C. R. Dean, and J. Hone, Nano Letters **18**, 1416 (2018).

[76] X. Cui, G. H. Lee, Y. D. Kim, G. Arefe, P. Y. Huang, C. H. Lee, D. A. Chenet, X. Zhang, L. Wang, F. Ye, F. Pizzocchero, B. S. Jessen, K. Watanabe, T. Taniguchi, D. A. Muller, T. Low, P. Kim, and J. Hone, Nature Nanotechnology **10**, 534 (2015).

[77] K. Marinov, A. Avsar, K. Watanabe, T. Taniguchi, and A. Kis, Nature Communications **8**, 1938 (2017).

[78] R. Pisoni, Y. Lee, H. Overweg, M. Eich, P. Simonet, K. Watanabe, T. Taniguchi, R. Gorbachev, T. Ihn, and K. Ensslin, Nano Letters **17**, 5008 (2017).

[79] J. Lee, M. Kim, K. Watanabe, T. Taniguchi, G.-H. Lee, and H.-J. Lee, Current Applied Physics **19**, 251 (2019).

[80] T. Dvir, A. Zalic, E. H. Fyhn, M. Amundsen, T. Taniguchi, K. Watanabe, J. Linder, and H. Steinberg, Physical Review B **103**, 115401 (2021).

[81] D. K. Efetov, L. Wang, C. Handschin, K. B. Efetov, J. Shuang, R. Cava, T. Taniguchi, K. Watanabe, J. Hone, C. R. Dean, and P. Kim, Nature Physics **12**, 328 (2016).

[82] R. Moriya, N. Yabuki, and T. Machida, Physical Review B **101**, 054503 (2020).

[83] A. Jain, Á. Szabó, M. Parzefall, E. Bonvin, T. Taniguchi, K. Watanabe, P. Bharadwaj, M. Luisier, and L. Novotny, Nano Letters **19**, 6914 (2019).

[84] B. Radisavljevic, A. Radenovic, J. Brivio, V. Giacometti, and A. Kis, Nature Nanotechnology **6**, 147 (2011).

[85] R. Fivaz and E. Mooser, Physical Review **163**, 743 (1967).

[86] A. Ayari, E. Cobas, O. Ogundadegbe, and M. S. Fuhrer, Journal of Applied Physics **101** (2007), 10.1063/1.2407388.

[87] B. W. Baugher, H. O. Churchill, Y. Yang, and P. Jarillo-Herrero, Nano Letters **13**, 4212 (2013).

[88] X. Cui, E.-M. Shih, L. A. Jauregui, S. H. Chae, Y. D. Kim, B. Li, D. Seo, K. Pistunova, J. Yin, J.-H. Park, H.-J. Choi, Y. H. Lee, K. Watanabe, T. Taniguchi, P. Kim, C. R. Dean, and J. C. Hone, Nano Letters **17**, 4781 (2017).

[89] H. Li, X. Zhu, Z. K. Tang, and X. H. Zhang, Journal of Luminescence **199**, 210 (2018).

[90] J. G. Roch, D. Miserev, G. Froehlicher, N. Leisgang, L. Sponfeldner, K. Watanabe, T. Taniguchi, J. Klinovaja, D. Loss, and R. J. Warburton, Physical Review Letters **124** (2020), 10.1103/PhysRevLett.124.187602.

[91] D. K. Efimkin and A. H. MacDonald, Physical Review B **95**, 35417 (2017).

[92] D. Van Tuan, B. Scharf, I. Zutić, and H. Dery, Physical Review X **7** (2017), 10.1103/PhysRevX.7.041040.

[93] H. F. Hess, R. B. Robinson, R. C. Dynes, J. M. Valles, and J. V. Waszczak, Physical Review Letters **62**, 214 (1989).

[94] S. Foner and E. J. McNiff, Physics Letters A **45**, 429 (1973).

[95] T. Dvir, F. Massee, L. Attias, M. Khodas, M. Aprili, C. H. Quay, and H. Steinberg, Nature Communications **9** (2018), 10.1038/s41467-018-03000-w.

[96] N. Papadopoulos, K. Watanabe, T. Taniguchi, H. S. Van Der Zant, and G. A. Steele, Physical Review B **99**, 115414 (2019).

[97] M. Ramezani, I. C. Sampaio, K. Watanabe, T. Taniguchi, C. Schönenberger, and A. Baumgartner, Nano Letters **21**, 5614 (2021).

[98] T. W. Larsen, K. D. Petersson, F. Kuemmeth, T. S. Jespersen, P. Krogstrup, J. Nygård, and C. M. Marcus, Phys. Rev. Lett. **115**, 127001 (2015).

[99] M. M. Leivo, J. P. Pekola, and D. V. Averin, Applied Physics Letters **68**, 1996 (1996).

[100] S. Roddaro, A. Pescaglini, D. Ercolani, L. Sorba, F. Giazotto, and F. Beltram, Nano Research **4**, 259 (2011).

[101] M. T. Deng, S. Vaitiekenas, E. B. Hansen, J. Danon, M. Leijnse, K. Flensberg, J. Nygård, P. Krogstrup, and C. M. Marcus, Science **354**, 1557 (2016).

[102] L. Hofstetter, S. Csonka, J. Nygård, and C. Schönenberger, Nature **461**, 960 (2009).

[103] G. Fülöp, S. D'Hollosy, A. Baumgartner, P. Makk, V. A. Guzenko, M. H. Madsen, J. Nygård, C. Schönenberger, and S. Csonka, Phys. Rev. B **90**, 235412 (2014).

[104] Z. Wan, A. Kazakov, M. J. Manfra, L. N. Pfeiffer, K. W. West, and L. P. Rokhinson, Nature Communications **6** (2015), 10.1038/ncomms8426.

[105] A. Fornieri, A. M. Whiticar, F. Setiawan, E. Portolés, A. C. Drachmann, A. Keselman, S. Gronin, C. Thomas, T. Wang, R. Kallaher, G. C. Gardner, E. Berg, M. J. Manfra, A. Stern, C. M. Marcus, and F. Nichele, Nature **569**, 89 (2019).

[106] F. Vischi, M. Carrega, A. Braggio, F. Paolucci, F. Bianco, S. Roddaro, and F. Giazotto, Phys. Rev. Appl. **13**, 54006 (2020).

[107] G. V. Graziano, J. S. Lee, M. Pendharkar, C. J. Palmstrøm, and V. S. Pribiag, Physical Review B **101**, 54510 (2020).

[108] S. Bhowal and S. Satpathy, Physical Review B **102**, 35409 (2020).

[109] I. Žutić, J. Fabian, and S. D. Sarma, Rev. Mod. Phys. **76**, 323 (2004).

[110] Q. H. Wang, K. Kalantar-Zadeh, A. Kis, J. N. Coleman, and M. S. Strano, Nat. Nanotechnol. **7**, 699 (2012).

[111] D. Y. Qiu, H. Felipe, and S. G. Louie, Phys. Rev. Lett. **111**, 216805 (2013).

[112] S. Tang, C. Zhang, D. Wong, Z. Pedramrazi, H. Z. Tsai, C. Jia, B. Moritz, M. Claassen, H. Ryu, S. Kahn, J. Jiang, H. Yan, M. Hashimoto, D. Lu, R. G. Moore, C. C. Hwang, C. Hwang, Z. Hussain, Y. Chen, M. M. Ugeda, Z. Liu, X. Xie, T. P. Devereaux, M. F. Crommie, S. K. Mo, and Z. X. Shen, Nature Physics **13**, 683 (2017).

[113] D. Miserev, J. Klinovaja, and D. Loss, Physical Review B **100**, 014428 (2019).

[114] R. Pisoni, Z. Lei, P. Back, M. Eich, H. Overweg, Y. Lee, K. Watanabe, T. Taniguchi, T. Ihn, and K. Ensslin, Applied Physics Letters **112**, 123101 (2018).

[115] G. M. Marega, Y. Zhao, A. Avsar, Z. Wang, M. Tripathi, A. Radenovic, and A. Kis, Nature **587**, 72 (2020).

[116] J. O. Island, G. A. Steele, H. S. J. van der Zant, and A. Castellanos-Gomez, 2D Materials **3**, 31002 (2016).

[117] D. J. Trainer, B. Wang, F. Bobba, N. Samuelson, X. Xi, J. Zasadzinski, J. Nieminen, A. Bansil, and M. Iavarone, ACS nano **14**, 2718 (2020).

[118] D. Costanzo, S. Jo, H. Berger, and A. F. Morpurgo, Nature Nanotechnology **11**, 339 (2016).

[119] J. G. Roch, G. Froehlicher, N. Leisgang, P. Makk, K. Watanabe, T. Taniguchi, and R. J. Warburton, Nature Nanotechnology **14**, 432 (2019).

[120] A. Allain, J. Kang, K. Banerjee, and A. Kis, Nature Materials **14**, 1195 (2015).

[121] K. Schauble, D. Zakhidov, E. Yalon, S. Deshmukh, R. W. Grady, K. A. Cooley, C. J. McClellan, S. Vaziri, D. Passarello, S. E. Mohney, M. F. Toney, A. K. Sood, A. Salleo, and E. Pop, ACS Nano **14**, 14798 (2020).

[122] J. Samm, J. Gramich, A. Baumgartner, M. Weiss, and C. Schönenberger, J. Appl. Phys. **115**, 174309 (2014).

[123] D. Lembke, S. Bertolazzi, and A. Kis, Accounts of Chemical Research **48**, 100 (2015).

[124] A. Seredinski, E. G. Arnault, V. Z. Costa, L. Zhao, T. F. Q. Larson, K. Watanabe, T. Taniguchi, F.Amet, A. K. M. Newaz, and and G. Finkelstein, arXiv: , 2101.06194 (2021).

[125] M. J. Witcomb and D. Dew-Hughes, Journal of The Less-Common Metals **31**, 197 (1973).

[126] S. Sundar, L. S. Sharath Chandra, V. K. Sharma, M. K. Chattopadhyay, and S. B. Roy, in *AIP Conference Proceedings*, Vol. 1512 (American Institute of Physics, 2013) pp. 1092–1093.

[127] V. Singh, B. H. Schneider, S. J. Bosman, E. P. J. Merkx, and G. A. Steele, Appl. Phys. Lett. **105**, 222601 (2014).

[128] J. D. Pillet, C. H. L. Quay, P. Morfin, C. Bena, A. L. Yeyati, P. Joyez, J.-D. Pillet1, C. H. L. Quay, P. Morfin, C. Bena, A. L. Yeyati, and P. Joyez, Nat. Physics **6**, 965 (2010).

[129] J. Gramich, A. Baumgartner, and C. Schönenberger, Physical Review B **96**, 195418 (2017).

[130] S. Heedt, M. Quintero-Pérez, F. Borsoi, A. Fursina, N. van Loo, G. P. Mazur, M. Nowak, M. Ammerlaan, K. Li, S. Korneychuk, and Others, arXiv preprint arXiv:2007.14383 (2020).

[131] R. C. Dynes and T. A. Fulton, Physical Review B **3**, 3015 (1971).

[132] S. Skalski, O. Betbeder-Matibet, and P. R. Weiss, Physical Review **136**, A1500 (1964).

[133] J. Gramich, A. Baumgartner, and C. Schönenberger, Applied Physics Letters **108**, 172604 (2016).

[134] Q.-f. Sun, J. Wang, and T.-h. Lin, Phys. Rev. B **59**, 3831 (1999).

[135] E. Zhitlukhina, I. Devyatov, O. Egorov, M. Belogolovskii, and P. Seidel, Nanoscale Research Letters **11**, 1 (2016).

[136] P. G. de Gennes and D. Saint-James, Physics Letters **4**, 151 (1963).

[137] C. Beenakker (2005) pp. 131–174, arXiv:0406018 [cond-mat] .

[138] L. Banszerus, F. Libisch, A. Ceruti, S. Blien, K. Watanabe, T. Taniguchi, A. K. Hüttel, B. Beschoten, F. Hassler, and C. Stampfer, (2020).

[139] H. Pan and S. Das Sarma, Physical Review Research **2**, 13377 (2020).

[140] H. Pan and S. Das Sarma, Physical Review B **104** (2021), 10.1103/PhysRevB.104.054510.

[141] D. I. Pikulin, J. P. Dahlhaus, M. Wimmer, H. Schomerus, and C. W. Beenakker, New Journal of Physics **14**, 125011 (2012).

A Fabrication Recipes

In the following we give the detailed fabrication recipes used to build the nano structures.

A.1. Van der Waals heterostructure fabrication

A.1.1. Material sources

1. Graphite: NGS Trading & Consulting GmbH, natural graphite source
2. MoS_2: SPI supplies, West Chester, USA
3. hBN: T. Taniguchi et al., National Institute for Material Science, 1-1 Namiki, Tsukuba 305-0044, Japan
4. Exfoliation tape: NITTO ELP-150P-LC

A.1.2. Annealing

1. Forming gas: H_2/N_2 (8%/92%)
2. Pressure 10-50 mbar
3. Ramping to 300 °C in 30 min
4. Hold temperature for 3-4 hours
5. Cool down to 30 °C in 30 min

A.2. Reactive ion etching

Depending on the design and the workflow a special mixture of the gas with a unique pare of parameters may be used.

A.2.1. CHF_3/O_2

1. CHF_3/O_2 (40 sccm/4 sccm); power 60 W; pressure 60 mTorr
2. Etching rates:
   - hBN: 0.3-0.33 nm/s
   - SiO_2: ∼0.23 nm/s
   - graphite: 0.07 nm/s

A.2.2. $SF_6/Ar/O_2$

1. $SF_6/Ar/O_2$ (20 sccm/5 sccm/4 sccm); power 50 W; pressure 25 mTorr
2. Etching rates:
   - hBN: >6.35 nm/s
   - SiO_2: ∼0.5 nm/s
3. Often after the SF_6 etching a O_2 plasma was used to remove cross-linked PMMA.

A.2.3. O_2

1. O_2 (20 sccm); power 60 W; pressure 40 mTorr
2. Etching rates:
   - hBN: ∼0.33 nm/s
   - PMMA: ∼1.66 nm/s

A.3. Electron beam lithography

A.3.1. PMMA mask for etching and contact deposition

1. PMMA 950k diluted in Anisole (solid content 4.5-5.5%)
2. Spin coat at 4000 rpm for 40 s with ramp rate of 1000 rpm/s ($\approx 450\,nm$)
3. Back out at 180 °C for 3 min
4. Exposure with e-beam (EHT=17 kV; dose≈410-600 $\mu C/cm^2$)
5. Development in cold (∼5 °C) IPA:H_2O (7:3) for 60 s
6. Blow dry with N_2

A.3.2. PMMA lift-off

1. Sample in Acetone (T=50 °C) for 30 min
2. Remove remaining metal by Acetone flow created with a syringe
3. Transfer sample into IPA
4. Wash off Acetone
5. Blow dry with N_2

A.4. Metal deposition

A.4.1. Sputtering of MoRe contacts

1. PMMA mask defined by EBL
2. O_2 etching (5 s)
3. Sputter MoRe using a AJA ATC Orion
4. Ignite plasma (Ar 30 sccm, pressure 20 mT, power 50 W)
5. Presputter for 2 min
6. Adjust parameters according to sputtering recipe
7. Single MoRe (1:1) target:
   - power 100 W
   - background pressure 2 mTorr
   - Ar flow 30 sccm
   - Sample rotation "off"
   - hight 40 cm
   - rate 0.24 nm/s
8. Lift-off in Acetone (A.3.2)

A.4.2. Fabrication of Au contacts

1. PMMA mask defined by EBL (A.3.1)
2. O_2 etching (5 s)
3. The metal was deposited using a Sharon e-beam evaporator
4. 5-10 nm of Ti was deposited as a sticking layer
5. Evaporate Au
6. Lift-off in Acetone (A.3.2)

A.4.3. Fabrication of metal top gates

1. PMMA mask defined by EBL (A.3.1)
2. O_2 etching (5 s) (A.2) to increase the adhesion
3. The metal was deposited using a Sharon e-beam evaporator
4. 10 nm of Ti was deposited as a sticking layer
5. Evaporate Au
6. Lift-off in Acetone (A.3.2)

A.5. PC mixture

1. clean glass vial with chloroform and magnetic stirring bar
2. add 0.7 g of Poly(Bisphenol A carbonate)
3. add 20 ml of chloroform
4. close the vial and seal it with parafilm
5. let it stir over night at 40° C to dissolve the PC

A.5.1. Assembly of vdW-heterostructures

In the following the detailed procedure of vdW-heterostructures fabrication is presented.

1. PC film preparation by drop casing a solution of PC in chloroform (9 wt%) on a glass slide. A second glass slide is then used to disperse the solution uniformly over both glass slides by pressing/sliding them against each other. Be fast as the chloroform evaporates rapidly.
2. Transfer of the dried PC layer to a PDMS stamp mounted on a glass slide with the help of window in a Scotch tape.
3. Exfoliate top mos layer on Si/SiO_2 substrate
4. Pick up top layer with PC at $\approx$80 °C
5. Pick up of next layer with PC/top layer, repeat for each layer to be picked up.
6. Release "half-stack" on bottom layer on Si/SiO_2 substrate by heating to 150 °C to release the PC layer from the PDMS.
7. Remove PC from the complete stack with chloroform ($\sim$1 h)
8. Thermal annealing in N_2/H_2 atmosphere (temperature depends on the involved materials)

A.6. E-beam lithography and development

A.6.1. PMMA resist for contacts and etching (negative mask)

1. Spin-coat PMMA (thickness may vary, bake at 180 °C for 3 min)
2. Expose with E-beam (V20 keV; Dose=450 µC/cm^2)
3. Cold-development in IPA:H_2O (ratio 7:3) at $\sim$5 °C for 60 s, blow-dry

Curriculum Vitae

Education

Mar. 2018–Feb. 2022 **PhD in experimental physics at the University of Basel**

- Dissertation in the group of Prof. Dr. C. Schönenberger
  "Superconducting contacts and quantum interference phenomena in monolayer semiconductor devices"

Feb. 2016–Dec. 2017 **Masters of science in materials science and Nanotechnology at the Bilkent University, Ankara, Turkey**

- Dissertation in the group of Dr. T. S. Kasirga
  "Synthesis and characterization of novel atomically thin 2D-material"

Oct. 2010–Jun. 2015 **Bachelor of Science in materials science and engineering at Amirkabir university of technology, Tehran, Iran**

- Dissertation in the group of Prof. Dr. F. Mahboubi
  "Synthesis of ternary MnO_2/graphene nanosheets/carbon nanotube composites for supercapacitor applications"

Extracurricular activity

Jul. 2019–Present **Community manager and event organizer**

- Green-UP environment platform, Basel. *"Our core activity is around sustainability, frugality, and circular economy."*

2018–Present **Computer Programming and Robotics**

- Digitalizing vintage camera modules.

- Embedding forward and reverse kinematics.

List of publications

- *"Coherent transport and two dimensional Andreev bound states in a monolayer semiconductor"*
  M. Ramezani, I. C. Sampaio, K. Watanabe, T. Taniguchi, C. Schönenberger, and A. Baumgartner
  In preparation

- *"Superconducting contacts to a monolayer semiconductor"*
  M. Ramezani, I. C. Sampaio, K. Watanabe, T. Taniguchi, C. Schönenberger, and A. Baumgartner
  Nano Letters **21**, 5614-5619 (2021)

- *"Facile synthesis of ternary MnO2/graphene nanosheets/carbon nanotubes composites with high rate capability for supercapacitor applications"*
  M. Ramezani, M. Fathi, F. Mahboubi
  Electrochimica Acta **174**, 345-355 (2015)

- *"Effects of Thickness on the Metal-Insulator Transition in Free-Standing Vanadium Dioxide Nanocrystals"*
  MM Fadlelmula, EC Surmeli, **M. Ramezani**, TS Kasirga
  Nano Letters **17,3**, 1762-1767 (2017)

Acknowledgements

The years I have spent in graduate school are one of the most confounding and unforeseen part of my life. I would have not imagined that this thesis will be the third thesis I have to write, and I lead a PhD project in condensed matter physics in the middle of a pandemic. Nevertheless, here I am writing the acknowledgements to everyone who helped me in one way or another in this long journey.

First and foremost, I would like to express my gratitude towards my supervisor Prof. Dr. Christian Schönenberger for providing me with the opportunity to pursue my scientific research in the nanoelectronics group. In November 2017, I was invited by Christian for a week-long interview and hands-on laboratory work that was mentored by Dr. Clevin Handschin. We fabricated a graphene Josephson junction, which I finally measured when I started my PhD in 2018. I am forever honoured to be able to work in Christian's group as he is a brilliant scientist, a role model in research, down to earth, supportive, and a determined person. Likewise, I am also grateful to my second first-supervisor Dr. Andreas Baumgartner. Aside from our endless meetings discussing physics, we shared so many discussions about history, mythology, and politics. I also want to extend my sincere thanks to my second supervisor Prof. Dr. Richard Warburton, with whom I had quite a few meetings, sometimes even spontaneous meetings at the Mensa of Physics department. He always encouraged me to address the biggest questions and spread his positive attitude towards research. I also want to thank my doctoral committee members Prof. Dr. Klaus Ennslin and Assoc. Prof. Dr. Andras Kis for their critical review of my thesis.

Next, I would like to acknowledge Ian Sampaio my one-and-only and also the best lab buddy. Since he had joined us on this project, we had a synergistic effect and did most of the things together. The main progress that is made in this project was achieved due to our excellent teamwork. Also, he always stayed critical of the work and kept me thinking about the physics behind the measurements.

Besides, I would like to thank Michele Masseroni from the nanophysics group at the ETHZ for having numerous discussions and sharing thoughts and ideas, and sharing tacit knowledge involved in fabrication and studying 2D-semiconductors. I appreciate our constructive discussions in particular,

since the community is very small, and sometimes very competitive.

Likewise, I would like to thank Alexina Ollier, Marcin Kisiel, and Prof. Dr. Ernst Meyer from Nanolino group at the University of Basel. We investigated the ferromagnetic effects in 2D-semiconductor using magnetic pendulum AFM. This study would not be possible without their expertise and knowledge.

Besides, I have met brilliant people during the last few years living in Basel, those who have my respect for what they are. I appreciate the time we have spent with each other. My friends Masha, Martin, Gian, Zeynep and Faruq, my colleagues from the Green-UP community Nicole, Julia, Manuela, Veronika, and Marcel. Likewise, my friends and colleagues from the department of physics and nanoelectronics group Roy, Carlo, Alessia, Jann, Olivier, Natasha, Viktoria, Kristopher, Jost, David, Clevin, Simon, Matthijs, Gergö, Paritosh, Artem, and Martin, the researchers from SNI PhD school Tamara, Thomas, Joanan, and Eirini, all those who came along and joined our movie club by bringing their favourite motion pictures from their homeland. Also, other friends and colleagues whose are not named, however, without their support, I would not be here. I hope I can make up for all the time I was not with them.

I moved from Iran to Turkey, and then Switzerland about 7 years ago. I took my backpack with me and left my lovely family back home. They have always spoiled me with their love and care, though I have struggled to meet them in person ever since. I am indebted to my family for their unconditional support and encouragement.

Lastly, my greatest thank goes to Dr. Ana Jesus, she is my new family and my soul mate. We laughed, we cried, and we finished our PhD project fighting for it, but never forgot to be there for each other. She taught me so many things, among them is the difference between palaeontology and archaeology, and the fact that she does not study dinosaurs (pun intended).

Thank you all very much for your understanding and for sharing your precious moments with me and making all those memories. Without you all, the PhD life would not be this exciting. I am looking forward to keeping in touch with you in my post-PhD era. I close this manuscript, signing off as Dr. Ramezani.